The role of melting on the geochemical evolution and isotopic variability of an anatectic complex in the Iberian Variscides

Joana Ferreira, João Mata, Telmo Bento dos Santos, Inês Pereira

The role of melting on the geochemical evolution and isotopic variability of an anatectic complex in the Iberian Variscides

Joana A. Ferreira[1,2*], João Mata[1,2], Telmo Bento dos Santos[1,2], Inês Pereira[3,4]

[1] Instituto Dom Luiz (IDL), Faculdade de Ciências, Universidade de Lisboa, Campo Grande, 1749-016, Lisboa, Portugal

[2] Departamento de Geologia, Faculdade de Ciências, Universidade de Lisboa, C6, Campo Grande, 1749-016 Lisboa, Portugal

[3] School of Earth and Environmental Sciences, University of Portsmouth, Building Burnaby Rd Portsmouth P01 3QL, UK

[4] Laboratoire Magmas et Volcans, Université Clermont Auvergne, 6 avenue Blaise Pascal, TSA 60026 – CS 60026, 63178 Aubiere Cedex, France

*Corresponding author (jaferreira@fc.ul.pt)

Abstract: Formation and evolution of migmatite-granite terranes usually involve several complex petrological and geochemical processes that leave their imprint on elemental and isotopic signatures. In this paper, we assess the role of melting reactions on the genesis of the Variscan Figueira de Castelo Rodrigo-Lumbrales Anatectic Complex (FCR-LAC) at the Central Iberian Zone, culminating in the generation of abundant S-type granites. At odds with the proposed for several anatectic complexes elsewhere, it is demonstrated that no isotopic (Sr-Nd-Hf-Pb) disequilibrium occurred in the FCR-LAC, in the transitions from metatexites to diatexites and, finally, to granites. However,

variable contribution of the source minerals generated batches of melts characterized by distinct parent/daughter ratios, which explain the significant heterogeneity of present-day isotopic signatures. While Rb/Sr ratios and the Pb budget of the successively generated lithotypes were mainly controlled by major minerals, such as muscovite, K-feldspar and plagioclase, the accessory phases played a major control on Sm/Nd and Lu/Hf ratios. Our study demonstrates the existence of two distinct diatexite groups produced by different reactions. Type-1 diatexites, having high Rb contents and fractionated HREE, are geochemically more akin to the associated S-type granites. They were produced via fluid-absent reactions during dehydration-melting of muscovite with production of peritectic K-feldspar, sillimanite and melt. The less abundant type-2 diatexites required influx of external fluids during melting reactions, which consumed more plagioclase than muscovite.

Isotopic data reveal the existence of two groups with distinct initial compositions (εNd_{320} = -5.05 to -6.03 and εHf_{320} = -3.42 to -4.45 *vs.* εNd_{320} = -7.30 to -8.89 and εHf_{320} = -6.45 to -8.47), both composed of metatexites, diatexites and granites, which is explained by source heterogeneity. The main source of the anatectic complex was the metasedimentary Neoproterozoic – Lower Cambrian Douro-Beiras Supergroup, with minor contribution of the Ordovician Ollo de Sapo magmatic rocks.

Keywords: Anatectic complex; Melting reactions; Isotope geochemistry; Variscan Orogeny

1. Introduction

Late-stage mountain building is typically characterized by crustal anatexis and generation of granitic bodies, a common feature in the continental tectonic framework

since the Archean (Whitney et al., 2004). Upper crust emplacement of granitic magmas leaving refractory residues leads to intracrustal differentiation, which explains the compositional distinction between lower and upper crust (Sawyer et al., 2011).

The production of large volumes of melt through partial melting of a source rock depends on protolith fertility, on the presence of fluids, and ~~of~~ on the temperature-pressure conditions, namely the magnitude of the thermal anomaly (Brown, 2013; Clemens, 2006). Metapelitic and metapsammitic rocks containing large amounts of hydrous phases, such as muscovite and biotite (30% to 50%), are fertile protoliths and potential sources of peraluminous melts through metamorphic incongruent melting reactions (fluid-present or fluid-absent) at 700 – 800 ºC (Brown, 2013; Sawyer et al., 2011). Indeed, fluid-absent melting of micas in metapelites and metagreywackes can yield up to 50 vol% of melt (Clemens and Vielzeuf, 1987; Sawyer et al., 2011; Bento dos Santos et al., 2011b; Brown, 2013). For these reasons, migmatite-granite complexes have been the target of several studies with the objective of exploring links between high-grade metamorphism, partial melting processes, the origin of the related granitic bodies and crustal differentiation (e.g. Johannes et al., 2003; Bento dos Santos et al., 2011a; Brown et al., 2016; Sola et al., 2013).

In the Iberian Variscan Belt (the southwestern sector of the European Variscan orogen), more precisely in the Central Iberian Zone (CIZ), several authors have emphasized the relationship between some granites and migmatitic rocks (Areias et al., 2014; Carrington da Costa and Teixeira, 1957; Ferreira et al., 2014; Pereira et al., 2017; Ribeiro et al., 2011; Vanderhaeghe, 2009). The Figueira de Castelo Rodrigo-Lumbrales Anatectic Complex (FCR-LAC) is one of such anatectic complexes and has the particularity of showing a clear spatial relationship between metatexites, diatexites and granites. In this way, this complex offers the opportunity to assess the melting reactions that genetically link migmatites (metatexites and diatexites), granites, and their metasedimentary sources. Links between the FCR-LAC granites and the hosting pre-Ordovician metasedimentary rocks have already been suggested by Ferreira et al.

(2019), based on the study of inherited zircon grains, a question that will be readdressed in this paper.

Radiogenic isotopes are widely applied to identify source characteristics of magmatic rocks (e.g. White, 2010). Indeed, it is usually assumed that the isotopic composition of a magma is similar to that of the source rock, a hypothesis implying that no isotopic fractionation occurs during melting and that almost the same happens with the parent (P)/daughter (D) element pairs. This is true if each of the source mineral phases is not a significant repository of any of the P or D elements for the isotopic systems considered, i.e. when the P and D elements are highly incompatible. However, in silica-rich magmatic systems, such as S-type granites and related anatectic rocks, isotopic disequilibrium becomes more common (e.g. Himalayan leucogranites - Ayres and Harris, 1997; Anatectic Complex of Toledo - Barbero et al., 1995; Sierra Nevada Batholith - Tommasini and Davies, 1997; Southern Sierra Nevada - Zeng et al., 2005b; see also Wolf et al., 2019;). Indeed, residue/melt isotopic disequilibrium can take place due to a) insufficient temperature to reach the closure temperature of some of the accessory phases, with which P and/or D elements are compatible, resulting in a significant fractionation (up to > 20 εHf units; Tang et al., 2014); and b) chemical diffusivity being sluggish compared with the time frame necessary for melt extraction from the residue (Ayres and Harris, 1997; Farina and Stevens, 2011; Zeng et al., 2005; Tang et al., 2014; Wolf et al., 2019). These factors can lead to the perception that isotopic disequilibrium during anatexis is ubiquitous (e.g. Tommasini and Davies, 1997). However, in some cases, even for situations specifically investigated for isotopic disequilibrium, no significant evidence–was found (e.g. Wolf et al., 2019). In this perspective, the isotopic variability of an anatectic complex must also be addressed in light of regional source heterogeneities (e.g. Yakymchuk et al., 2015, 2013), and on the role of melting reactions leading to distinct P/D pairs with the consequent development of distinct isotopic signatures due to variable rates of radiogenic ingrowth through time.

For these reasons, the importance of isotopic disequilibrium during anatexis is still inconclusive.

Distinct isotopic systems are expected to behave differently during anatexis, with some of them responding variably to diverse melting conditions (e.g. Wolf et al., 2019). This confers to multi-isotopic studies the potential to investigate the hypothetical role of isotopic disequilibrium and source heterogeneity, as well as to better decipher the role of distinct melting reactions during the different stages of anatexis.

Therefore, in this study, we use Sr, Nd, Hf and Pb isotopes, the elemental whole-rock compositions, and zircon and apatite trace-element compositions from the FCR-LAC lithologies to: 1) assess the melting reactions behind the different lithotypes; 2) evaluate the potential role of isotopic disequilibrium during anatexis; 3) provide insights onto the causes of isotopic variability characterizing the anatectic complex; and 4) explore the geochemical link between the different stages of anatexis, from migmatites to granites, and also to infer potential metapelitic protoliths.

2. Geological Setting

The European Variscan Belt is the result of a complex evolution culminating with the polyphasic collision of the continents Laurentia and Gondwana during the Devonian – Carboniferous periods (e.g. Dias and Ribeiro, 1995; Nance et al., 2010). In the internal zones of the orogen, the continental collision produced the rapid formation of metamorphic core complexes, characterised by the exhumation of migmatites, large volumes of granitic magmas, and LP-HT metamorphism (Burg et al., 1994; Schulmann et al., 2002).

The FCR-LAC is located within the autochthonous terranes of the variscan Central Iberian Zone (CIZ) and it is an example of a migmatite-granite complex formed during the Variscan Orogeny (e.g. Ferreira et al., 2019) (Fig. 1). This anatectic complex preserves significant field macroscopic evidence of the gradual anatectic evolution from

metatexites, to diatexites and to syn-tectonic granites (Fig. 2). The FCR-LAC contacts with low-grade (biotite and chlorite zone) metamorphic units of Ediacaran-Cambrian (to the North and South) and Ordovician age (to the South) through the Huebra and the Juzbado-Penalva do Castelo shear zones, respectively. Their sinistral kinematics were active at least during the intracontinental collision stage (D_3, third phase of the Iberian variscan deformation; Pereira et al., 2017 and references therein), although it has been suggested that it represents a much older tectonic discontinuity (Iglesias and Ribeiro, 1981). The Juzbado-Penalva do Castelo shear zone (JPCSZ) is a 200 km long, 5 to 15 km wide first-order structure, with a proposed horizontal displacement between 65 and 100 km (Iglesias and Ribeiro, 1981; Villar Alonso et al., 2000). Geothermobarometric estimates using mineral equilibria point to peak metamorphic conditions of T = 761 ± 50 ºC and P = 5.0 ± 1.0 kbar (Pereira et al., 2017). Exhumation mechanisms of this anatectic complex have been widely discussed and two major models have been proposed. Díez Fernández and Pereira (2016) invoked extensional tectonics and orogenic collapse as the mechanism responsible for anatexis and upper crust emplacement, followed by capture by the strike-slip shear zone. However, the interpretation of the complete exhumation process of this granitic-migmatitic association must consider that this complex occurs in contact with low grade metamorphic rocks to which is juxtaposed by first-order high-angle shear zones, also evidenced by recent magnetotelluric studies (Alves Ribeiro et al., 2017). Migmatites and the associated granites preserve a low dipping, non-horizontal transport lineation (6°–12°; Pereira et al., 2017), clearly indicative of a significant net vertical mass transfer during the 65 – 100 km horizontal displacement of the JPCSZ, caused by simple shear-dominated transpression during the D_3 stage (see Pereira et al., 2017). Petrochronological constrains recently published estimated cooling rates as high as 35 $ºC.Ma^{-1}$ and fast exhumation rates (max of 0.84 $mm.a^{-1}$), which confirm a tectonically-assisted exhumation process (Ferreira et al., 2019).

3. Field and petrographic observations

The low-grade (chlorite-biotite zones) metamorphic units are composed of phyllites and quartzphyllites, affected by a nearly E-W schistosity (Fig. 3a). Phyllites in the vicinity of granites show post-deformation andalusite porphyroblast growth, usually pseudomorphosed, formed by contact metamorphism (Fig. 2a and Fig. 3b). The mineral assemblage of these phyllites also includes quartz, muscovite, biotite, and minor plagioclase and chlorite, as well as accessory titanite, zircon, apatite, rare staurolite, and opaque minerals.

Metatexites exhibit stromatic structures still preserving a pre-melting banded orientation inherited from the regional E-W schistosity (i.e. inherited fabric). Sometimes, centimetric or millimetric lenses of peritectic sillimanite associated to muscovite are found (Fig. 2b). Occasionally, metatexites are intersected by centimetric leucosome, sometimes boudinated, and filled with granitic to pegmatitic material (Fig. 2c). Leucosome patches up to 20-35 cm, also occur in association with these veins (Fig. 2d). The large majority of leucosomes are concordant to the pre-migmatization structures (schistosity) of the hosting rocks. The melanosome of the foliated metatexite is predominantly composed of biotite and muscovite. In contrast, leucosomes are predominantly composed of a quartz-feldspar assemblage (Fig. 3c). Fibrolite appears as relic grains in late muscovite formed during retrogression (Fig. 3d). The most common accessory phases are zircon, apatite, tourmaline, staurolite and ilmenite.

Diatexites show structures such as restitic nodules (Fig. 2e), schlieren (Fig. 2f), and, occasionally, ptygmatic folding. Closer to the shear zones, diatexites reveal E-W oriented shear deformation planes, i.e. the same orientation as the shear zone. Locally, there are pegmatitic and leucosome veins forming vein-structured diatexites. Some of these diatexites show a near-nebulitic texture (only slightly more coarser-grained and biotite-enriched than the examples described in Sawyer (2008).. As a whole, diatexites comprise quartz, plagioclase, K-feldspar, biotite, minor fibrolitic sillimanite and

189 secondary muscovite (Fig. 3f). Chemically, two different groups of diatexites can be
190 distinguished (see section 6.2), which are not macroscopically distinguishable.
191 However, thin section petrography reveals that the mineralogical composition is slightly
192 different, with type-1 diatexites having more fibrolitic sillimanite and secondary
193 muscovite, but lower amounts of K-feldspar than type-2 diatexites (Table 1).

194 Additional evidence of partial melting in these migmatites can be found in the
195 occurrence of corroded grains of biotite and melt films (Fig. 3e), mainly in quartz-
196 feldspar boundaries.

197 In general, the contact between the metatexites, diatexites and granites is marked
198 by a gradual transition, but there are also injections of granitic material found in the
199 migmatites, feeding the S-type plutons.

200 Granites are essentially two mica-bearing, with biotite and muscovite appearing in
201 different proportions and with variable grain sizes. These variations led to their
202 grouping onto 10 different granite facies (Silva and Ribeiro, 2000; Fig. 2g and Fig. 2h).
203 Some granitic outcrops reveal deformation structures like those found in the
204 migmatites, compatible with the JPCSZ movement (Fig. 3h). These granites are mainly
205 composed of quartz, plagioclase, K-feldspar, biotite, muscovite (Fig. 3g) and minor
206 fibrolitic sillimanite. Accessory mineral assemblage includes zircon, apatite, rutile
207 needles and ilmenite.

208 Apatite from these granites yield 288 – 307 Ma, while newly grown zircon grains
209 provide magmatic U-Pb crystallisation ages between 300 and 317 Ma (Ferreira et al.,
210 2019). However, a significant part of the zircon population is inherited (54%), yielding
211 ages in the range 400 – 650 Ma, having survived the melting and segregation stages.

212

213 4. Analytical methods

214 We report 55 analyses of whole-rock geochemistry of granites, migmatites and
215 phyllites from the Douro-Beiras Supergroup that were conducted in the Activation Lab

in Ontario, Canada. Major elements were measured by Fusion Inductively Coupled Plasma Optical Emission Spectrometry and trace elements by Fusion Inductively Coupled Plasma Mass Spectrometry (see details in the Supplementary Material 1).

Whole-rock isotopic analyses of Sr, Nd, Hf and Pb were performed in 13 samples, including 8 migmatites (5 metatexites, 2 type-1 diatexites and 1 type-2 diatexite), 5 granites and 2 metasedimentary units from the Douro-Beiras Supergroup at the Laboratoire G-Time of the Université Libre de Bruxelles (ULB, Belgium) using a Nu Plasma I Multi-Collector Inductively Coupled Mass Spectrometer (MC-ICP-MS) instrument (for more details see the Supplementary Material 1).

Zircon and apatite grains separated from the anatectic units were analysed for their trace element content using an ASI RESOlution 193 nm ArF excimer laser coupled to the ANALYTIK JENA Plasma Quant Elite quadrupole ICP-MS at the University of Portsmouth (UoP) (see more analytical details in the Supplementary Material 1).

5. Results

5.1. Whole-rock elemental geochemistry

Whole-rock elemental compositions are presented in Table 2, where the studied samples are grouped as phyllites, metatexites, diatexites and granites.

Phyllites and metatexites are enriched in Al_2O_3, FeO^t, MgO and TiO_2 in comparison to diatexites and granites, evidencing a negative correlation with silica (Fig. 4). This reflects the larger abundance of refractory minerals (e.g. biotite and titanite) in the metasedimentary protoliths and in the metatexite's melanosomes, representative of an incipient degree of partial melting. On the other hand, diatexites and granites commonly yield higher contents of SiO_2, Na_2O, K_2O and P_2O_5 when compared to metatexites. This difference is consistent with higher degree of partial melting and, eventually the occurrence of some crystal fractionation (e.g. Sawyer, 2008), and, thus, with the production of quartz-plagioclase-, K-feldspar- and apatite-rich melts. Two types

of diatexites were identified mainly based on their composition (Fig. 4): type-1 diatexites (SiO_2 = 68 – 74 wt%) and type-2 diatexites (SiO_2 = 74 – 75 wt%). Additionally, type-2 diatexites are distinguishable by a wider variation of Na_2O concentration, slightly lower average $Fe_2O_3^t$ content and lower concentrations of P_2O_5, which are similar to the depicted by metatexites and phyllites.

All lithotypes display high Al_2O_3 content (Al_2O_3 > 12 wt.%), being strongly peraluminous (phyllites: ASI = 2.0 – 3.3, quartzphyllites: ASI = 1.2 – 2.4, metatexites: ASI = 1.5 – 2.7, diatexites: ASI = 1.1 – 1.5, and granites: ASI = 1.1 – 1.4).

The resemblance between metatexites and phyllites, revealed by major elements, is also generally depicted by trace elements (Fig. 5). Type-2 diatexites exhibit lower Rb contents compared to the other anatectic rocks, but similar to metasediments. Phyllites, quartzphyllites, and metatexites have significantly similar patterns in the multi-element diagrams, showing negative anomalies of Nb, K, Pb, Sr and Ti, and positive anomalies of U, Ta, La, Ce and Nd (Fig. 6a). Zr and Hf positive anomalies are evident in the quartzphyllites (Fig. 6a), as the result of their higher zircon contents (observed under the microscope), in agreement with their more psammitic characteristics in comparison with the remaining metasediments. Multi-element patterns of diatexites and granites overlap within error (Fig. 6b), exhibiting a wide range of values for some elements, such as Th, REE and Zr-Hf. Both lithotypes show negative anomalies for Nb, Pb, Sr and Ti. There are some similarities between metasediments/metatexites and diatexites/granites, as all yield Nb, Pb, Sr and Ti anomalies (Fig. 6a and 6b).

REE composition data are summarized in Table 2 and Figure 7. Phyllites, quartzphyllites and metatexites have almost identical normalised patterns (Fig. 7a), with all but one sample being included in a very limited concentration range (e.g. La = 41 to 61 ppm; Yb = 2.2 to 3.5 ppm). The exception is one metatexite sample (JTJ-60A) which stands out of the group, because of its lower REE contents (La = 18; Yb = 1.4), but yet yielding similar $(La/Yb)_N$ ratios (7.43 to 13.35). The Heavy Rare Earth Elements (HREE) are weakly fractionated (Dy/Yb_N = 1.07 – 1.35) and the Eu anomalies are small

(Eu/Eu* = 0.5 – 0.7). Diatexites and granites display a wide range of REE concentrations (Σ = 8 – 777 ppm) (Fig. 7b and 7c), despite the studied granites having similar normalised patterns across the different facies. At odds, diatexites have a wider variability, showing different degrees of HREE fractionation (Dy/Yb_N = 0.8 to 5) and Eu anomalies, either negative (down to 0.2; type-1 diatexites) or positive (up to 4; type-2 diatexites). See section 6.2 for more details on the chemical differences between these two types of diatexites.

5.2. Accessory minerals: trace element composition

5.2.1. Apatite

The trace element compositions of apatite grains from the FCR-LAC and their host rocks (phyllites) are remarkably distinct in Sr, Y, Th and REE compositions (Table 3; Fig. 8a-8e). The highest Sr content in apatite was found in phyllites (317 – 1471 ppm), decreasing gradually in metatexites (113 – 487 ppm), diatexites (86 – 144 ppm) and granites (74 – 99 ppm). Thorium behaves similarly. On the other hand, Y contents in apatite are low in phyllites (480 – 854 ppm), are quite similar between metatexites (837 – 1973 ppm) and diatexites (847 – 2026 ppm) and show a large range in granites (212 – 1546 ppm). Concerning their U composition, phyllites reveal lower values (8 – 34 ppm), while metatexites exhibit a larger variation (17 – 223 ppm), identical to that of diatexites (33 and 185 ppm). The maximum U concentration in the diatexites corresponds to a type-2 diatexite. The variation of U in granites is smaller, but within the same range of values as the migmatites (49 and 81 ppm).

Apatite grains are highly enriched in REE with ΣREE ranging from 1397 to 5829. They all show a marked enrichment in LREE compared to HREE, as depicted by $(La/Yb)_n$ ratios (Fig. 8f; phyllites = 5.1 – 32.6, metatexites = 0.6 – 3.7, diatexites = 0.6 – 6.8 and granites = 3.7 – 19.1, yet $(La/Sm)_n$ ratios are lower than the unity, except in IIγ

298 granite. At odds, apatite $(Tb/Lu)_n$ ratios are clearly higher than 1 for all the lithotypes.
299 The IIγ granite has a REE fractionation higher than the remaining granite facies,
300 because of its higher LREE contents. In general, Eu anomalies are negative with the
301 exception of the late-tectonic granite (granite IIγ: 1.06), which lacks an anomaly.
302
303 5.2.2. Zircon
304 Contents of Hf, Y, U, Th and HREE in zircon grains exhibit positive correlations with
305 those from the whole rock, indicating that zircon controls the budget of these elements
306 in migmatites and granites (Table 4; Fig. 13b and Fig. 13c). Hf contents are similar
307 between metatexites (8180 – 14410 ppm), diatexites (11060 – 12750 ppm) and
308 granites (10280 – 12670 ppm). Lu values decrease in zircon grains from metatexites
309 (48 – 309 ppm), to diatexites (48 – 91 ppm), and to granites (14 – 58 ppm). We were
310 only able to determine Y contents for half the measured points (11 out of 23). For the
311 available measurements, metatexites yield 120 – 2074 ppm, diatexites 610 ppm, and
312 granites range between 469 – 1199 ppm. U and Th contents are highly variable, with
313 Th/U ratios in zircon from diatexites (0.06 – 0.11) and granites (0.11 – 5.88) being
314 broadly higher than 0.1 (10 spots out of 12), whereas metatexites yield a wide range
315 (0.003 – 0.845), with half the analysed grains showing ratios lower than 0.1 (6 of the 11
316 spots).
317 Zircon from the different units exhibit high and similar ΣHREE concentrations, here
318 considered from Eu to Lu (Fig. 8g), ranging from 490 to 2430 ppm in metatexites, 488
319 to 1679 ppm in diatexites, and 261 to 2540 ppm in granites. They also show Eu
320 negative anomalies (metatexites 0.16 – 0.52, diatexites 0.14 – 0.33 and granites 0.02 –
321 0.16). On the other hand, zircon from the different FCR-LAC rocks show Ce positive
322 anomalies, suggesting high amounts of Ce in 4^+ valence, which allowed its greater
323 incorporation (Trail et al., 2012). Most zircon in the metatexites have La below the
324 detection limit, so to a better estimation of the REE fractionation, Ce/Yb_N is used. REE

fractionation values (Ce/Yb_N) in zircon retrieved from the metatexites are the most fractionated (Ce/Yb_N = 0.00001 – 0.05), while zircon from granites and diatexites clearly yield more elevated values (Ce/Yb_N = 0.01 – 0.4 and 0.001 – 0.04, respectively) (Fig. 8g). Overall, Lu/Hf ratios in zircon from the different units are variable, decreasing from metatexites (0.015), to diatexites (0.006) and granites (0.003).

5.3. Isotopic geochemistry

The radiogenic isotopes presented in this study were recalculated to 320 Ma, which corresponds to the migmatization age of the autochthonous domain of the CIZ (318 – 325 Ma, Martínez Catalán et al., 2014; Ferreira et al., 2019) (Table 5). While in the previous section, granites were presented as a single lithological group, in this section they are presented as syn-tectonic granites and late-tectonic granites (Ferreira et al., 2019). Likewise, phyllites are presented as phyllite N and phyllite S, depending if they were collected to the North (N) or South (S) of the anatectic complex.

5.3.1. Sr, Nd and Hf isotopic compositions

All migmatitic and granitic samples, except two, plot in the fourth quadrant (radiogenic Sr and less radiogenic Nd) of the $^{87}Sr/^{86}Sr_{320}$ vs. εNd_{320} diagram (Fig. 9a), implying time-integrated evolution characterized by enrichment of Rb and Nd relatively to the less incompatible Sr and Sm, respectively.

Granites share similar εNd_{320} values (-6.03 to -8.89), but significantly different $^{87}Sr/^{86}Sr_{320}$ ratios (0.7022 to 0.7126). These compositions are compatible with the upper continental crust (Chauvel et al., 2014; Hart et al., 1999). Overall, metatexite compositions are similar to those of granites with $^{87}Sr/^{86}Sr_{320}$ values ranging between 0.7039 and 0.7124 and εNd_{320} between -5.21 to -8.86.

The metasedimentary units, phyllite N ($^{87}Sr/^{86}Sr_{320}$ = 0.7153; εNd_{320} = -10.07) and phyllite S ($^{87}Sr/^{86}Sr_{320}$ = 0.7089; εNd_{320} = 3.28), have distinct compositions but both plot in the field defined for the Douro Group (see Teixeira, 2008). The phyllite S is also strikingly different from the FCR-LAC in terms of its Nd composition. Most granites and metatexites show similar compositions to that of the syn-tectonic Aguiar da Beira muscovite-biotite leucogranite (see Costa et al., 2014), while two samples of diatexite and one sample of metatexite have similarities with the Ollo de Sapo gneisses (see Montero et al., 2017; Fig. 9b).

The anatectic units have enriched Hf isotopic compositions that result in εHf_{320} ranging from -3.42 to -9.25. Except for facies IIγ (εHf_{320} = -3.99), granites have similar εHf_{320} compositions (-7.70 to -8.43). The peculiar composition of IIγ facies can be related to the fact that this granite is a 300 Ma late-tectonic granite, whereas the remaining granites are syn-tectonic, with ages between 313 and 317 Ma (Ferreira et al. 2019). Hf isotopic compositions of the metasedimentary units show distinct compositions (phyllite N with εHf_{320} = -13.68 and phyllite S with εHf_{320} = -7.16). The εNd_{320} *vs.* εHf_{320} diagram shows an overall positive correlation defined by the granites, metatexites and some diatexites (Fig. 9c). Despite some isotopic variability, two tight clusters are noticeable in the εNd_{320} *vs*. εHf_{320} diagram, each including granites, metatexites and type-1 diatexites. Type-2 diatexite reveals a εNd_{320} composition between the two clusters.

Phyllites, N and S, yield two-stage Nd model ages (TDM_2) of 1.83 Ga and 779 Ma, respectively. The range of Nd TDM_2 ages for the metatexites is 1.45 to 1.73 Ga, for the diatexites is 1.43 to 1.69 Ga, and for the granites is 1.51 to 1.73 Ga. The Hf TDM_2 ages are older, displaying the following values: phyllite N (2.16 Ga), phyllite S (1.75 Ga), metatexites (1.57 to 1.83 Ga), diatexites (1.51 to 1.88 Ga), and granites (1.54 to 1.83 Ga). These Nd and Hf model ages are similar for most of the anatectic complex lithologies (granites, diatexites, and metatexites). Nd TDM_2 for the phyllite S sample is

different and younger than the remaining analysed lithologies, and also somewhat different regarding its Hf TDM_2.

5.3.2. Pb isotopic composition

When recalculated to 320 Ma, the Pb isotopic ratios retrieved from phyllites become clustered onto one group with the remaining lithologies, in oppositition to what was shown for the Sr, Nd, and Hf isotopic systems in section 5.3.1. The $^{206}Pb/^{204}Pb_{320}$ and $^{207}Pb/^{204}Pb_{320}$ isotopic ratios tend to be almost identical for all lithologies ($^{206}Pb/^{204}Pb_{320}$ = 17.24 to 18.27 and $^{207}Pb/^{204}Pb_{320}$ = 15.61 to 15.67), with the exception of one metatexite outlier (Fig. 10a). In comparison, the $^{208}Pb/^{204}Pb_{320}$ isotopic ratio (36.67 to 39.39) is slightly more variable (Fig. 10b).

6. Discussion

6.1. Granite systematics

The intimate field relationship between granites, migmatites and metasediments in the FCR-LAC suggests a genetic link between these lithotypes. This is supported by the granites plotting close to ternary minimums in the Ab-Or-Q ternary diagram (Fig. 11c; Tuttle and Bowen, 1958; Winter, 2014). This points out to the S-type character of the studied granites, which is also suppported by their peraluminous character (ASI > 1.1) (Fig. 11a) and by their positioning in the A-B granite classification diagram of Villaseca et al. (1998) (Fig. 11b). Low CaO (0.2 – 1 wt.%), Na_2O (in general < 3.2 wt.%), and high K_2O (≈ 5 wt.%) contents, as well as $^{87}Sr/^{86}Sr_{320}$ ratios up to 0.7124 are also typical of S-type granites (Chappell and White, 1974). $^{87}Sr/^{86}Sr_{320}$ ratios are somewhat variable (0.7039 – 0.7124), reflecting variability between different granite facies. This variability, typical of S-type granites (Chappell and White, 2001), can be a

404 consequence of heteregeneous protoliths or reflect isotopic disequilibrium (see below).
405 The tight clustering of granites and migmatites in the εNd_{320} *vs*. εHf_{320} plot (Fig. 9c) puts
406 in evidence the cogenetic association amongst these units, which reinforces their
407 characterisation as S-type granites.

408 The abundant presence of perthites indicates the hypersolvus character of these
409 granites, compatible with relatively low H_2O pressure, which is also suggested by the
410 positionning between the ternary minimum defined at 0.1 and 0.2 GPa in the Ab-Or-Q
411 ternary diagram (Fig. 11c).

412

413 6.2. The diatexite-granite link

414 In an anatectic complex, diatexites are regarded as the result of melting processes
415 which by melt aggregation, migration, and emplacement give rise to granitic intrusive
416 bodies (Milord et al., 2001). Diatexites in the FCR-LAC are characterized by a
417 significant compositional variability, which can provide clues on the shared genetic link
418 with granites.

419 Major and trace element concentrations were used to geochemically separate
420 distinct types of diatexites: type-1 (SiO_2 = 68 – 74 wt%) and type-2 (SiO_2 =74 – 75
421 wt%), whereas granites (SiO_2 = 70 – 75 wt%) are generally less silica-enriched than
422 type-2 diatexites. Using the Frost et al. (2001) diagram, type-1 diatexites and granites
423 are alkali-calcic to alkalic, whereas type-2 diatexites range between the alkali-calcic
424 and calc-alkalic (Fig. 11d). Regarding trace element compositions, type-2 diatexites
425 also stand out by their lower Rb (145 – 238 ppm) (Fig. 5a) and higher Yb and Lu
426 concentrations (Fig. 6b), and flat Tb to Yb patterns (Tb/Yb_N = 0.8 – 1.5) (Fig. 7b), at
427 odds with what can be observed in the other diatexites and granites (Fig. 7b and 7c)
428 (Tb/Yb_N > 2.64). In addition, type-1 diatexites exhibit fractionated HREE (Dy/Yb_N = 2 -
429 5) and Eu negative anomalies (0.2 – 0.7), in contrast with type-2 diatexites, which

reveal unfractionated HREE (Dy/Yb_N = 0.8 - 1) and Eu anomalies from slightly negative to strongly positive (0.6 – 4).

Comparing both types of diatexites with granites, it is evident the similarity between granites and type-1 diatexites. Taking into account the differences between these two types of diatexites, type-2 could correspond to cumulates of quartz and feldspar that evolved isolated from type-1 diatexites and granites through an earlier fractional crystallization process (e.g. Brown et al., 2016; Morfin et al., 2014; Sawyer, 1987). The Hf isotopic signatures of these two types of diatexites are clearly distinct, with εHf_{320} of the type-2 diatexites being significantly less radiogenic (up to 6 units; Table 5) than the reported for type-1 diatexites and also for the studied granites. Thus, the Hf isotopic data reinforces the idea of existing two distinct types of diatexites and of a genetic link between type-1 diatexites and granites, which is not so obvious when type-2 diatexites are considered. The role of melting reactions in this variability is potentially significant and is discussed in the following section.

Taking into account the referred isotope similitude with granites (see above), type-1 diatexites are here considered as related to the granites by melt-residuum separation. This process is evident in the Harker diagrams (Fig. 4), where this type of diatexites are tendentially more rich in FeO^t, MgO, TiO_2 and Al_2O_3, but comparatively depleted in K_2O, Na_2O and SiO_2 than the associated granites.

6.3. Melting reactions

The formation of migmatite-granite complexes is the culmination of high-grade metamorphism during orogenic events. Partial melting is a sequential process where the production and accumulation of melt gradually increases with time. As prograde reactions take place, melting of the protolith lead to the formation of metatexitic and diatexitic migmatites, culminating with a granitic melt at higher melt fractions (Brown, 2013). Melting reactions can take place at different temperatures, pressures and water

457 contents. Typically, pelitic and greywacke protoliths begin to melt at about 650-700 ºC
458 in the presence of an aqueous fluid (fluid-present reactions), producing up to 60 vol.%
459 of melt (Brown, 2013; Milord et al., 2001; Vielzeuf and Holloway, 1988; Weinberg and
460 Hasalová, 2015). During the prograde metamorphic path, as temperature increases to
461 ca. 800-1000 ºC, partial melting can occur in the absence of an external fluid, giving
462 place to a series of fluid-absent reactions by dehydration of hydrous minerals, such as
463 micas and amphiboles, which progressively increases melt production up to 70 modal
464 percent melt (Brown, 2013; Bucher and Grapes, 2011; Yakymchuk and Brown, 2014).
465 Field observations combined with major element geochemistry of the FCR-LAC
466 units show that the most probable protolith of the granitic melts (s.l.) is of sedimentary
467 origin (see sections 2 and 6.1). Moreover, the major elements geochemistry, in
468 particular the CaO/Na_2O ratio, reinforces the idea that FCR-LAC granites are derived
469 from pelitic melts ($CaO/Na_2O < 0.3$; Jung and Pfänder, 2007) (Fig. 12a). The type of
470 melting reactions can be inferred based on trace-element modelling using Rb, Ba, Sr
471 (Inger and Harris, 1993) and taking into account the mineral assemblages of the FCR-
472 LAC rocks (section 3). Yet, the exact reaction cannot be accurately determined given
473 its high dependence on the chemical and modal composition of the protolith, which in
474 the present study is thought to be significantly heterogeneous on basis of several
475 evidences (sections 6.5 and 6.6; Teixeira, 2008). In this way, we can infer that melting
476 of the pelitic source was mainly controlled by two consecutive reactions leading to the
477 progressive increase of melt production.
478 It has been shown that fluid-present and fluid-absent reactions produce melts with
479 distinct characteristics for some key trace-elements, which are constrained by relative
480 mass proportions of consumed feldspar and mica (Inger & Harris, 1993; Gao et al.,
481 2017; Dou et al., 2019). The role of these two reaction types on the evolution of the
482 studied anatectic complex (FCR-LAC) is well evident on diagrams involving elements
483 compatible with plagioclase or muscovite (Fig. 12b; Fig. 12c).

The operation of fluid-present reaction is characterized by the development of evolution trends with almost constant Rb/Sr ratios but highly variable Sr and Ba contents (e.g. Gao et al., 2017; Dou et al., 2019), which at FCR-LAC (Fig. 12b and 12c) encompass phyllites and most of the metatexites.

Petrographic observations indicate that the metatexite melanosomes are characterized by a lower plagioclase/muscovite proportion than the phyllites from where they are considered to have been derived. This suggests that the following fluid-induced key reaction (Patiño Douce and Harris, 1998; Weinberg and Hasalová, 2015) occurred during the initial steps of melting:

$$9\ \text{muscovite} + 15\ \text{plagioclase} + 7\ \text{quartz} + x\ H_2O \rightarrow 31\ \text{melt} \quad (1)$$

Increase of Rb/Sr ratios from phyllite, to metatexite, and to diatexite/granite and the higher Sr and Ba in metatexites in comparison with diatexite/granite (Fig. 12b) seem to support that early partial melting and melt segregation (phyllites to metatexite formation) resulted from such congruent fluid-present reaction (1), consuming plagioclase in larger quantities than muscovite (see also Dou et al., 2019; Gao et al., 2017; Martini et al., 2019).

As temperature increases during prograde metamorphism, fluid-absent melting can take place by the consumption of hydrous minerals, such as micas. A significant increase of Rb/Sr ratios accompanied by a decrease of Sr and Ba is observed for granites and most type-1 diatexites (Fig. 12b and 12c), suggesting dehydration-melting involving the significant consumption of muscovite and crystallization of peritectic minerals, such as K-feldspar and sillimanite, in a reaction that could have been similar to (2) (Patiño Douce and Harris, 1998; see also Gao et al., 2017; Inger and Harris, 1993; Yang et al., 2019):

$$25\ \text{muscovite} + 7\ \text{plagioclase} + 8\ \text{quartz} \rightarrow 5\ \text{K-feldspar} + 5\ \text{sillimanite} + 25\ \text{melt} \quad (2)$$

This reaction also involves the crystallization of peritectic minerals, such as K-feldspar and sillimanite. This agrees with the absence of primary muscovite in type-1 diatexites and granites, as well as the abundance of K-feldspar and sillimanite. Reaction (2) also explains the negative Eu anomalies characterizing most of type-1 diatexites and granites (Eu/Eu* down to 0.2), which can be explained by the crystallization of peritectic K-feldspar (Fig. 12d; Dou et al., 2019; Gao et al., 2017).

After fluid-absent reactions involving the consumption of muscovite, it is commonly described the dehydration-melting of biotite as a response to temperature increase along the metamorphic path. There is some petrographic evidence stemming from migmatites for the breakdown of biotite, such as the occurrence of biotite crystals with corroded borders. However, reactions involving the melting consumption of biotite are accompanied by the peritectic production of garnet (> 0.4 GPa) or cordierite (< 0.4 GPa) (Spear et al., 1999; Bento dos Santos et al., 2011). Such minerals were not detected in the studied samples, although garnet has been reported (Díez Fernández and Pereira, 2016), and therefore some incipient melting of biotite should have occurred.

We demonstrated before the existence of two geochemically distinct types of diatexites (see section 6.2) and that type-1 diatexites were derived from fluid absent reactions (2) associated to the dehydration-melting of muscovite. Type-2 diatexites exhibit positive Eu anomalies (Eu/Eu* up to 4), but low CaO contents and Rb/Sr ratios (Fig. 12b; 12c), compared to the remaining granites and type-1 diatexites. This implies that peritectic K-feldspar was not formed or only crystallized in small proportions (Dou et al., 2019; Gao et al., 2017), and, instead, another process must have been important. Fluid-fluxed melting of muscovite (reaction 1) is a more likely mechanism to generate melts with compositions similar to type-2 diatexites. The melt productivity of such reaction is dependent on the amount of fluid present in the rock. The lower abundance of type-2 diatexites and the lack of granites with compositions compatible

with this type of diatexites suggest that the amount of melt generated by that fluid-present reaction was not enough to promote the melt segregation/extraction needed to granite generation. This suggests that the amount of fluid in the source rock was small. Yet, as mentioned in section 6.2, the relative higher silica content in type-2 diatexites suggests that their composition probably reflect, in addition, the occurrence of some fractional crystallization.

Ti-in-zircon temperatures from young zircon grains within the syn-tectonic granites range between 783 – 836 ºC (Ferreira et al., 2019), implying that the metamorphic peak reached such temperatures. Additionally, this range of estimated melt temperatures are consistent with the minimum metamorphic peak temperature previously calculated from mineral equilibria for the FCR-LAC (T = 761 ± 50 ºC; Pereira et al., 2017). At this temperature range, up to 60% volume of melt is produced by the referred partial melting reactions (Vielzeuf and Holloway, 1988), thus allowing significant melt extraction given that the critical melt percentage for melt migration (20 to 35% volume; e.g. Clemens and Vielzeuf, 1987 and Bento dos Santos et al., 2011a; ≤7%; Rosenberg and Handy, 2005 and Brown, 2013) is clearly surpassed.

6.4. The role of accessory minerals

Accessory minerals have an important role controlling the composition of trace elements and isotopic ratios in migmatites and granites (e.g. Ayres and Harris, 1997; Bea, 1996a, 1996b; Bea et al., 1994; Yakymchuk and Acosta-Vigil, 2019; Zeng et al., 2005a). Apatite and zircon are the main accessory minerals that occur in the FCR-LAC rocks and their trace element compositions are described in section 5.2.

Results demonstrate that apatite is the main carrier of LREE and Y in the FCR-LAC (Table 3) and exhibits a flat REE pattern (more evident for LREE; Fig. 8a), typical of peraluminous rocks (Bea, 1996a). The moderate LREE and P_2O_5 covariation observed

566 in the whole-rock geochemistry (Fig. 13a) confirm the control that apatite has in the
567 variation of these elements.

568 Conversely, the HREE composition of the anatectic rocks is mainly influenced by
569 zircon (Table 4). This influence is also confirmed by the covariation between HREE and
570 Zr/Hf from the whole-rock geochemistry (Fig. 13b-d). Granites show depletion in the
571 HREE and lower Lu/Hf ratios when compared to metatexites and the country rocks,
572 which is due to the role of zircon. Indeed, Lu is preferentially retained in restitic zircon
573 grains during partial melting, resulting in a constant decrease of the Lu concentration
574 and Lu/Hf ratio in subsequent crystallised zircons.

575 Inherited zircon grains are quite common in all these granites, indicating survival of
576 significant amounts of zircon, in agreement with partial melting experimental data.
577 Indeed, considering an average Zr bulk-rock composition of 150 ppm (Table 2), an
578 estimated maximum melting temperatures of ~840 ºC (section 6.3) and an approximate
579 1:1 proportion of metapelite and greywacke in the protolith, only about 15% of zircon is
580 expected to dissolve into the melt (Yakymchuk et al., 2017).

581 Apatite grains found in the metasedimentary units are highly enriched in LREE (La
582 up to 1595 ppm) and Th (up to 97 ppm), which is a typical feature of magmatic apatite
583 (Henrichs et al., 2018). Therefore, it is plausible that these correspond to detrital
584 magmatic-derived apatite grains. The recrystallization of apatite during prograde
585 metamorphism can explain the relative depletion of LREE (La ≤ 405 ppm) in the
586 metatexitic apatite, typical of metamorphic apatites (Henrichs et al., 2018).

587

588 6.5. Isotope variability

589 The studied rocks form two tight clusters in the εHf_{320} vs. εNd_{320} diagram (Fig. 9c) ,
590 each of them comprising metatexites, diatexites and granites. Sm, Nd, Lu and Hf, the
591 parent and daughter elements of the Nd and Hf isotopic systems, are all characterized
592 by high field strengths, which confer them a significant degree of immobility during

meteoric and metamorphic processes. Considering this, such clusters clearly suggest the existence of two somewhat distinct sources for the FCR-LAC anatectic complex, in agreement with the significant isotopic variability of the DBSG phyllites (Teixeira, 2008). Additionally, the fact that each of the clusters comprise metatexites, diatexites and granites suggests that during the metatexite-diatexite-granite evolution partial melting was not accompanied by significant isotopic disequilibrium, like those caused by the incomplete melting of zircon and the consequent variable release of zircon unradiogenic ^{177}Hf and non-zircon Hf during melting (the zircon effect; Tang et al., 2014). Considering the very long half-life of ^{176}Lu (37.1 Ga) and ^{147}Sm (106 Ga) and the lack of evidence for isotopic disequilibrium, protolith minerals must have had a comparatively short time period for developing distinct isotopic signatures. Alternatively, their isotopic compositions may have been homogenised during the high-grade metamorphism path preceding anatexis itself (Wolf et al., 2019). The occurrence of restricted isotopic disequilibrium during the first melting stages that led to the formation of the metatexites should not be discarded. However, given the natural isotopic variability of the probable source rocks (e.g. Teixeira, 2008) the most likely explanation for the isotopic variability in the migmatite-granites is source heterogeneity. Below we will focus on the metatexite-diatexite-granite compositional transitions.

It should be noticed that the present-day values (ε_0) show a distinct behaviour for the isotope systems in consideration. Indeed, inside of each of the two groups, enclosing metatexites/diatexites/granites, a significantly larger variation is observed for the εHf_0 values than for εNd_0 (Fig. 14a). Considering this and the fact that in the εHf_{320} vs. εNd_{320} diagram (Fig. 9c) two clusters are observed comprising granites and migmatites, we propose that a significant fractionation between Hf and Nd isotopic systems occurred during melting reactions from metatexites to diatexites and finally to granites, caused by a distinct behaviour of their parent/daughter pairs. As shown before (6.3), the melting process involved essentially micas and plagioclase, phases with no capability to significantly fractionate Sm from Nd or Lu from Hf, thus suggesting the role

621 of an accessory phase to explain this different behaviour. Apatite in peraluminous
622 systems has $D^{Sm/Nd} \approx 0.3$ and and $D^{Lu/Hf} \approx 70$ (Bea et al., 1994), making it a good
623 candidate. However, εNd_0 of granite-metatexite pairs is similar or only slightly varying,
624 which would not be expected, and apatite dissolution during melting reactions would
625 induce an increase of $^{176}Hf/^{177}Hf$ by radiogenic ingrowth of ^{176}Hf with time, opposite to
626 what it is observed.. Therefore, decoupling of Lu and Hf cannot be attributed to apatite
627 dissolution. The observed decoupling of Hf and Nd isotopic systems can be achieved
628 by the involvement of zircon. Zirconium and Hf are usually considered as two
629 geochemically coherent elements, which explains the very high D_{Hf} characterizing
630 zircon ($D_{Hf} \approx 2420$; Wang et al., 2010). The consequent very low Lu/Hf ratios
631 characterizing zircon will allow, that by incomplete melting of zircon, Lu/Hf in the melt to
632 be distinct of that of the whole source rock, and that granites would evolve with time to
633 lower $^{176}Hf/^{177}Hf$ ratios than the less evolved metatexites. Moreover, variable zircon
634 contribution to melt will contribute to the production of liquid batches characterized by
635 significantly different Lu/Hf ratios. This would be facilitated by incomplete zircon
636 dissolution, a process which has been demonstrated to frequently occur in
637 peraluminous granitic magmas where zircon saturation occurs at relatively low Zr
638 concentrations (~78 ppm; Harrison and Watson, 1983; Hogan and Sinha, 1991; Tang
639 et al., 2014) and, also, by the fact that zircon is preferentially located inside biotite
640 which can protect it from dissolution (Bea, 1996) (see also 6.4). In opposition to the
641 observed for Lu/Hf ratios, zircon only have a limited capability to fractionate Sm from
642 Nd ($D_{Sm/Nd} \approx 1$; Bea et al 1994), thus explaining the contrasting behaviour of Hf and Nd
643 present day isotope ratios depicted on Fig. 14a).

644 Each of the FCR-LAC metatexite/diatexite/granite groups defined on the εHf_{320} vs.
645 εNd_{320} diagram (Fig. 9c) display a significant present-day $^{87}Sr/^{86}Sr$ range at almost
646 constant εNd (Fig. 14b). This suggests that Sr isotope signatures evolved under distinct
647 $^{87}Rb/^{86}Sr$, allowing radiogenic ingrowth of ^{87}Sr at different rates. At odds with the Nd

and Hf systems, which are mainly controlled by the solubility of accessory phases, in the Rb/Sr system the melt composition is constrained by the major mineral phases involved in the melting reactions (Tang et al., 2014; Wolf et al., 2019). In fact, an increase of $(^{87}Sr/^{86}Sr)_0$ from metatexites to diatexites and then to granites is observed (Fig. 14b), which indicates an increase of $^{87}Rb/^{86}Sr$ in the melts progressively generated at higher temperatures. If we take into account the melting reactions inferred for the FCR-LAC (as in section 6.3), it is expected firstly a significant contribution of muscovite to the melt (reactions 1 and 2) and later a minor contribution of biotite, a mineral usually characterized by significantly higher Rb/Sr than coexisting muscovite (e.g. Neiva et al., 2002), which together can explain these isotopic ranges and evolutions.

Nonetheless, the range in Sr isotopes is observed even when the initial values $(^{87}Sr/^{86}Sr)_{320}$ are considered (Fig. 9a). There are several ways to explain variation on the initial Sr isotopic composition: isotopic disequilibrium, hydrothermal alteration, assimilation/fractional crystallization (AFC), and source heterogeneity.

Isotopic disequilibrium taking place during the melting stages involving various minerals characterized by significantly distinct $^{87}Rb/^{86}Sr$ (plagioclase, muscovite, biotite) is a plausible mechanism, especially in these settings (crustal anatexis). However, these isotopic signatures had to be developed previously to melting to account for variable mineral $^{87}Sr/^{86}Sr$ during radiogenic ingrowth (Farina and Stevens, 2011; Zeng et al., 2005b). Yet, at odds with the commonly observed in situations of isotopic disequilibrium (e.g. Wolf et al., 2019), no systematic isotopic variation is observed when considered the different lithotypes (metatexites, diatexites, and granites), but only a significant overlapping of the $^{87}Sr/^{86}Sr_{320}$ characterizing metatexites and granites. In this perspective, the $^{87}Sr/^{86}Sr_{320}$ variability could likely just be the result of open-system processes, such as hydrothermal alteration and/or assimilation/fractional crystallization (AFC). A hydrothermal overprint on these units would result in a lack of correlation between mobile and high field strength immobile

676 elements, such as LILE and Ti, respectively (e.g. Huang et al., 2019). This is not
677 supported by our data, which show a clearly linear correlation between K, Sr, Ba *vs.*
678 TiO_2 (Fig. 15a-c). Therefore, $^{87}Sr/^{86}Sr_{320}$ variability as a result of post-magmatic
679 overprint is not plausible.

680 AFC is not a very probable process in constraining the chemical variability of S-type
681 granitic systems (Clemens and Stevens, 2012; Yakymchuk, 2019). Indeed, as
682 suggested by Castro (2014), the small difference in density between melt and minerals
683 precociously crystallised, as well as the high viscosity of high silica melts, lead to
684 consider as probably small and inefficient the role of fractional crystallization on granitic
685 magmas. In addition, it has been considered, based on thermodynamics, that granitic
686 melts have a limited capability of assimilation of crustal rocks, which is more evident for
687 relatively low-temperature S-type magmas like those in this study (e.g. Glazner, 2007).
688 In agreement, no positive correlation is observed for the studied rocks between La/Sm
689 and Th/Sc (Fig. 15d), both ratios being expected to increase during AFC processes
690 (Huang et al., 2019).

691 Given the lack of evidence for Sr isotopic disequilibrium and for the occurrence of
692 hydrothermal alteration or AFC processes, the large variability of the $^{87}Sr/^{86}Sr_{320}$ was
693 most probably caused by source heterogeneity. This is in agreement with geochemical
694 studies of the DBSG phyllites which have shown a much larger heterogeneity of the Sr
695 isotope ratios than the observed for $^{143}Nd/^{144}Nd$ (Teixeira, 2008), and in line with
696 Clemens and Stevens (2012) and Yakymchuk (2019) findings, who concluded that
697 source heterogeneity is an important factor on isotopic variations in granites in as much
698 it controls the type of peritectic minerals that will form.

699 On the $^{207}Pb/^{204}Pb$ vs $^{206}Pb/^{204}Pb$ diagram (Fig.14c), the studied rocks define a linear
700 array close to the evolution line modelled for the upper continental crust by Zartman
701 and Doe (1981). However, a significantly larger dispersion is observed in the
702 $^{208}Pb/^{204}Pb$ vs. $^{206}Pb/^{204}Pb$ (Fig. 14d and Fig. 10b), suggesting decoupling of ^{206}Pb and
703 ^{207}Pb (the final products of the decay chains of ^{238}U and ^{235}U, respectively) from ^{208}Pb,

704 the final radiogenic product of ^{232}Th. In granitic systems, the elemental Pb budget is
705 mainly controlled by K-feldspar, whereas accessory phases are the main repositories
706 of U and Th (e.g. Bea, 1996), which have the ability to strongly influence the long-term
707 lead isotope evolution (Hogan and Sinha, 1991; Wolf et al., 2019). Decoupling of
708 uranogenic lead from thorogenic lead (Fig. 10b) may then reflect the variable modal
709 proportions of these phases in the source materials and also the variable contribution
710 to melts of U-rich (e.g.: zircon, apatite and monazite) and Th-rich (e.g.: monazite and
711 apatite) minerals.
712
713 6.6. Source rocks: some considerations
714 Based on the whole-rock geochemistry (e.g. Harker diagrams; Fig. 4 and 5), we can
715 distinguish the geochemical evolution due to partial melting and the progressive
716 residuum-melt separation, with the metapelitic rocks (phyllites) plotting at the origin of
717 the metatexite-diatexite-granite sequence. This relationship is in clear agreement with
718 field-based observations (as seen in section 3).
719 Despite the isotopic differences/variability between the phyllite N and phyllite S
720 (Douro-Beiras Supergroup; Fig. 9b; Teixeira, 2008), and even among the anatectic
721 complex lithologies, the Sr, Nd, and Hf isotopic compositions show a clear affinity
722 between migmatites and phyllites. This is more evident for the phyllite N sample with Sr
723 and Nd signatures within the range of the FCR-LAC units (Fig. 9a and Table 5), than
724 for the phyllite S sample, where only the Hf initial composition is within analytical
725 uncertainty of the remaining anatectic units (Fig. 9c and Table 5). TDM_2 provenance
726 ages of the metasedimentary protoliths of the anatectic complex broadly agree with the
727 phyllite units TDM_2 ages (Table 5), which reinforces the Douro-Beiras Supergroup as
728 representing the most probable protolith.
729 While we can not go too far beyond out current small dataset to draw further links
730 between a definitive source to this anatectic complex (either phyllite N or phyllite S), it

731 seems reasonable to propose a stronger affinity with the Douro Group, sampled to the
732 N. However, we cannot fully discard the involvement of the southern Beiras Group
733 units (Tassinari et al., 1996) nor a minor contribution from the Ollo de Sapo magmatic
734 rocks (Montero et al., 2017), particularly when the Nd initial isotopic compositions are
735 taken into account (Fig. 9b). This is particularly the case of the IIγ late-tectonic granite,
736 which exhibits isotopic compositions significantly different from the syn-tectonic
737 granites (Fig. 9a and 9c; see Ferreira et al., 2019 for granite ages).

738 The contrasting Nd and Hf isotopic results between phyllites sampled from the
739 northern (εNd_{320} = -10.07) and southern (εNd_{320} = +3.28) domains are striking, but in
740 agreement with previously published data for the CIZ metasediments (Villaseca et al.
741 (2014). This suggests source heterogeneities between both domains, with variable
742 detrital inputs (more and less evolved crustal sources), which influenced the isotopic
743 composition of the FCR-LAC units.

744 Further work is needed to clearly demonstrate: a) a systematic isotopic variability
745 between the metasedimentary units to the North and South of the FCR-LAC; and b) the
746 affinity of the anatectic complex with the Douro Group. This will further elucidate if the
747 JPCSZ was a major paleogeographic boundary during the Precambrian/Cambrian, as
748 proposed by Villaseca et al. (2014) and Iglesias and Ribeiro (1981).

749 ## 7. Conclusions

750 This study shows the links between the distinct lithologies of the variscan Figueira
751 de Castelo Rodrigo – Lumbrales Anatectic Complex of the Central Iberian Zone and
752 evaluates the occurrence of isotopic disequilibrium during melting reactions from
753 metatexites to diatexites and granites. The main conclusions are summarized below:

754 1) Based on whole-rock elemental and isotopic geochemistry a genetic link is
755 definitively established between metatexites, diatexites and granites, which
756 represent different evolutionary stages of the anatectic complex, culminating on
757 the genesis of the S-type granites.

2) We demonstrate the existence of two geochemically distinct diatexite groups (type-1 and type-2) generated at different stages of the partial melting process. We show that type-1 diatexite, with high Rb concentration and fractionated HREE is geochemically similar to the regional S-type granites, whereas type-2 diatexites are not linked to any of the outcropping granites.

3) Based on the mineral assemblage and whole-rock geochemistry we demonstrated that type-1 diatexites—and granites were produced during dehydration-melting of muscovite and production of peritectic K-feldspar and sillimanite plus melt. On the contrary, Rb-poor, unfractionated HREE type-2 diatexites required influx of externally derived fluids during melting, which consumed more plagioclase than muscovite. The type-2 diatexites represent a more evolved melt composition than the outcropping granites, being mainly composed by quartz and feldspar.

4) Evidence of incipient biotite melting and Ti-in-zircon thermometry allow to establish peak temperatures ranging from 783 to 836 ºC. These conditions resulted in the production of large volumes of melt, which explains the profusion of S-type granites within the CIZ.

5) There are no signs of significant isotopic disequilibrium during melting in the transition from metatexites to diatexites and, finally, to granites. This means that the source minerals were in isotopic equilibrium at the onset of the melting process, either reflecting that they were formed shortly before melting, or, alternatively, that isotopic homogenization during the high-grade metamorphism preceding the melting process took place. However, the distinct contributions of mineral phases to the melt produced batches of melt with distinct parent/daughters' ratios, which resulted in distinct radiogenic ingrowth, and explain the present-day isotopic heterogeneity found in these units.

6) Rb/Sr ratios and the Pb budget of the successively generated lithotypes were mainly controlled by major minerals such as muscovite, K-feldspar and

plagioclase. The accessory phases were the main minerals controlling the Sm/Nd, Lu/Hf ratios and the U and Th contents.

7) Two distinct groups, both comprising metatexites, diatexites and granites, were identified when comparing the initial isotopic ratios, testifying for the existence of source heterogeneity. This is consistent with the isotopic variability of metasediments considered to be the sources of the anatectic complex and may also explain the differences in the initial Hf and Nd isotopic compositions between late-tectonic granite-migmatite cluster and the syn-tectonic granite-migmatite cluster.

8) The genetic links with probable protoliths of the anatectic complex were also explored. We showed that anatectic complex is sourced on the Neoproterozoic/Lower Cambrian Douro-Beiras Supergroup, with possible minor contribution of the Ordovician Ollo de Sapo magmatic rocks.

Acknowledgements: The corresponding author thanks the financial support of Fundação para a Ciência e Tecnologia (FCT) through a doctoral grant (PD/BD/114486/2016). The authors would also like to acknowledge the financial support of FCT through project UIDB/50019/2020 – IDL. Inês Pereira acknowledges a PhD bursary awarded by the University of Portsmouth. We would also like to thank the University of Portsmouth for the access to their analytical facilities, including sample preparation, SEM and LA-ICP-MS instruments. We also acknowledge Editor Marco Scambelluri, Chris Yakymchuk and Bruna Carvalho for their important inputs to this article.

References

Alves Ribeiro, J., Monteiro-Santos, F.A., Pereira, M.F., Díez Fernández, R., Dias da Silva, Í., Nascimento, C., Silva, J.B., 2017. Magnetotelluric imaging of the

lithosphere across the Variscan Orogen (Iberian autochthonous domain, NW Iberia). Tectonics. https://doi.org/10.1002/2017TC004593

Areias, M., Ribeiro, M.A., Santos, J.F., Dória, A., 2014. LP-HT anatectic processes and lithological heterogeneity in the Mindelo Migmatite Complex (NW Portugal). Estud. Geológicos 70, 1–20. https://doi.org/10.3989/egeol.41730.323

Ayres, M., Harris, N., 1997. REE fractionation and Nd-isotope disequilibrium during crustal anatexis: constraints from Himalayan leucogranites. Chem. Geol. 139, 249–269. https://doi.org/10.1016/S0009-2541(97)00038-7

Barbero, L., Villaseca, C., Rogers, G., Brown, P.E., 1995. Geochemical and isotopic disequilibrium in crustal melting: an insight from the anatectic granitoids from Toledo, Spain. J. Geophys. Res. 100. https://doi.org/10.1029/95jb00036

Bea, F., 1996a. Residence of REE, Y, Th and U in granites and crustal protoliths; implications for the chemistry of crustal melts. J. Petrol. 37, 521–552. https://doi.org/10.1093/petrology/37.3.521

Bea, F., 1996b. Controls on the trace element composition of crustal melts. Trans. R. Soc. Edinb. Earth Sci. 87, 33–41. https://doi.org/10.1017/S0263593300006453

Bea, F., Pereira, M.D., Stroh, A., 1994. Mineral/leucosome trace-element partitioning in a peraluminous migmatite (a laser ablation-ICP-MS study). Chem. Geol. 117, 291–312. https://doi.org/10.1016/0009-2541(94)90133-3

Bento dos Santos, T., Rodrigues, J.F., Castro, P., Meireles, C., Ferreira, N., Ferreira, P., Ferreira, J.A., Pereira, I., Ribeiro, A., Pereira, E., Guimarães, F., n.d. Exhumation of an anatectic complex by channel flow and extrusion tectonics: structural and metamorphic evidence from the Porto – Viseu Metamorphic Belt, Central-Iberian Zone. Int. J. Earth Sci.

Bento dos Santos, T.M., Munhá, J.M., Tassinari, C.C.G., Fonseca, P.E., 2011a. The

838 link between partial melting, granitization and granulite development in central
839 Ribeira Fold Belt, SE Brazil: New evidence from elemental and Sr-Nd isotopic
840 geochemistry. J. South Am. Earth Sci. 31, 262–278.
841 https://doi.org/10.1016/j.jsames.2011.01.004

842 Bento dos Santos, T.M., Munhá, J.M., Tassinari, C.C.G., Fonseca, P.E., Neto, C.D.,
843 2011b. Metamorphic P-T evolution of granulites in the central Ribeira Fold Belt,
844 SE Brazil. Geosci. J. 15, 27–51. https://doi.org/10.1007/s12303-011-0004-1

845 Blichert-Toft, J., Albarède, F., 1997. The Lu-Hf isotope geochemistry of chondrites and
846 the evolution of the mantle-crust system. Earth Planet. Sci. Lett. 148, 243–258.
847 https://doi.org/https://doi.org/10.1016/S0012-821X(97)00040-X

848 Brown, C.R., Yakymchuk, C., Brown, M., Fanning, C.M., Korhonen, F.J., Piccoli, P.M.,
849 Siddoway, C.S., 2016. From source to sink: Petrogenesis of cretaceous anatectic
850 granites from the Fosdick migmatite-granite complex, West Antarctica. J. Petrol.
851 57, 1241–1278. https://doi.org/10.1093/petrology/egw039

852 Brown, M., 2013. Granite: From genesis to emplacement. Bull. Geol. Soc. Am. 125,
853 1079–1113. https://doi.org/10.1130/B30877.1

854 Bucher, K., Grapes, R., 2011. Petrogenesis of Metamorphic Rocks 8th Edition, Journal
855 of Chemical Information and Modeling. https://doi.org/10.1007/978-3-540-74169-5

856 Burg, J.-P., Van den Driessche, J., Brun, J.-P., 1994. Syn-to post-thickening extension
857 in the Variscan Belt of Western Europe: Modes and structural consequences.
858 Géologie la Fr. 3, 33–51.

859 Carríngton da Costa, J., Teixeira, C., 1957. Carta Geológica de Portugal, na escala
860 1/50.000, Notícia Explicativa da Folha 9-C. Serviços Geológicos Port. 39 pp.

861 Castro, A., 2014. The off-crust origin of granite batholiths. Geosci. Front. 5, 63–75.
862 https://doi.org/10.1016/J.GSF.2013.06.006

863 Chappell, B.W., White, A.J.R., 2001. Two contrasting granite types: 25 years later.
864 Aust. J. Earth Sci. 48, 489–499.

865 Chappell, B.W., White, A.J.R., 1974. Two contrasting granite types. Pacific Geol. 8,
866 173–174.

867 Chauvel, C., Garçon, M., Bureau, S., Besnault, A., Jahn, B., Ding, Z., 2014. Constraints
868 from loess on the Hf – Nd isotopic composition of the upper continental crust.
869 Earth Planet. Sci. Lett. 388, 48–58. https://doi.org/10.1016/j.epsl.2013.11.045

870 Clemens, J., 2006. Melting of the continental crust: Fluid regimes, melting reactions,
871 and source-rock fertility, Evolution and Differentiation of the Continental Crust.

872 Clemens, J.D., Stevens, G., 2012. What controls chemical variation in granitic
873 magmas? Lithos 134–135, 317–329. https://doi.org/10.1016/j.lithos.2012.01.001

874 Clemens, J.D., Vielzeuf, D., 1987. Constraints on melting and magma production in the
875 crust. Earth Planet. Sci. Lett. 86, 287–306. https://doi.org/10.1016/0012-
876 821X(87)90227-5

877 Costa, M.M., Neiva, A.M.R., Azevedo, M.R., Corfu, F., 2014. Distinct sources for
878 syntectonic Variscan granitoids: Insights from the Aguiar da Beira region, Central
879 Portugal. Lithos 196–197, 83–98. https://doi.org/10.1016/j.lithos.2014.02.023

880 Davies, G.R., Tommasini, S., 2000. Isotopic disequilibrium during rapid crustal
881 anatexis: Implications for petrogenetic studies of magmatic processes. Chem.
882 Geol. 162, 169–191. https://doi.org/10.1016/S0009-2541(99)00123-0

883 Dias, R., Ribeiro, A., 1995. The Ibero-Armorican Arc: A collision effect against an
884 irregular continent? Tectonophysics 246, 113–128. https://doi.org/10.1016/0040-
885 1951(94)00253-6

886 Dias, R., Ribeiro, A., Romão, J., Coke, C., Moreira, N., 2016. A review of the arcuate
887 structures in the Iberian Variscides; constraints and genetic models.

888 Tectonophysics 681, 170–194. https://doi.org/10.1016/j.tecto.2016.04.011

889 Díez Fernández, R., Pereira, M.F., 2016. Extensional orogenic collapse captured by
890 strike-slip tectonics: Constraints from structural geology and U[sbnd]Pb
891 geochronology of the Pinhel shear zone (Variscan orogen, Iberian Massif).
892 Tectonophysics 691, 290–310. https://doi.org/10.1016/j.tecto.2016.10.023

893 Dou, J., Siebel, W., He, J., Chen, F., 2019. Different melting conditions and
894 petrogenesis of peraluminous granites in western Qinling, China, and tectonic
895 implications. Lithos 336–337, 97–111. https://doi.org/10.1016/j.lithos.2019.04.003

896 Esteves, A.F., 2006. As rochas metamórficas da região de Viseu. University of Aveiro.

897 Farina, F., Stevens, G., 2011. Lithos Source controlled 87 Sr / 86 Sr isotope variability
898 in granitic magmas : The inevitable consequence of mineral-scale isotopic
899 disequilibrium in the protolith. LITHOS 122, 189–200.
900 https://doi.org/10.1016/j.lithos.2011.01.001

901 Ferreira, J.A., Bento dos Santos, T., Pereira, I., Mata, J., 2019. Tectonically assisted
902 exhumation and cooling of Variscan granites in an anatectic complex of the
903 Central Iberian Zone , Portugal : constraints from LA - ICP - MS zircon and apatite
904 U – Pb ages. Int. J. Earth Sci. https://doi.org/10.1007/s00531-019-01755-1

905 Ferreira, J.A., Ribeiro, M.A., Martins, H.C.B., 2014. The Pedregal granite (Portugal):
906 petrographic and geochemical characterization of a peculiar granitoid. Estud.
907 Geológicos 70, e019. https://doi.org/10.3989/egeol.41730.321

908 Frost, B.R., Calvin, G.B., William, J.C., Arculus, R.J., Ellis, D.J., Frost, C.D., 2001. A
909 Geochemical Classification for Granitic Rocks. J. Petrol. 42, 2033–2048.

910 Gao, L.E., Zeng, L., Asimow, P.D., 2017. Contrasting geochemical signatures of fluid-
911 absent versus fluid-fluxed melting of muscovite in metasedimentary sources: The
912 Himalayan leucogranites. Geology 45. https://doi.org/10.1130/G38336.1

913 Griffin, W.L., Wang, X., Jackson, S.E., Pearson, N.J., O'Reilly, S.Y., Xu, X., Zhou, X.,
914 2002. Zircon chemistry and magma mixing, SE China: In-situ analysis of Hf
915 isotopes, Tonglu and Pingtan igneous complexes. Lithos 61, 237–269.
916 https://doi.org/https://doi.org/10.1016/S0024-4937(02)00082-8

917 Hart, S.R., Blusztajn, J., Dick, H.J.B., Meyer, P.S., Muehlenbachs, K., 1999. The
918 fingerprint of seawater circulation in a 500-meter section of ocean crust gabbros.
919 Geochim. Cosmochim. Acta 63, 4059–4080. https://doi.org/10.1016/S0016-
920 7037(99)00309-9.

921 Henrichs, I.A., O'Sullivan, G., Chew, D.M., Mark, C., Babechuk, M.G., McKenna, C.,
922 Emo, R., 2018. The trace element and U-Pb systematics of metamorphic apatite.
923 Chem. Geol. 483, 218–238. https://doi.org/10.1016/j.chemgeo.2017.12.031

924 Iglesias, M., Ribeiro, A., 1981. La zone de cisaillement ductile de Juzbado
925 (Salamanca)-Penalva Do Castelo (Viseu): un linéament ancien réactivé pendant
926 l'orogénese hercynienne? Comun. dos Serviços Geológicos Port. 67(1), 89–93.

927 Inger, S., Harris, N., 1993. Geochemical Constraints on Leukogranite Magmatism in
928 the Langtang Valley, Nepal Himalaya. J. Petrol. 34, 345–368.
929 https://doi.org/10.1093/petrology/34.2.345

930 Jacobsen, S.B., Wasserburg, G.J., 1980. Sm-Nd isotopic evolution of chondrites. Earth
931 Planet. Sci. Lett. 50, 139–155. https://doi.org/https://doi.org/10.1016/0012-
932 821X(80)90125-9

933 Johannes, W., Ehlers, C., Kriegsman, L.M., Mengel, K., 2003. The link between
934 migmatites and S-type granites in the Turku area , southern Finland. Lithos 68,
935 69–90. https://doi.org/10.1016/S0024-4937(03)00032-X

936 Jung, S., 2005. Isotopic equilibrium/disequilibrium in granites, metasedimentary rocks
937 and migmatites (Damara orogen, Namibia) - A consequence of

polymetamorphism and melting. Lithos 84, 168–184. https://doi.org/10.1016/j.lithos.2005.03.013

Jung, S., Pfänder, J.A., 2007. Source composition and melting temperatures of orogenic granitoids: constraints from CaO/Na2O, Al2O3/TiO2 and accessory mineral saturation thermometry. Eur. J. Mineral. 19, 859–870. https://doi.org/10.1127/0935-1221/2007/0019-1774

Liew, T., Hofmann, A., 1988. Precambrian crustal components, plutonic associations, plate environment of the Hercynian Fold Belt of central Europe: Indications from a Nd and Sr isotopic study. Contrib. to Mineral. Petrol. 98, 129–138. https://doi.org/10.1007/BF00402106

Lugmair, G.W., Marti, K., 1978. Lunar initial 143Nd/144Nd: Differential evolution of the lunar crust and mantle. Earth Planet. Sci. Lett. 39, 349–357. https://doi.org/https://doi.org/10.1016/0012-821X(78)90021-3

Martínez Catalán, J.R., Rubio Pascual, F.J., Montes, A.D., Fernández, R.D., Barreiro, J.G., Dias Da Silva, Í., Clavijo, E.G., Ayarza, P., Alcock, J.E., 2014. The late Variscan HT/LP metamorphic event in NW and Central Iberia: relationships to crustal thickening, extension, orocline development and crustal evolution. Geol. Soc. London, Spec. Publ. 405, 225–247. https://doi.org/10.1144/SP405.1

Martini, A., Fátima, M. De, Weinberg, R.F., Betino, G., Toni, D., Nardi, L.V.S., 2019. From migmatite to magma - crustal melting and generation of granite in the Camboriú Complex , south Brazil. Lithos 340–341, 270–286. https://doi.org/10.1016/j.lithos.2019.05.017

Miller, C.F., McDowell, S.M., Mapes, R.W., 2003. Hot and cold granites: Implications of zircon saturation temperatures and preservation of inheritance. Geology 31, 529–532. https://doi.org/10.1130/0091-7613(2003)031<0529:HACGIO>2.0.CO;2

963 Milord, I., Sawyer, E.W., Brown, M., 2001. Formation of diatexite migmatite and granite
964 magma during anatexis of semi-pelitic metasedimentary rocks: An example from
965 St. Malo, France. J. Petrol. 42, 487–505.
966 https://doi.org/10.1093/petrology/42.3.487

967 Montero, P., Talavera, C., Bea, F., 2017. Geochemical, isotopic, and zircon (U-Pb, O,
968 Hf isotopes) evidence for the magmatic sources of the volcano-plutonic Ollo de
969 Sapo Formation, Central Iberia. Geol. Acta 15, 245–260.
970 https://doi.org/10.1344/GeologicaActa2017.15.4.1

971 Morfin, S., Sawyer, E.W., Bandyayera, D., 2014. The geochemical signature of a felsic
972 injection complex in the continental crust: Opinaca Subprovince, Quebec. Lithos
973 196–197, 339–355. https://doi.org/10.1016/j.lithos.2014.03.004

974 Nance, R.D., Gutiérrez-Alonso, G., Keppie, J.D., Linnemann, U., Murphy, J.B.,
975 Quesada, C., Strachan, R.A., Woodcock, N.H., 2010. Evolution of the Rheic
976 Ocean. Gondwana Res. 17, 194–222. https://doi.org/10.1016/j.gr.2009.08.001

977 Palme, H., O'Neil, H.S.C., 2003. Cosmochemical estimatess of mantle composition.
978 mantle core 2, 1–38. https://doi.org/10.1016/B978-0-08-095975-7.00201-1

979 Patiño Douce, A.E., Harris, N., 1998. Experimental Constraints on Himalayan Anatexis.
980 J. Petrol. 39, 689–710. https://doi.org/10.1093/petroj/39.4.689

981 Pereira, I., Dias, R., Bento dos Santos, T., Mata, J., 2017. Exhumation of a migmatite
982 complex along a transpressive shear zone: Inferences from the Variscan Juzbado-
983 Penalva do Castelo Shear Zone (Central Iberian Zone). J. Geol. Soc. London.
984 174, 1004–1018. https://doi.org/10.1144/jgs2016-159

985 Perini, G., Cesare, B., Gömez-Pugnaire, M.T., Ghezzi, L., Tommasini, S., 2009.
986 Armouring effect on Sr-Nd isotopes during disequilibrium crustal melting: the case
987 study of frozen migmatites from El Hoyazo and Mazarrón, SE Spain. Eur. J.

988 Mineral. 21, 117–131. https://doi.org/10.1127/0935-1221/2009/0021-1882

989 Ribeiro, M.A., Sant'Ovaia, H., Dória, A., 2011. Litologias gnaisso-migmatíticas da faixa
990 Lavadores-Madalena: possível significado das paragéneses com hercinite.
991 Simpósio Model. Sist. Geológicos 343–351.

992 Ribeiro, M.L., 1978. Algumas observações sobre o metamorfismo na região de Tourém
993 (N de Portugal). Serviços Geológicos Port. 151–169.

994 Rosenberg, C.L., Handy, M.R., 2005. Experimental deformation of partially melted
995 granite revisited: implications for the continental crust. J. Metamorph. Geol. 23,
996 19–28. https://doi.org/10.1111/j.1525-1314.2005.00555.x

997 Sawyer, E.W., 2008. Atlas of Migmatites. NRC Research Press and Mineralogical
998 Association of Canada. https://doi.org/doi:10.1139/9780660197876

999 Sawyer, E.W., 1987. The role of partial melting and fractinal crystallization determining
1000 discordant migmatites leucosome compositions. J. Petrol. 28, 445–473.

1001 Sawyer, E.W., Cesare, B., Brown, M., 2011. When the continental crust melts.
1002 Elements 7, 229–234. https://doi.org/10.2113/gselements.7.4.229

1003 Schulmann, K., Schaltegger, U., Jezek, J., Thompson, A.B., Edel, J.B., 2002. Rapid
1004 burial and exhumation during orogeny: Thickening and synconvergent exhumation
1005 of thermally weakened and thinned crust (Variscan Orogen in Western Europe).
1006 Am. J. Sci. 302, 856–879. https://doi.org/10.2475/ajs.302.10.856

1007 Silva, A., Ribeiro, M.L., 2000. Carta Geológica Simplificada do Parque Arqueológico do
1008 Vale do Côa. Vila Nova de Foz Côa.

1009 Söderlund, U., Patchett, P.J., Vervoort, J., Isachsen, C., 2004. The 176Lu decay
1010 constant determined by Lu-Hf and U-Pb isotope systematics of Precambrian mafic
1011 intrusions. Earth Planet. Sci. Lett. 219, 311–324. https://doi.org/10.1016/S0012-
1012 821X(04)00012-3

1013 Sola, A.M., Becchio, R.A., Pimentel, M.M., 2013. Petrogenesis of migmatites and
1014 leucogranites from Sierra de Molinos , Salta , Northwest Argentina : A petrologic
1015 and geochemical study Lithos Petrogenesis of migmatites and leucogranites from
1016 Sierra de Molinos , Salta , Northwest Argentina : A petrologic . LITHOS 177, 470–
1017 491. https://doi.org/10.1016/j.lithos.2013.07.025

1018 Spear, F.S., Kohn, M.J., Cheney, J.T., 1999. P - T paths from anatectic pelites.
1019 Contrib. to Mineral. Petrol. 134, 17–32. https://doi.org/10.1007/s004100050466

1020 Steiger, R.H., Jäger, E., 1977. Subcommission on geochronology: Convention on the
1021 use of decay constants in geo- and cosmochronology. Earth Planet. Sci. Lett. 36,
1022 359–362. https://doi.org/https://doi.org/10.1016/0012-821X(77)90060-7

1023 Tang, M., Wang, X., Shu, X., Wang, D., Yang, T., Gopon, P., 2014. Hafnium isotopic
1024 heterogeneity in zircons from granitic rocks : Geochemical evaluation and
1025 modeling of " zircon effect " in crustal anatexis. Earth Planet. Sci. Lett. 389, 188–
1026 199. https://doi.org/10.1016/j.epsl.2013.12.036

1027 Tassinari, C.C.G., Medina, J., Pinto, M.S., 1996. Rb-Sr and Sm-Nd geochronology and
1028 isotope geochemistry of central Iberian metasedimentary rocks (Portugal). Geol.
1029 en Mijnb. 75, 69–79.

1030 Teixeira, R.J.S., 2008. Mineralogia, petrologia e geoquímica dos granitos e seus
1031 encraves da região de Carrazeda de Ansiães. Universidade de Trás-os-Montes e
1032 Alto Douro.

1033 Tommasini, S., Davies, G.R., 1997. Isotope disequilibrium during anatexis: a case
1034 study of contact melting, Sierra Nevada, California. Earth Planet. Sci. Lett. 148,
1035 273–285.

1036 Trail, D., Watson, E., Tailby, N., 2012. Ce and Eu anomalies in zircon as proxies for
1037 oxidation state of magmas. Geochim. Cosmochim. Acta 97, 70–87.

https://doi.org/10.1016/j.gca.2012.08.032

Tuttle, O.F., Bowen, N.L., 1958. Origin of granite in the light of experimental studies in the system NaAlSi3O8-KAlSi3O8-SiO2-H2O, Geological Society of America Memoir.

Vanderhaeghe, O., 2009. Migmatites, granites and orogeny: Flow modes of partially-molten rocks and magmas associated with melt/solid segregation in orogenic belts. Tectonophysics 477, 119–134. https://doi.org/10.1016/j.tecto.2009.06.021

Vernon, R.H., Clarke, G.L., 2008. Principles of metamorphic petrology. Cambridge University Press.

Vervoort, J.D., Blichert-Toft, J., 1999. Evolution of the depleted mantle: Hafnium isotope evidence from juvenile rocks through time. \gca 63, 533–556. https://doi.org/10.1016/S0016-7037(98)00274-9

Vielzeuf, D., Holloway, J., 1988. Experimental determination of the fluid-absent melting relations in the pelitic system. Contrib. to Mineral. Petrol. 98, 257–276. https://doi.org/10.1007/BF00375178

Villar Alonso, P., Fernández Ruiz, J., Bellido, F., Carrasco, R.., Rodriguez Fernández, L.., 2000. Memoria del mapa geológico de España 1:50000, Lumbrales (Hoja 475). Série magna, 1ªed, 2ªsérie,. Madrid.

Villaros, A., Stevens, G., Moyen, J.F., Buick, I.S., 2009. The trace element compositions of S-type granites: Evidence for disequilibrium melting and accessory phase entrainment in the source. Contrib. to Mineral. Petrol. 158, 543–561. https://doi.org/10.1007/s00410-009-0396-3

Villaseca, C., Barbero, L., Herreros, V., 1998. A re-examination of the typology of peraluminous granite types in intracontinental orogenic belts. Trans. R. Soc. Edinb. Earth Sci. 89, 113–119. https://doi.org/DOI: 10.1017/S0263593300007045

1063 Villaseca, C., Merino, E., Oyarzun, R., Orejana, D., Pérez-Soba, C., Chicharro, E.,
1064 2014. Contrasting chemical and isotopic signatures from Neoproterozoic
1065 metasedimentary rocks in the Central Iberian Zone (Spain) of pre-Variscan
1066 Europe: Implications for terrane analysis and Early Ordovician magmatic belts.
1067 Precambrian Res. 245, 131–145. https://doi.org/10.1016/j.precamres.2014.02.006

1068 Wang, X., Griffin, W.L., Chen, J., 2010. Hf contents and Zr/Hf ratios in granitic zircons.
1069 Geochem. J. 44, 65–72. https://doi.org/10.2343/geochemj.1.0043

1070 Watson, E.B., Harrison, T.M., 1983. Zircon saturation revisited: temperature and
1071 composition effects in a variety of crustal magma types. Earth Planet. Sci. Lett. 64,
1072 295–304. https://doi.org/10.1016/0012-821X(83)90211-X

1073 Weinberg, R.F., Hasalová, P., 2015. Water-fluxed melting of the continental crust: A
1074 review. Lithos. https://doi.org/10.1016/j.lithos.2014.08.021

1075 White, W., 2010. Oceanic Island Basalts and Mantle Plumes: The Geochemical
1076 Perspective. Annu. Rev. Earth Planet. Sci 38, 133–160.
1077 https://doi.org/10.1146/annurev-earth-040809-152450

1078 Whitney, D.L., Teyssier, C., Vanderhaeghe, O., 2004. Gneiss domes and crustal flow.
1079 Spec. Pap. 380 Gneiss Domes Orogeny 15–33. https://doi.org/10.1130/0-8137-
1080 2380-9.15

1081 Winter, J.D., 2014. Principles of Igneous and Metamorphic Petrology John D. Winter
1082 Second Edition.

1083 Wolf, M., Romer, R.L., Glodny, J., 2019. Isotope disequilibrium during partial melting of
1084 metasedimentary rocks. Geochim. Cosmochim. Acta 257, 163–183.
1085 https://doi.org/10.1016/j.gca.2019.05.008

1086 Yakymchuk, C., 2019. On Granites. J. Geol. Soc. India 94, 9–22.
1087 https://doi.org/10.1007/s12594-019-1261-2

1088 Yakymchuk, C., Acosta-Vigil, A., 2019. Geochemistry of phosphorus and the behavior
1089 of apatite during crustal anatexis: Insights from melt inclusions and
1090 nanogranitoids. Am. Mineral. 104, 1765–1780. https://doi.org/10.2138/am-2019-
1091 7054

1092 Yakymchuk, C., Brown, C.R., Brown, M., Siddoway, C.S., Fanning, C.M., Korhonen,
1093 F.J., 2015. Paleozoic evolution of western Marie Byrd Land, Antarctica. Bull. Geol.
1094 Soc. Am. 127, 1464–1484. https://doi.org/10.1130/B31136.1

1095 Yakymchuk, C., Brown, M., 2014. Consequences of open-system melting in tectonics.
1096 J. Geol. Soc. London. 171, 21–40. https://doi.org/10.1144/jgs2013-039

1097 Yakymchuk, C., Clark, C., White, R.W., 2017. Phase Relations, Reaction Sequences
1098 and Petrochronology. Rev. Mineral. Geochemistry 83, 13–53.
1099 https://doi.org/10.2138/rmg.2017.83.2

1100 Yakymchuk, C., Siddoway, C.S., Fanning, C.M., Mcfadden, R., Korhonen, F.J., Brown,
1101 M., 2013. Anatectic reworking and differentiation of continental crust along the
1102 active margin of Gondwana: A zircon Hf-O perspective from West Antarctica.
1103 Geol. Soc. Spec. Publ. 383, 169–210. https://doi.org/10.1144/SP383.7

1104 Yang, L., Liu, X.-C., Wang, J.-M., Wu, F.-Y., 2019. Is Himalayan leucogranite a product
1105 by in situ partial melting of the Greater Himalayan Crystalline? A comparative
1106 study of leucosome and leucogranite from Nyalam, southern Tibet. Lithos 342–
1107 343, 542–556.

1108 Zartman, R.E., Doe, B.R., 1981. Plumbotectonics - the model. Tectonophysics 75,
1109 135–162.

1110 Zeng, L., Asimow, P.D., Saleeby, J.B., 2005a. Coupling of anatectic reactions and
1111 dissolution of accessory phases and the Sr and Nd isotope systematics of
1112 anatectic melts from a metasedimentary source. Geochim. Cosmochim. Acta 69,

3671–3682. https://doi.org/10.1016/J.GCA.2005.02.035

Zeng, L., Saleeby, Æ.J.B., Ducea, Æ.M., 2005b. Geochemical characteristics of crustal anatexis during the formation of migmatite at the Southern Sierra Nevada , California. https://doi.org/10.1007/s00410-005-0010-2

Figure Captions

Fig.1 – (a) Figueira de Castelo Rodrigo-Lumbrales Anatectic Complex in the Iberian Variscan Belt setting (adapted from Dias et al., 2016); (b) Geological map of the Figueira de Castelo Rodrigo-Lumbrales Anatectic Complex (modified from Silva and Ribeiro, 2000).

Fig. 2 – Field observations: (a) phyllites with andalusite porphyroblasts; (b) metatexite with bands of peritectic sillimanite; (c) metatexite with boudinated leucosome veins; (d) leucosome pocket associated to metatexite; (e) restitic nodule in diatexite; (f) schlieren structures in diatexite; (g) nebulitic texture in diatexite; (h) and (i) two-mica granites with variable grain size.

Fig. 3 – Petrographic observations: (a) phyllite with foliated texture; (b) pseudomorph of andalusite in the phyllite; (c) alternation of leucosome and melanosome in the metatexite; (d) fibrolite included in the retrograde secondary muscovite in metatexite; (e) Corroded biotite and melt films evidences (red arrows) in diatexite; (f) secondary muscovite including fibrolite in diatexite; (g) granite texture and typical mineralogy; (h) granite with evidences of deformation.

Fig. 4 – Harker diagrams for major elements for the host rocks (phyllites and quartzphyllites) and FCR-LAC lithologies (metatexites, diatexites and granites).

Fig. 5 – Harker diagrams for trace elements for the host rocks (phyllites and quartzphyllites) and FCR-LAC lithologies (metatexites, diatexites and granites).

1137 Fig. 6 – (a) Multi-element diagram for phyllites, quartzphyllites and metatexites; (b)
1138 Multi-element diagram for type-1 diatexites, type-2 diatexites and granites. Chondrite
1139 normalization values after Palme and O'Neil (2003).

1140 Fig. 7 – (a) REE diagram for phyllites, quartzphyllites and metatexites; (b) REE
1141 diagram for type-1 diatexites and type-2 diatexites; (c) REE diagram for granites.
1142 Chondrite normalization values after Palme and O'Neil (2003).

1143 Fig. 8 – (a), (b), (c), (d) and (e) Sr, Y, Th, U and REE (ppm) *versus* SiO2 WR (Whole-
1144 Rock; wt. %), respectively; (f) Apatite REE pattern for phyllites, quartzphyllites,
1145 metatexites, type-1 diatexites, type-2 diatexites and granites; (g) Zircon REE pattern for
1146 metatexites, type-1 diatexites, type-2 diatexites and granites. Chondrite normalization
1147 values after Palme and O'Neil (2003).

1148 Fig. 9 – (a) $^{87}Sr/^{86}Sr_{320}$ *versus* εNd_{320} diagram for the host rocks (phyllites) and FCR-
1149 LAC lithologies (metatexites, diatexites and granites); (b) $^{87}Sr/^{86}Sr_{320}$ *versus* εNd_{320}
1150 diagram for the host rocks (phyllites), FCR-LAC lithologies (metatexites, diatexites and
1151 granites) and comparison with other geological domains of the CIZ: Douro-Beiras
1152 Supergroup (Douro Group – Teixeira, 2008; Beiras Group – Tassinari et al., 1996;
1153 South CIZ – Villaseca et al., 2014), Aguiar da Beira granitoids (biotite granodiorite-
1154 granite and muscovite-biotite leucogranite; Costa et al., 2014), and Ollo de Sapo
1155 gneisses (Montero et al., 2017). The Aguiar da Beira granitoids were chosen because
1156 of its proximity to the FCR-LAC and their syn-tectonic character; (c) εNd_{320} *versus*
1157 εHf_{320} diagram for the host rocks (phyllites) and FCR-LAC lithologies (metatexites,
1158 diatexites and granites). The green and the purple ellipses correspond to groups
1159 defined by very close εNd_{320} *vs.* εHf_{320} compositions.

1160 Fig.10 – (a) $^{206}Pb/^{204}Pb_{320}$ *versus* $^{207}Pb/^{204}Pb_{320}$ for the host rocks (phyllites) and FCR-
1161 LAC lithologies (metatexites, diatexites and granites); (b) $^{206}Pb/^{204}Pb_{320}$ *versus*

1162 $^{208}Pb/^{204}Pb_{320}$ for the host rocks (phyllites) and FCR-LAC lithologies (metatexites,
1163 diatexites and granites).

1164 Fig. 11 – (a) Aluminium Saturation Index (ASI) classification for granitic and diatexitic
1165 rocks proposed by (Frost et al., 2001); (b) A-B granite classification diagram of
1166 Villaseca et al. (1998); (c) Ab-Or-Q ternary diagram (Tuttle and Bowen, 1958; Winter,
1167 2014) for the FCR-LAC granites; (d) Na_2O+K_2O-CaO (wt. %) versus SiO_2 (wt. %)
1168 classification diagram (Frost et al., 2001) showing the ranges between alkalic and
1169 calcic composition for the FCR-LAC diatexites and granites.

1170 Fig. 12 – (a) CaO/Na_2O *versus* Al_2O_3/TiO_2 (wt. %) distinguish between pelite-derived
1171 melts ($CaO/Na_2O < 0.3$) and melts derived from greywackes or igneous sources (Jung
1172 and Pfänder, 2007) for FCR-LAC granites and diatexites; (b) Rb/Sr *versus* Sr (ppm)
1173 and (c) Rb/Sr *versus* Ba (ppm) for the host rocks (phyllites) and FCR-LAC lithologies
1174 (metatexites, diatexites and granites). The vectors represent the evolution of partial
1175 melting reactions (Inger and Harris, 1993): Mu(VP) – vapour-present muscovite
1176 melting; Mu(VA) – vapour-absent muscovite melting; Bi(VA) – vapour-absent biotite
1177 melting; (d) Cao (wt. %) *versus* Eu/Eu* for the host rocks (phyllites) and FCR-LAC
1178 lithologies (metatexites, diatexites and granites).

1179 Fig. 13 – Apatite and zircon role during the partial melting process in the FCR-LAC: (a)
1180 P_2O_5 *versus* LREE (ppm); (b) Zr *versus* Hf (ppm); (c) Zr *versus* HREE (ppm); (d) Hf
1181 *versus* HREE (ppm).

1182 Fig. 14 – (a) εNd_0 *versus* εHf_0 diagram for the host rocks (phyllites) and FCR-LAC
1183 lithologies (metatexites, diatexites and granites); (b) $^{87}Sr/^{86}Sr_0$ *versus* εNd_0 diagram for
1184 the host rocks (phyllites) and FCR-LAC lithologies (metatexites, diatexites and
1185 granites); (b) and (c) Plumbotectonic model after Zartman and Doe (1981) applied to
1186 the host rocks (phyllites) and FCR-LAC lithologies (metatexites, diatexites and
1187 granites): A – mantle; B – orogene; C – upper crust; D – lower crust.

1188 Fig. 15 – Covariation between LILE (K, Sr and Ba) and HFSE (TiO_2), (a), (b) and (c),
1189 respectively; (d) AFC assessment – La/Sm *versus* Th/Sc (ppm).

1190

1191 Table 1 – Modal mineralogical proportion for the host rocks (phyllites and
1192 quartzphyllites) and rocks from the Figueira de Castelo Rodrigo-Lumbrales Anatectic
1193 Complex (metatexites, diatexites and granites).

1194 Table 2 – Whole-rock chemical composition of phyllites, quartzphyllites (qtzphyllites)
1195 and FCR-LAC rocks (metatexites, diatexites, and granites). Major elements in weight
1196 percentage (wt. %) and the trace elements expressed in parts per million (ppm).

1197 Table 3 – Apatite trace element composition (ppm) from the host rocks (phyllites) and
1198 FCR-LAC rocks (metatexites, diatexites, and granites).

1199 Table 4 – Zircon trace element composition (ppm) from FCR-LAC rocks (metatexites,
1200 diatexites, and granites).

1201 Table 5 – Whole-rock Sr, Nd, Hf and Pb isotopic data for the host rocks (phyllites) and
1202 FCR-LAC rocks (metatexites, diatexites, and granites).

Table 1

	Phyllites	Quartzphyllites	Metatexites	Type-1 Diatexites	Type-2 Diatexites	Granites
Quartz	36	48	32	32	40	33
Plagioclase	10	-	14	22	28	23
K-feldspar	-	-	7	12	14	17
Biotite	30	30	22	9	8	12
Muscovite	19	19	21	20	9	12
Sillimanite	-	-	3	4	<1	3
Chlorite	4	2	-	-	-	-
Accessory minerals	<1	<1	<1	<1	<1	<1

Table 2

Lithology	Phyllite N		Phyllite S		Qtzphyllite N	Qtzphyllite S	Metatexite										
Sample	JTJ-2	JTJ-6	JTJ-18	JTJ-19	JTJ-49	JTJ-41b	JTJ-8	JTJ-20	JTJ-22B	JTJ-24B	JTJ-25	JTJ-37	JTJ-48B	JTJ-53	JTJ-54B	JTJ-56A	JTJ-60A
SiO_2	61.02	54.64	63.82	66.63	68.39	65.71	58.57	66.85	63.74	74.73	60.94	69.23	59.31	64.82	58.51	69.93	71.14
Al_2O_3	18.02	23.40	17.68	14.94	14.18	16.15	20.42	16.58	17.78	12.47	18.57	15.08	18.69	15.58	20.42	14.10	15.38
$Fe_2O_3^T$	6.95	7.34	4.91	5.36	4.55	6.24	8.10	5.51	5.61	3.78	6.52	4.76	7.32	5.90	6.79	4.47	2.50
FeO^T	6.25	6.60	4.42	4.82	4.09	5.61	7.29	4.96	5.05	3.40	5.87	4.28	6.59	5.31	6.11	4.02	2.25
MnO	0.06	0.07	0.05	0.04	0.06	0.08	0.09	0.06	0.05	0.12	0.04	0.07	0.10	0.10	0.09	0.09	0.08
MgO	2.40	2.06	1.75	1.67	1.65	2.00	2.43	1.74	2.01	1.25	2.24	1.84	2.70	2.16	2.73	1.69	0.73
CaO	1.36	0.30	0.10	0.15	2.36	0.44	0.55	0.79	0.35	0.76	0.51	1.13	0.54	0.23	0.69	0.74	0.60
Na_2O	1.75	1.14	1.18	1.35	2.52	1.75	1.57	2.30	1.18	2.18	1.40	2.65	1.21	1.45	1.82	2.80	3.04
K_2O	3.40	4.49	4.34	2.86	3.68	3.03	3.92	3.48	3.84	3.41	4.16	3.27	4.42	2.84	3.67	3.41	4.34
TiO_2	0.87	0.82	0.76	0.86	0.76	0.89	0.84	0.86	0.70	0.58	0.78	0.64	0.82	0.70	0.74	0.60	0.32
P_2O_5	0.14	0.13	0.11	0.07	0.15	0.15	0.13	0.11	0.14	0.17	0.17	0.19	0.15	0.14	0.17	0.16	0.24
LOI	3.65	5.09	4.22	5.02	1.01	3.60	3.72	2.25	3.69	1.23	4.51	1.53	4.43	4.72	4.75	1.63	1.37
Total	99.62	99.45	98.92	98.95	99.31	100.00	100.30	100.50	99.08	100.70	99.84	100.40	99.68	98.63	100.40	99.62	99.74
Sc	15.00	18.00	15.00	14.00	11.00	15.00	18.00	15.00	15.00	8.00	16.00	12.00	17.00	15.00	17.00	13.00	7.00
V	91.00	115.00	123.00	94.00	67.00	98.00	112.00	92.00	111.00	59.00	111.00	79.00	109.00	136.00	124.00	72.00	36.00
Ba	737.00	780.00	764.00	608.00	660.00	608.00	735.00	497.00	615.00	683.00	921.00	664.00	738.00	1038.00	1005.00	361.00	286.00
Sr	209.00	110.00	64.00	49.00	243.00	82.00	118.00	149.00	79.00	156.00	114.00	189.00	111.00	74.00	169.00	107.00	79.00
Y	32.00	29.00	28.00	34.00	28.00	33.00	29.00	22.00	24.00	21.00	26.00	29.00	28.00	33.00	29.00	26.00	14.00
Zr	203.00	133.00	211.00	218.00	386.00	285.00	142.00	188.00	162.00	274.00	142.00	200.00	140.00	155.00	140.00	240.00	114.00
Cr	90.00	110.00	90.00	80.00	60.00	90.00	100.00	80.00	80.00	50.00	90.00	70.00	100.00	100.00	90.00	70.00	40.00
Ni	40.00	40.00	20.00	30.00	20.00	20.00	50.00	30.00	20.00	< 20	30.00	< 20	40.00	50.00	30.00	30.00	< 20
Ga	25.00	32.00	23.00	20.00	19.00	21.00	29.00	22.00	23.00	16.00	25.00	19.00	26.00	23.00	28.00	21.00	22.00
Rb	154.00	184.00	174.00	116.00	154.00	110.00	189.00	167.00	180.00	186.00	170.00	150.00	234.00	170.00	281.00	279.00	260.00
Nb	15.00	14.00	11.00	12.00	13.00	12.00	15.00	13.00	11.00	8.00	12.00	10.00	14.00	11.00	12.00	16.00	19.00
Cs	4.90	9.90	7.60	4.80	8.80	2.10	16.30	12.60	33.30	20.60	9.30	9.40	28.50	13.30	44.10	58.40	42.00
La	51.00	53.90	42.80	46.40	50.90	38.60	61.10	34.70	34.50	43.60	46.40	38.20	45.90	44.70	46.90	40.80	17.70
Ce	92.40	104.00	83.00	93.20	103.00	77.60	114.00	73.00	69.20	91.10	92.10	78.50	90.60	88.30	92.80	82.70	35.00
Pr	11.30	11.90	10.30	10.70	11.40	9.28	13.20	8.22	8.26	9.82	10.90	8.68	10.00	10.30	10.40	9.44	4.03
Nd	40.10	43.30	37.90	40.80	41.60	34.30	46.60	31.00	30.00	35.50	40.90	31.60	37.50	38.40	38.40	34.00	14.00
Sm	7.60	8.40	7.30	8.10	7.60	7.10	8.50	6.20	6.10	6.60	7.90	6.40	7.00	7.40	7.40	6.80	2.90
Eu	1.55	1.69	1.41	1.65	1.67	1.42	1.67	1.23	1.22	1.10	1.50	1.36	1.39	1.47	1.53	1.10	0.54
Gd	6.30	6.80	6.00	7.40	6.30	6.70	6.60	5.20	5.40	5.50	6.60	5.60	6.10	6.80	6.10	5.50	2.50
Tb	1.00	1.00	0.90	1.20	1.00	1.10	1.00	0.80	0.90	0.80	1.00	0.90	1.00	1.00	1.00	0.90	0.50
Dy	6.00	5.90	5.50	6.90	5.70	6.30	6.00	4.50	5.00	4.50	5.60	5.60	5.40	6.00	5.70	5.00	2.70
Ho	1.10	1.10	1.10	1.30	1.10	1.20	1.10	0.80	0.90	0.80	1.00	1.10	1.00	1.20	1.10	1.00	0.50
Er	3.30	3.20	3.10	3.70	3.10	3.70	3.10	2.50	2.80	2.30	2.90	3.40	3.00	3.40	3.10	2.80	1.40
Tm	0.47	0.48	0.46	0.54	0.45	0.53	0.46	0.37	0.41	0.33	0.40	0.51	0.43	0.49	0.43	0.41	0.21
Yb	3.10	3.20	3.10	3.50	3.10	3.50	2.90	2.60	2.90	2.20	2.70	3.40	2.90	3.20	2.90	2.80	1.40
Lu	0.46	0.47	0.46	0.51	0.47	0.55	0.45	0.40	0.45	0.34	0.42	0.53	0.43	0.51	0.44	0.43	0.22
Hf	5.40	3.60	5.20	5.50	9.30	7.00	3.70	4.80	4.20	6.00	3.50	5.00	3.80	3.80	3.80	6.10	2.80
Ta	1.30	1.20	1.10	1.30	1.20	1.00	1.20	1.50	2.10	1.00	0.90	1.10	1.40	0.90	1.00	2.40	4.90
Pb	23.00	21.00	10.00	11.00	22.00	15.00	25.00	20.00	17.00	28.00	21.00	29.00	22.00	22.00	25.00	17.00	21.00
Th	17.10	16.90	12.00	10.20	16.70	13.40	17.20	10.80	10.50	15.30	12.70	11.90	13.20	12.20	13.20	12.80	5.50
U	3.50	6.50	3.60	3.80	3.20	3.80	4.20	5.10	6.60	3.50	4.50	3.90	6.40	43.70	9.40	7.10	3.80
REE	225.68	245.34	203.33	225.90	237.39	191.88	266.68	171.52	168.04	204.49	220.32	185.78	212.65	213.17	218.20	193.68	83.60

LREE	202.40	221.50	181.30	199.20	214.50	166.88	243.40	153.12	148.06	186.62	198.20	163.38	191.00	189.10	195.90	173.74	73.63
HREE	23.28	23.84	22.03	26.70	22.89	25.00	23.28	18.40	19.98	17.87	22.12	22.40	21.65	24.07	22.30	19.94	9.97
LREE/HREE	8.69	9.29	8.23	7.46	9.37	6.68	10.46	8.32	7.41	10.44	8.96	7.29	8.82	7.86	8.78	8.71	7.39
La/Yb_N	11.08	11.34	9.30	8.93	11.06	7.43	14.19	8.99	8.01	13.35	11.57	7.57	10.66	9.41	10.89	9.81	8.51
La/Sm_N	4.22	4.03	3.69	3.60	4.21	3.42	4.52	3.52	3.56	4.15	3.69	3.75	4.12	3.80	3.98	3.77	3.84
Dy/Yb_N	1.26	1.20	1.15	1.28	1.19	1.17	1.34	1.12	1.12	1.33	1.35	1.07	1.21	1.22	1.28	1.16	1.25
Tb/Yb_N	1.42	1.38	1.28	1.51	1.42	1.38	1.52	1.35	1.37	1.60	1.63	1.16	1.52	1.38	1.52	1.41	1.57
Eu/Eu*	0.68	0.68	0.65	0.65	0.74	0.63	0.68	0.66	0.65	0.56	0.63	0.69	0.65	0.63	0.70	0.55	0.61

Table 2 *continued*

Lithology	Type-1 Diatexite								Type-2 Diatexite							
Sample	JTJ-27	JTJ-30	JTJ-31C	JTJ-43	JTJ-48A	JTJ-52	JTJ-55	JPC-48	JTJ-23A	JTJ-24A	JTJ-26	JTJ-28A	JTJ-51	JTJ-56B	JTJ-60B	JPC-45
SiO2	72.92	72.29	74.46	68.32	72.75	72.33	73.30	69.83	73.53	74.24	74.82	75.14	75.24	74.98	72.95	74.55
Al2O3	13.92	14.17	14.07	15.60	15.37	14.94	14.72	15.62	14.35	13.93	13.27	14.96	12.87	12.91	15.25	14.11
$Fe2O3^T$	0.97	1.38	0.90	2.90	1.29	1.52	1.13	2.15	1.12	0.75	0.81	0.18	2.67	1.01	0.98	0.81
FeO^T	0.87	1.24	0.81	2.61	1.16	1.37	1.02	1.93	1.01	0.67	0.73	0.16	2.40	0.91	0.88	0.73
MnO	0.01	0.01	0.02	0.03	0.03	0.02	0.03	0.03	0.03	0.03	0.01	0.01	0.05	0.03	0.02	0.02
MgO	0.21	0.31	0.25	0.84	0.27	0.41	0.29	0.67	0.18	0.17	0.16	0.06	0.90	0.36	0.49	0.44
CaO	0.59	0.63	0.54	0.95	0.61	0.74	0.88	0.62	0.46	0.59	0.60	0.42	0.65	0.48	0.44	0.21
Na2O	3.07	3.12	3.13	2.80	3.39	2.98	3.56	2.91	3.57	3.66	3.15	2.57	2.31	3.16	3.89	2.96
K2O	5.31	5.64	5.50	5.71	4.82	5.44	4.18	5.93	4.28	4.97	4.50	6.16	3.77	4.55	3.91	5.27
TiO2	0.12	0.20	0.13	0.75	0.19	0.24	0.15	0.40	0.07	0.07	0.11	0.02	0.39	0.12	0.10	0.12
P2O5	0.36	0.47	0.30	0.44	0.42	0.39	0.25	0.40	0.24	0.25	0.18	0.34	0.14	0.17	0.24	0.20
LOI	1.10	0.93	0.83	1.41	1.05	1.15	1.21	1.23	1.35	0.72	0.98	0.81	1.47	1.50	1.20	1.19
Total	98.58	99.14	100.10	99.74	100.20	100.20	99.68	101.72	99.18	99.38	98.58	100.70	100.50	99.25	99.46	100.61
Sc	4.00	2.00	1.00	3.00	2.00	3.00	3.00	<7	4.00	3.00	5.00	< 1	8.00	3.00	3.00	<7
V	< 5	< 5	< 5	29.00	6.00	8.00	< 5	13.00	< 5	< 5	< 5	< 5	38.00	9.00	9.00	5.00
Ba	196.00	217.00	232.00	640.00	205.00	282.00	468.00	353.00	146.00	203.00	200.00	358.00	582.00	482.00	187.00	220.00
Sr	57.00	56.00	61.00	150.00	50.00	74.00	139.00	89.00	43.00	79.00	63.00	111.00	128.00	115.00	69.00	82.00
Y	12.00	11.00	4.00	11.00	8.00	12.00	9.00	14.00	9.00	8.00	12.00	4.00	24.00	9.00	7.00	10.00
Zr	47.00	79.00	45.00	415.00	74.00	100.00	48.00	163.00	28.00	42.00	35.00	25.00	159.00	42.00	39.00	37.00
Cr	< 20	< 20	< 20	< 20	< 20	< 20	< 20	19.00	< 20	< 20	< 20	< 20	40.00	< 20	< 20	6.00
Ni	< 20	< 20	< 20	< 20	< 20	< 20	< 20	7.00	< 20	< 20	< 20	< 20	< 20	< 20	< 20	<7
Ga	18.00	21.00	19.00	26.00	24.00	20.00	17.00	23.00	16.00	12.00	16.00	17.00	16.00	12.00	15.00	14.00
Rb	239.00	303.00	275.00	331.00	315.00	282.00	143.00	290.00	238.00	170.00	183.00	234.00	165.00	154.00	145.00	205.00
Nb	6.00	7.00	4.00	6.00	10.00	7.00	6.00	10.37	9.00	4.00	3.00	< 1	7.00	5.00	5.00	4.98
Cs	10.20	8.60	6.60	7.80	20.30	17.10	14.00	-	34.80	9.70	5.00	6.00	10.10	8.60	6.00	-
La	7.20	15.60	5.90	145.00	14.70	20.40	21.00	36.96	3.50	3.60	4.60	1.10	36.60	7.70	6.80	3.79
Ce	15.40	35.10	13.40	368.00	32.20	44.70	41.70	79.12	7.80	7.20	9.60	2.20	74.20	15.20	13.10	7.77
Pr	1.85	4.23	1.65	46.50	3.78	5.19	4.80	9.79	0.88	0.79	1.11	0.28	8.21	1.64	1.49	0.95
Nd	6.70	16.00	6.10	175.00	14.40	19.50	17.10	36.54	3.40	2.90	4.10	1.10	29.20	6.60	5.20	3.46
Sm	1.80	4.10	1.80	25.40	3.90	5.10	4.10	8.99	0.80	0.70	1.10	0.40	5.90	1.30	1.00	0.98
Eu	0.41	0.45	0.39	1.06	0.33	0.55	0.79	0.61	0.25	0.40	0.44	0.55	1.08	0.56	0.34	0.43
Gd	1.90	3.60	1.80	9.50	3.50	4.70	3.30	6.86	1.00	0.80	1.30	0.50	4.80	1.30	0.90	1.12
Tb	0.40	0.60	0.30	0.80	0.50	0.70	0.50	0.85	0.30	0.20	0.30	0.10	0.80	0.20	0.20	0.24
Dy	2.20	2.90	1.10	3.10	2.10	3.10	2.10	3.52	1.70	1.30	2.00	0.60	4.70	1.40	1.10	1.70

Ho	0.40	0.40	0.20	0.40	0.20	0.40	0.30	0.49	0.30	0.30	0.40	0.10	0.90	0.20	0.20	0.35
Er	1.10	0.70	0.30	0.90	0.50	0.80	0.60	1.10	0.90	0.80	1.20	0.30	2.50	0.70	0.70	1.07
Tm	0.14	0.08	0.05	0.12	0.06	0.11	0.08	0.15	0.14	0.14	0.20	0.05	0.37	0.10	0.11	0.18
Yb	0.90	0.40	0.20	0.70	0.40	0.60	0.50	1.00	1.00	1.10	1.40	0.30	2.30	0.80	0.90	1.27
Lu	0.12	0.01	0.01	0.09	0.05	0.10	0.06	0.14	0.15	0.17	0.22	0.04	0.36	0.13	0.13	0.20
Hf	1.40	2.10	1.30	10.00	2.10	2.80	1.50	2.32	0.80	1.20	0.90	0.90	4.10	1.00	1.30	<0.06
Ta	0.70	0.80	0.60	0.50	1.90	0.90	1.10	1.03	1.90	1.30	0.30	< 0.1	0.90	1.00	1.40	0.37
Pb	32.00	33.00	33.00	41.00	27.00	36.00	36.00	39.00	36.00	41.00	31.00	43.00	28.00	37.00	28.00	38.00
Th	2.50	7.50	2.90	133.00	6.90	8.10	6.90	20.62	0.90	0.90	1.30	< 0,1	12.30	2.30	1.80	1.54
U	5.50	9.30	6.10	10.30	10.00	7.80	5.90	13.48	6.80	12.80	3.30	1.50	5.40	3.00	7.10	3.38
REE	40.52	84.17	33.20	776.57	76.62	105.95	96.93	186.13	22.12	20.40	27.97	7.62	171.92	37.83	32.17	23.52
LREE	32.95	75.03	28.85	759.90	68.98	94.89	88.70	171.40	16.38	15.19	20.51	5.08	154.11	32.44	27.59	16.96
HREE	7.57	9.14	4.35	16.67	7.64	11.06	8.23	14.73	5.74	5.21	7.46	2.54	17.81	5.39	4.58	6.57
LREE/HREE	4.35	8.21	6.63	45.58	9.03	8.58	10.78	11.64	2.85	2.92	2.75	2.00	8.65	6.02	6.02	2.58
La/Yb_N	5.39	26.27	19.87	139.50	24.75	22.90	28.29	24.80	2.36	2.20	2.21	2.47	10.72	6.48	5.09	2.01
La/Sm_N	2.51	2.39	2.06	3.59	2.37	2.51	3.22	2.58	2.75	3.23	2.63	1.73	3.90	3.72	4.27	2.43
Dy/Yb_N	1.59	4.71	3.57	2.88	3.41	3.36	2.73	2.28	1.10	0.77	0.93	1.30	1.33	1.14	0.79	0.87
Tb/Yb_N	1.96	6.60	6.60	5.03	5.50	5.13	4.40	3.72	1.32	0.80	0.94	1.47	1.53	1.10	0.98	0.83
Eu/Eu*	0.68	0.36	0.66	0.21	0.27	0.34	0.66	0.24	0.85	1.63	1.12	3.76	0.62	1.32	1.10	1.26

Table 2 *continued*

Lithology	Granite															
Sample	JTJ-31A	JTJ-32	JTJ-34	JTJ-40	JPC-49	JPC-56	JPC-57	JTJ-9	JTJ-10	JTJ-44	JTJ-45	JTJ-47	JTJ-50	JTJ-62	JPC-51	JPC-52
SiO2	73.04	71.18	70.97	74.07	71.66	72.13	71.99	73.37	71.55	71.54	73.60	70.78	72.76	73.31	71.53	71.37
Al2O3	15.07	14.88	15.14	14.33	14.95	14.88	15.02	14.56	14.70	15.20	14.40	14.89	14.50	15.40	14.92	15.19
$Fe2O3^T$	1.04	1.91	2.36	0.51	1.94	1.56	1.50	1.28	1.45	1.56	1.36	1.90	1.32	0.92	1.48	1.41
FeO^T	0.94	1.72	2.12	0.46	1.75	1.40	1.35	1.15	1.30	1.40	1.22	1.71	1.19	0.83	1.33	1.27
MnO	0.02	0.03	0.02	0.01	0.02	0.02	0.02	0.02	0.03	0.02	0.02	0.03	0.03	0.04	0.02	0.02
MgO	0.26	0.46	0.57	0.09	0.60	0.65	0.65	0.25	0.29	0.43	0.32	0.48	0.23	0.10	0.71	0.60
CaO	0.55	0.71	0.88	0.34	0.45	0.36	0.36	0.53	0.62	0.60	0.55	0.71	0.57	0.44	0.34	0.33
Na2O	2.90	2.51	2.61	1.99	2.67	3.14	3.03	2.98	3.30	3.04	2.79	2.83	3.15	3.92	3.87	3.04
K2O	5.24	5.43	5.98	7.57	5.61	5.38	5.54	4.99	5.02	5.34	5.28	5.56	5.01	4.05	5.47	6.09
TiO2	0.15	0.29	0.54	0.06	0.32	0.27	0.25	0.19	0.19	0.27	0.21	0.33	0.16	0.08	0.22	0.27
P2O5	0.38	0.48	0.41	0.55	0.33	0.37	0.39	0.36	0.40	0.44	0.41	0.35	0.35	0.45	0.38	0.33
LOI	0.94	1.28	1.20	0.90	1.34	1.09	1.13	1.61	0.96	1.25	1.30	1.11	0.96	1.23	0.98	1.19
Total	99.59	99.15	100.70	100.40	101.64	101.25	101.23	100.10	98.52	99.67	100.20	98.96	99.01	99.95	101.25	101.11
Sc	1.00	3.00	2.00	< 1	<7	<7	<7	2.00	2.00	2.00	3.00	2.00	2.00	2.00	<7	<7
V	8.00	10.00	17.00	< 5	11.00	7.00	8.00	7.00	5.00	11.00	7.00	13.00	< 5	< 5	7.00	8.00
Ba	211.00	279.00	357.00	143.00	258.00	235.00	217.00	243.00	225.00	262.00	206.00	263.00	139.00	46.00	213.00	261.00
Sr	60.00	68.00	84.00	54.00	69.00	67.00	62.00	57.00	57.00	64.00	54.00	80.00	48.00	27.00	62.00	79.00
Y	5.00	17.00	10.00	9.00	12.00	10.00	12.00	7.00	7.00	10.00	7.00	7.00	6.00	6.00	10.00	9.00
Zr	57.00	137.00	287.00	23.00	129.00	108.00	104.00	64.00	70.00	106.00	84.00	117.00	64.00	40.00	96.00	114.00
Cr	< 20	< 20	< 20	< 20	8.00	8.00	7.00	< 20	< 20	< 20	< 20	< 20	< 20	< 20	5.00	5.00
Ni	< 20	< 20	< 20	< 20	<7	<7	<7	< 20	< 20	< 20	< 20	< 20	< 20	< 20	<7	<7
Ga	23.00	24.00	27.00	22.00	22.00	22.00	22.00	22.00	22.00	22.00	22.00	27.00	23.00	26.00	20.00	23.00
Rb	325.00	316.00	376.00	401.00	284.00	343.00	311.00	311.00	342.00	330.00	338.00	416.00	419.00	521.00	339.00	371.00

Nb	5.00	9.00	7.00	3.00	10.54	11.26	11.68	9.00	9.00	7.00	9.00	9.00	14.00	15.00	10.08	8.87
Cs	20.30	18.40	11.50	13.60	-	-	-	13.30	27.00	15.20	18.90	17.80	26.60	37.50	-	-
La	10.80	31.80	97.30	2.90	37.13	24.76	22.92	15.50	15.90	21.40	19.80	36.00	15.00	8.00	21.82	31.72
Ce	25.00	75.50	248.00	7.80	85.76	54.74	52.13	34.00	34.60	50.80	47.50	84.10	34.10	17.90	50.56	71.00
Pr	3.08	9.37	31.50	1.05	11.01	6.94	6.70	4.01	3.98	6.28	5.85	10.30	4.08	2.13	6.57	9.03
Nd	12.40	35.40	119.00	4.30	41.49	26.35	25.79	14.80	15.20	24.10	22.40	38.50	14.50	7.80	25.37	34.11
Sm	3.10	8.10	20.50	1.50	8.33	6.07	6.00	3.70	3.80	5.80	4.50	8.50	3.60	1.90	5.77	7.68
Eu	0.41	0.54	0.78	0.33	0.42	0.42	0.40	0.34	0.36	0.51	0.38	0.62	0.33	0.13	0.37	0.54
Gd	2.30	6.20	9.30	1.50	5.12	4.50	4.59	3.40	3.50	4.60	3.20	5.40	2.80	1.60	3.96	5.16
Tb	0.30	0.90	0.80	0.30	0.63	0.54	0.63	0.50	0.50	0.60	0.40	0.60	0.40	0.30	0.51	0.58
Dy	1.20	4.00	2.90	1.70	2.75	2.18	2.82	1.90	2.00	2.40	1.80	2.00	1.80	1.30	2.29	2.18
Ho	0.20	0.60	0.30	0.30	0.39	0.29	0.38	0.20	0.20	0.30	0.20	0.20	0.20	0.20	0.32	0.29
Er	0.40	1.30	0.70	0.70	0.84	0.58	0.78	0.40	0.40	0.60	0.60	0.60	0.50	0.50	0.70	0.56
Tm	0.05	0.15	0.09	0.08	0.09	0.07	0.10	0.06	0.05	0.07	0.07	0.06	0.06	0.06	0.08	0.07
Yb	0.30	0.80	0.50	0.50	0.60	0.38	0.55	0.30	0.30	0.40	0.40	0.30	0.30	0.40	0.47	0.43
Lu	0.01	0.10	0.07	0.06	0.08	0.05	0.06	0.04	0.04	0.06	0.06	0.04	0.04	0.06	0.06	0.06
Hf	1.50	3.70	7.00	1.00	1.55	<0.06	1.50	1.70	1.90	2.80	2.20	3.10	1.80	1.50	1.31	3.02
Ta	0.90	1.10	0.80	0.40	0.58	1.14	1.14	1.80	1.90	1.20	1.50	1.00	3.30	4.90	1.20	0.86
Pb	28.00	36.00	39.00	43.00	38.00	35.00	35.00	27.00	27.00	31.00	29.00	36.00	32.00	16.00	36.00	43.00
Th	6.80	22.20	107.00	1.20	39.25	22.16	20.21	6.90	7.20	13.90	15.60	28.50	9.10	5.10	20.86	33.69
U	6.70	12.60	10.70	3.50	16.30	11.93	14.03	5.10	9.40	8.70	11.10	15.00	13.70	4.50	10.69	5.84
REE	59.55	174.76	531.74	23.02	194.63	127.86	123.85	79.15	80.83	117.92	107.16	187.22	77.71	42.28	118.85	163.41
LREE	54.38	160.17	516.30	17.55	183.71	118.86	113.54	72.01	73.48	108.38	100.05	177.40	71.28	37.73	110.09	153.54
HREE	5.17	14.59	15.44	5.47	10.92	9.00	10.31	7.14	7.35	9.54	7.11	9.82	6.43	4.55	8.76	9.88
LREE/HREE	10.52	10.98	33.44	3.21	16.83	13.20	11.01	10.09	10.00	11.36	14.07	18.07	11.09	8.29	12.57	15.55
La/Yb_N	24.24	26.77	131.06	3.91	41.48	43.79	27.82	34.80	35.69	36.03	33.34	80.82	33.67	13.47	31.35	49.25
La/Sm_N	2.19	2.47	2.98	1.22	2.80	2.56	2.40	2.63	2.63	2.32	2.77	2.66	2.62	2.65	2.38	2.59
Dy/Yb_N	2.60	3.25	3.77	2.21	2.96	3.72	3.30	4.11	4.33	3.90	2.92	4.33	3.90	2.11	3.18	3.27
Tb/Yb_N	4.40	4.95	7.04	2.64	4.57	6.24	5.00	7.33	7.33	6.60	4.40	8.80	5.87	3.30	4.82	5.83
Eu/Eu*	0.47	0.23	0.17	0.67	0.20	0.24	0.24	0.29	0.30	0.30	0.31	0.28	0.32	0.23	0.24	0.26

Table 2 *continued*

Lithology	Granite													
Sample	JPC-53	JTJ-35	JPC-50	JTJ-11	JTJ-12	JPC-55	JTJ-59	JTJ-13	JPC-19	JPC-24	JPC-59	JPC-54	JTJ-36	JTJ-58
SiO2	71.62	70.63	71.41	71.13	71.39	70.32	71.96	71.78	70.64	72.31	75.24	73.33	72.64	73.41
Al2O3	15.20	15.10	15.05	14.71	15.01	15.51	14.50	14.60	15.15	14.64	13.95	14.72	14.91	14.81
$Fe2O3^T$	1.72	2.14	1.51	1.64	1.84	2.15	1.66	1.63	1.73	1.89	0.70	1.19	1.34	0.82
FeO^T	1.55	1.93	1.36	1.48	1.66	1.93	1.49	1.47	1.56	1.70	0.63	1.07	1.21	0.74
MnO	0.02	0.02	0.02	0.02	0.02	0.03	0.04	0.02	0.02	0.03	0.02	0.02	0.02	0.03
MgO	0.70	0.59	0.55	0.43	0.41	0.75	0.54	0.36	0.63	0.64	0.36	0.48	0.31	0.19
CaO	0.40	0.72	0.26	0.73	0.61	0.58	1.01	0.58	0.46	0.37	0.09	0.24	0.63	0.55
Na2O	3.02	2.57	2.99	3.06	2.72	3.16	3.54	2.66	2.63	2.80	3.48	2.98	3.25	3.27
K2O	5.53	5.37	5.93	5.43	5.39	5.32	4.86	5.71	6.91	5.39	4.33	5.20	4.97	4.59
TiO2	0.31	0.44	0.22	0.28	0.28	0.42	0.28	0.28	0.40	0.31	0.10	0.19	0.19	0.10
P2O5	0.37	0.48	0.47	0.37	0.40	0.39	0.29	0.49	0.31	0.36	0.30	0.30	0.44	0.35
LOI	0.95	1.51	1.44	0.94	1.06	1.21	1.02	1.21	0.84	1.01	1.32	1.21	1.11	1.67

Total	101.39	99.58	101.21	98.71	99.14	101.77	99.70	99.31	101.28	101.45	100.52	100.93	99.82	99.78
Sc	<7	3.00	<7	2.00	2.00	<7	3.00	2.00	<7	<7	<7	<7	2.00	3.00
V	8.00	19.00	<5	11.00	9.00	18.00	17.00	10.00	8.00	9.00	<5	5.00	7.00	< 5
Ba	240.00	376.00	183.00	283.00	235.00	287.00	491.00	268.00	407.00	172.00	134.00	146.00	274.00	201.00
Sr	76.00	93.00	47.00	80.00	63.00	74.00	142.00	76.00	106.00	49.00	42.00	46.00	74.00	61.00
Y	10.00	10.00	14.00	9.00	11.00	10.00	8.00	8.00	9.00	11.00	5.00	6.00	9.00	7.00
Zr	123.00	211.00	86.00	112.00	116.00	198.00	130.00	113.00	193.00	130.00	35.00	72.00	74.00	46.00
Cr	9.00	< 20	6.00	< 20	< 20	11.00	< 20	< 20	6.00	7.00	<5	5.00	< 20	< 20
Ni	<7	< 20	<7	< 20	< 20	<7	< 20	< 20	<7	<7	<7	<7	< 20	< 20
Ga	24.00	25.00	23.00	22.00	22.00	25.00	23.00	25.00	23.00	24.00	20.00	22.00	23.00	18.00
Rb	371.00	358.00	403.00	334.00	357.00	369.00	276.00	381.00	305.00	378.00	277.00	293.00	288.00	281.00
Nb	11.61	7.00	14.99	8.00	10.00	9.94	10.00	8.00	4.32	15.97	12.91	7.92	10.00	9.00
Cs	-	10.60	-	14.80	18.30	-	19.10	13.00	-	-	-	-	17.00	18.90
La	33.65	65.40	16.95	26.60	30.40	64.65	38.80	31.20	61.40	37.77	5.03	14.98	12.40	8.50
Ce	75.62	162.00	39.29	60.00	72.70	151.70	77.60	72.00	135.11	87.83	11.04	33.71	26.90	17.70
Pr	9.74	20.40	5.00	7.08	8.82	19.91	8.80	8.88	16.41	11.35	1.36	4.24	3.27	2.09
Nd	36.91	75.60	18.49	26.50	33.50	75.41	30.80	33.80	61.23	43.58	5.09	15.65	12.40	7.50
Sm	8.17	12.90	3.94	6.30	7.00	12.56	5.50	7.40	13.18	9.40	1.22	3.56	3.30	2.20
Eu	0.50	0.74	0.25	0.57	0.45	0.59	0.75	0.56	0.79	0.46	0.11	0.23	0.34	0.51
Gd	5.30	6.40	2.91	4.50	5.10	6.18	3.70	4.80	7.47	5.84	1.20	2.62	3.00	2.10
Tb	0.61	0.70	0.50	0.60	0.70	0.68	0.40	0.60	0.70	0.72	0.19	0.34	0.50	0.30
Dy	2.43	2.80	2.66	2.20	2.80	2.60	1.90	2.10	2.39	2.92	0.95	1.46	2.30	1.80
Ho	0.30	0.40	0.41	0.30	0.40	0.38	0.30	0.30	0.30	0.43	0.15	0.18	0.30	0.30
Er	0.60	0.80	0.91	0.60	0.80	0.82	0.60	0.60	0.69	0.95	0.32	0.40	0.60	0.60
Tm	0.07	0.11	0.11	0.07	0.10	0.10	0.09	0.07	0.06	0.11	0.04	0.04	0.08	0.08
Yb	0.39	0.60	0.64	0.40	0.50	0.62	0.60	0.30	0.46	0.66	0.27	0.26	0.50	0.50
Lu	0.05	0.09	0.08	0.06	0.07	0.08	0.09	0.05	0.05	0.07	0.04	0.03	0.06	0.07
Hf	2.21	5.10	0.48	2.80	3.10	5.09	3.40	2.90	2.18	2.09	1.06	<0.06	2.10	1.50
Ta	1.05	0.80	1.61	1.10	1.60	1.27	1.40	0.90	0.52	1.23	2.09	1.07	2.10	2.50
Pb	39.00	34.00	34.00	36.00	33.00	36.00	34.00	37.00	53.00	34.00	21.00	33.00	26.00	42.00
Th	32.41	57.10	21.08	14.00	22.30	66.13	17.00	24.60	38.52	36.34	2.48	14.02	4.90	3.40
U	19.28	11.60	12.44	9.90	10.70	13.69	10.30	10.60	10.11	13.20	3.67	13.15	5.70	5.80
REE	174.34	348.94	92.13	135.78	163.34	336.28	169.93	162.66	300.24	202.10	27.00	77.70	65.95	44.25
LREE	164.08	336.30	83.67	126.48	152.42	324.23	161.50	153.28	287.33	189.93	23.74	72.14	58.27	37.99
HREE	10.26	12.64	8.46	9.30	10.92	12.05	8.43	9.38	12.91	12.17	3.27	5.56	7.68	6.26
LREE/HREE	15.99	26.61	9.89	13.60	13.96	26.90	19.16	16.34	22.27	15.61	7.27	12.98	7.59	6.07
La/Yb_N	58.29	73.41	17.92	44.79	40.95	69.91	43.55	70.04	90.16	38.33	12.66	38.24	16.70	11.45
La/Sm_N	2.59	3.19	2.70	2.65	2.73	3.23	4.43	2.65	2.93	2.53	2.60	2.64	2.36	2.43
Dy/Yb_N	4.06	3.03	2.71	3.57	3.64	2.71	2.06	4.55	3.39	2.86	2.31	3.58	2.99	2.34
Tb/Yb_N	6.94	5.13	3.45	6.60	6.16	4.82	2.93	8.80	6.72	4.78	5.69	3.12	4.40	2.64
Eu/Eu*	0.23	0.25	0.23	0.33	0.23	0.20	0.51	0.29	0.24	0.19	0.28	0.23	0.33	0.73

Table 3

Lithology	Phyllite			Metatexite					Type-1 Diatexite				Type-2 Diatexite	Granite X	Granite IX	Granite VIII	Granite V	Granite III	Granite II
Sample	M1_2_1	M1_2_2	M1_2_3	M1_20_1	M2_25_1	M3_8_1	M4_60A_1	M5_53_1	M2_43_1	M2_43_2	M3_55_1	M3_55_2	M1_24A_1	M4_34_1	M3_10_1	M2_35_1	M1_12_1	M5_13_1	M4_36_1
Sr	317	1471	333	167	243	487	113	183	112	115	144	131	86	78	99	96	74	76	133
Y	854	480	697	1973	1915	837	1618	1457	847	852	1569	1634	2026	908	542	1026	1546	1083	212
Th	27	97	18	1	1	50	1	0	15	21	1	0	1	7	5	5	19	5	4
U	8	34	18	223	32	17	91	46	33	47	135	123	185	49	51	62	74	75	81
La	386	1585	897	162	167	405	159	126	496	538	192	169	214	391	330	344	380	340	276
Ce	1124	2019	1672	547	559	921	503	425	1848	1924	654	557	574	1404	879	1230	1289	1129	561
Pr	175	174	179	91	97	107	83	74	329	336	114	96	79	241	120	214	215	181	66
Nd	931	630	747	513	565	455	457	435	1760	1808	643	533	348	1282	514	1115	1114	899	259
Sm	253	94	143	216	245	120	190	195	491	502	321	261	142	432	168	377	414	363	67
Eu	21	21	19	17	26	29	16	17	10	10	14	14	11	10	17	13	8	11	22
Gd	252	98	158	301	350	145	255	278	315	321	444	361	194	334	160	318	392	345	59
Tb	33	16	22	60	67	27	50	52	39	39	82	69	48	45	28	47	66	54	10
Dy	169	100	130	386	410	166	316	320	181	184	404	378	341	205	124	226	327	255	46
Ho	29	18	25	77	78	31	61	60	29	30	55	58	67	31	15	35	49	36	6
Er	67	42	60	199	190	78	155	146	68	68	101	130	192	64	31	75	104	73	12
Tm	8	5	8	28	25	11	22	19	9	9	11	17	32	8	4	9	13	8	2
Yb	51	33	46	183	148	73	145	120	52	53	64	111	231	41	24	53	70	46	10
Lu	7	4	7	25	19	9	19	16	7	7	8	14	31	5	3	6	8	5	1
LREE	2870	4503	3638	1529	1632	2008	1391	1255	4924	5108	1923	1615	1357	3750	2011	3279	3413	2911	1229
HREE	638	338	474	1275	1311	569	1039	1028	709	720	1183	1153	1147	742	407	783	1036	833	168
REE	3508	4841	4112	2804	2943	2577	2431	2283	5633	5829	3106	2768	2504	4493	2418	4062	4448	3744	1397
Eu/Eu*	0.25	0.67	0.39	0.20	0.27	0.67	0.22	0.22	0.07	0.08	0.12	0.14	0.19	0.08	0.33	0.11	0.06	0.09	1.06
La/Yb_N	5.1	32.6	13.0	0.6	0.8	3.7	0.7	0.7	6.4	6.8	2.0	1.0	0.6	6.5	9.1	4.3	3.7	5.0	19.1
La/Sm_N	1.0	10.6	3.9	0.5	0.4	2.1	0.5	0.4	0.6	0.7	0.4	0.4	0.9	0.6	1.2	0.6	0.6	0.6	2.6
Dy/Yb_N	2.1	2.0	1.8	1.4	1.8	1.5	1.4	1.7	2.3	2.2	4.1	2.2	1.0	3.3	3.3	2.8	3.0	3.6	3.1

Table 4

Lithology	Metatexite											Type-1 Diatexite		Type-2 Diatexite	Granite X							Granite IX	Granite V
Sample	M1T_20_11c - 1	M1T_20_25c - 1	M1T_20_46c - 1	M1T_20_57c - 1	M1T_20_78c - 1	M6T_25_1c - 1	M6T_25_2c - 1	M6T_25_3c - 1	M6T_25_4c - 1	M6T_25_5c - 1	M6T_25_7c - 1	M6T_55_10c - 1	M6T_55_12c - 1	M1T_24A_17c - 1	M6T_34_10c - 1	M6T_34_15c - 1	M6T_34_23c - 1	M6T_34_24c - 1	M6T_34_26c - 1	M6T_34_27c - 1	M6T_34_3c - 1	M6T_45_1 - 1	M6T_12_1c - 1
Hf	10140	11080	8180	12530	10000	14300	13290	13260	13300	14410	14360	12750	11060	11810	12850	11660	11990	12070	12430	12670	12650	10280	11950
U	1152	341	97	2171	851	1310	1137	1261	1378	1213	1239	475	1514	321	734	1258	1182	1603	1480	1000	190	898	2770
Th	419	288	57	520	253	4	3	6	4	4	5	28	117	37	84	314	284	398	7400	980	68	214	16300
Th/U	0.36	0.85	0.58	0.24	0.30	0.003	0.003	0.005	0.003	0.003	0.004	0.06	0.08	0.12	0.11	0.25	0.24	0.25	5.00	0.98	0.36	0.24	5.88
Y	-	-	677	-	120	-	-	-	-	-	2074	-	-	610	469	855	797	1199	985	592	799	-	-
La	56	0.2	<LOD	14	3	<LOD	<LOD	<LOD	<LOD	<LOD	1	0.1	11	0.2	0.1	2	4	22	731	64	<LOD	2	-
Ce	95	23	22	70	29	0.1	0.1	0.1	0.1	0.1	5	1	54	15	2	17	38	260	-	64	5	17	-
Pr	8	0.2	0.1	12	3	<LOD	<LOD	0.02	<LOD	<LOD	1	0.1	11	0.3	0.3	4	9	33	377	115	0.1	4	-
Nd	34	3	2	79	21	0.2	0.2	0.2	0.1	0.2	6	1	68	2	3	31	70	209	1920	950	1	27	-
Sm	18	6	3	57	18	1	1	1	1	1	5	2	47	2	6	26	50	90	1170	153	2	25	3440
Eu	4	1	1	15	4	0.2	0.2	0.2	0.2	0.2	2	0.2	9	0.5	0.1	1	2	5	7	2	0.1	1	18

Gd	57	30	15	131	54	12	10	12	12	10	24	14	144	12	23	49	70	106	450	89	13	75	1380
Tb	18	10	5	33	16	7	6	8	8	7	11	7	48	4	6	12	14	20	40	13	5	19	115
Dy	201	128	58	327	182	139	111	143	143	127	177	98	489	54	58	106	111	158	196	97	76	168	457
Ho	69	48	21	94	62	64	52	65	66	59	73	38	120	20	15	28	26	39	38	24	29	45	71
Er	309	230	105	391	288	388	320	394	407	354	419	188	369	101	55	104	91	136	124	89	131	180	200
Tm	63	49	23	77	62	112	94	112	118	103	115	44	55	23	10	19	16	24	21	17	26	35	31
Yb	534	439	215	647	552	1305	1090	1284	1368	1193	1307	434	381	225	80	146	118	178	157	132	214	296	231
Lu	104	92	48	122	116	297	248	290	309	269	295	91	64	48	14	25	20	30	27	23	39	58	38
LREE	212	32	27	232	73	1	1	1	1	1	19	4	190	19	11	80	170	614	4198	1346	8	75	3440
HREE	1357	1026	490	1837	1334	2324	1930	2308	2430	2122	2423	915	1679	488	261	490	468	696	1058	486	533	877	2540
REE	1569	1059	517	2069	1407	2325	1931	2309	2432	2124	2442	919	1869	507	272	570	638	1310	5256	1832	542	952	5980
Yb/Gd_N	11.64	18.19	17.93	6.11	12.73	138.14	140.38	127.71	144.81	141.15	67.50	38.07	3.27	23.07	4.25	3.65	2.08	2.08	0.43	1.83	19.91	4.89	0.21
Ce/YbN	0.05	0.01	0.03	0.03	0.01	0.00003	0.00002	0.00002	0.00001	0.00001	0.001	0.001	0.04	0.02	0.01	0.03	0.08	0.4	-	0.1	0.01	0.01	-
Eu/Eu*	0.34	0.30	0.51	0.52	0.43	0.17	0.17	0.16	0.17	0.17	0.44	0.14	0.33	0.26	0.03	0.09	0.12	0.16	0.03	0.04	0.04	0.07	0.02
Ce/Ce*	1.09	26.09	-	1.30	2.49	-	-	-	-	-	1.15	3.77	1.22	14.55	2.43	1.39	1.52	2.34	-	0.18	-	1.43	-

Table 5

Lithology	Phyllite N	Phyllite S	Metatexite					Type-1 Diatexite		Type-2 Diatexite	Granite X	Granite IX	Granite VIII	Granite V	Granite II
Sample	JTJ-2	JTJ-19	JTJ-20	JTJ-25	JTJ-48B	JTJ-53	JTJ-60A	JTJ-43	JTJ-55	JTJ-24A	JTJ-34	JTJ-45	JTJ-35	JTJ-12	JTJ-36
$^{87}Sr/^{86}Sr$	0.7250	0.7402	0.7245	0.7321	0.7318	0.7403	0.7489	0.7364	0.7340	0.7447	0.7648	0.7893	0.7636	0.7774	0.7578
±2σ	0.000013	0.000016	0.000019	0.000016	0.000013	0.000017	0.000034	0.000018	0.000065	0.000020	0.000015	0.000024	0.000025	0.000013	0.000021
$^{87}Sr/^{86}Sr_{320}$	0.7153	0.7089	0.7097	0.7124	0.7039	0.7099	0.7053	0.7072	0.7204	0.7162	0.7055	0.7062	0.7126	0.7022	0.7063
$^{143}Nd/^{144}Nd$	0.5119	0.5126	0.5122	0.5121	0.5120	0.5121	0.5121	0.5120	0.5123	0.5122	0.5120	0.5121	0.5120	0.5120	0.5123
±2σ	0.000011	0.000006	0.000009	0.000010	0.000007	0.000009	0.000009	0.000009	0.000011	0.000007	0.000009	0.000008	0.000009	0.000012	0.000012
εNd	-13.42	0.15	-8.30	-10.91	-12.28	-10.57	-10.99	-12.77	-7.16	-8.28	-12.66	-11.06	-12.18	-11.51	-7.49
$εNd_{320}$	-10.07	3.28	-5.21	-7.65	-8.86	-7.30	-8.08	-8.32	-5.05	-6.21	-8.89	-7.99	-8.36	-8.64	-6.03
Nd T_{DM2} (Ma)[a]	1826	779	1445	1637	1731	1609	1670	1524	1690	1433	1714	1734	1693	1664	1510
$^{176}Hf/^{177}Hf$	0.2823	0.2824	0.2825	0.2824	0.2824	0.2825	0.2824	0.2824	0.2825	0.2824	0.2823	0.2824	0.2824	0.2824	0.2825
±2σ	0.000005	0.000005	0.000004	0.000009	0.000005	0.000004	0.000005	0.000005	0.000005	0.000007	0.000006	0.000006	0.000005	0.000004	0.000005
εHf	-18.14	-11.40	-8.98	-11.41	-12.09	-9.44	-12.82	-14.92	-9.25	-12.02	-15.16	-13.99	-14.21	-14.06	-10.16
$εHf_{320}$	-13.68	-7.16	-4.45	-7.99	-8.47	-6.45	-8.16	-8.16	-3.42	-9.25	-8.43	-7.78	-7.71	-7.70	-3.99

Hf T_{DM2} (Ma)[b]	2160	1747	1574	1800	1830	1701	1810	1880	1810	1508	1781	1828	1781	1786	1544
$^{208}Pb/^{204}Pb$	38.7956	38.6236	38.6820	38.8925	39.2638	38.6856	38.4898	39.9730	38.4068	38.2375	42.1802	38.6802	39.2789	38.9877	38.3497
±2σ	0.0021	0.0023	0.0023	0.0021	0.0018	0.0013	0.0022	0.0022	0.0026	0.0024	0.0022	0.0021	0.0017	0.0014	0.0023
$^{206}Pb/^{204}Pb$	18.3550	19.0401	18.7160	18.6505	18.6196	19.0338	18.5718	18.5110	18.4268	18.2206	19.0352	18.6156	18.6437	18.6888	18.6227
±2σ	0.0009	0.0010	0.0011	0.0010	0.0009	0.0005	0.0011	0.0010	0.0011	0.0009	0.0009	0.0010	0.0007	0.0006	0.0009
$^{207}Pb/^{204}Pb$	15.6924	15.6746	15.6434	15.6434	15.6485	15.6848	15.6502	15.6483	15.6407	15.6246	15.6830	15.6541	15.6583	15.6631	15.6618
±2σ	0.0008	0.0008	0.0009	0.0008	0.0007	0.0005	0.0009	0.0008	0.0010	0.0008	0.0008	0.0008	0.0007	0.0005	0.0008
$^{208}Pb/^{206}Pb$	2.1136	2.0285	2.0668	2.0853	2.1087	2.0325	2.0724	2.1594	2.0843	2.0986	2.2159	2.0778	2.1068	2.0862	2.0593
±2σ	0.000029	0.000033	0.000037	0.000046	0.000034	0.000027	0.000037	0.000041	0.000032	0.000037	0.000030	0.000046	0.000039	0.000045	0.000086
$^{207}Pb/^{206}Pb$	0.8549	0.8232	0.8358	0.8388	0.8404	0.8241	0.8427	0.8453	0.8488	0.8575	0.8239	0.8409	0.8399	0.8381	0.8410
±2σ	0.000011	0.000011	0.000013	0.000016	0.000010	0.000008	0.000011	0.000014	0.000010	0.000010	0.000010	0.000015	0.000010	0.000015	0.000024
$^{206}Pb/^{204}Pb_{320}$	17.8770	17.9549	17.9149	17.9774	17.7057	12.7938	18.0033	17.7218	17.9120	17.2398	18.1733	17.4132	17.5719	17.6702	17.9340
$^{207}Pb/^{204}Pb_{320}$	15.6671	15.6173	15.6011	15.6079	15.6002	15.3554	15.6201	15.6067	15.6135	15.5728	15.6375	15.5907	15.6017	15.6093	15.6254
$^{208}Pb/^{204}Pb_{320}$	38.0388	37.6798	38.1323	38.2769	38.6531	38.1212	38.2232	36.6712	38.2117	38.2151	39.3876	38.1326	37.5695	38.2999	38.1579

[a] $T_{DM2} = 1/\lambda \times \ln(^{143}Nd/^{144}Nd\text{-}(e^{\lambda t}\text{-}1) \times (^{147}Sm/^{144}Nd\text{-}^{147}Sm/^{144}Nd_{CC})\text{-}^{143}Nd/^{144}Nd_{DM} / (^{147}Sm/^{144}Nd_{CC}\text{-}^{147}Sm/^{144}Nd_{DM}) +1)$

[b] $T_{DM2} = 1/\lambda \times \ln(^{176}Hf/^{177}Hf\text{-}(e^{\lambda t}\text{-}1) \times (^{176}Lu/^{177}Hf\text{-}^{176}Lu/^{177}Hf_{CC})\text{-}^{176}Hf/^{177}Hf_{DM} / (^{176}Lu/^{177}Hf_{CC}\text{-}^{176}Lu/^{177}Hf_{DM}) +1)$

λRb - Steiger and Jäger (1977)

λSm - Lugmair and Marti (1978)

λLu - Söderlund et al. (2004)

λU and λTh - Steiger and Jäger (1977)

$^{147}Sm/^{144}Nd_{CHUR}$ and $^{143}Nd/^{144}Nd_{CHUR}$ - Jacobsen and Wasserburg (1980)

$^{147}Sm/144Nd_{DM}$,143Nd/$^{144}Nd_{DM}$, and $^{147}Sm/^{144}Nd_{CC}$ - Liew and Hofmann (1988)

$^{176}Lu/^{177}Hf_{CHUR}$ and $^{176}Hf/^{177}Hf_{CHUR}$ - Blichert-Toft and Albarède (1997)

$^{176}Lu/^{177}Hf_{DM}$ and $^{176}Hf/^{177}Hf_{DM}$ - Vervoort and Blichert-Toft (1999)

$^{176}Lu/^{177}Hf_{CC}$ - Griffin et al. (2002)

Fig.1

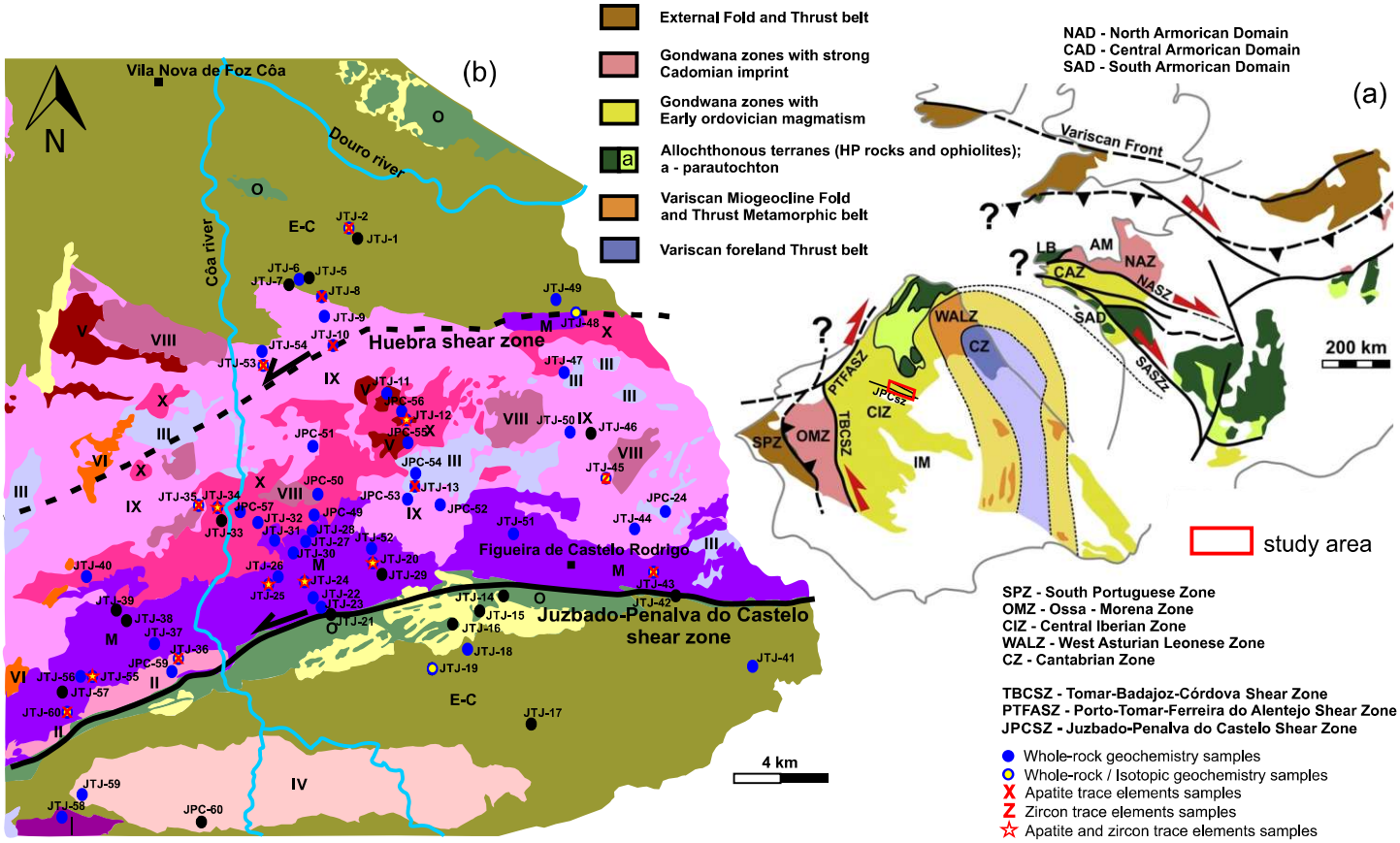
External Fold and Thrust belt
Gondwana zones with strong Cadomian imprint
Gondwana zones with Early ordovician magmatism
a
Allochthonous terranes (HP rocks and ophiolites); a - parautochton
Variscan Miogeocline Fold and Thrust Metamorphic belt
Variscan foreland Thrust belt
NAD - North Armorican Domain
CAD - Central Armorican Domain
SAD - South Armorican Domain
(a)
Variscan Front
LB
AM
NAZ
CAZ
NASZ
SAD
SASZ
WALZ
CZ
PTFASZ
JPCSZ
CIZ
TBCSZ
SPZ
OMZ
IM
200 km
study area
SPZ - South Portuguese Zone
OMZ - Ossa - Morena Zone
CIZ - Central Iberian Zone
WALZ - West Asturian Leonese Zone
CZ - Cantabrian Zone
TBCSZ - Tomar-Badajoz-Córdova Shear Zone
PTFASZ - Porto-Tomar-Ferreira do Alentejo Shear Zone
JPCSZ - Juzbado-Penalva do Castelo Shear Zone
Whole-rock geochemistry samples
Whole-rock / Isotopic geochemistry samples
Apatite trace elements samples
Zircon trace elements samples
Apatite and zircon trace elements samples
(b)
N
Vila Nova de Foz Côa
Douro river
Côa river
Huebra shear zone
Figueira de Castelo Rodrigo
Juzbado-Penalva do Castelo shear zone
E-C
O
M
4 km
Cenozoic deposits
I Póvoa de El-Rei-Sorval granite (Iy)
II São Pedro-Vieiro granite (IIy)
III Ribeira de Massueime-Galegos granite (IIIy)
IV Santa Eufémia-Bogalhal granite (IVy)
V Chãs-Amargo granite (Vy)
VI Castedo-Cabanas de Cima granite (VIy)
VIII Amêdo-Tomadias granite (VIIIy)
IX Mêda-Escalhão granite (IXy)
X Sta. Comba-Algodres granite (Xy)
M Migmatites
E-C Ediacaran-Cambrian formations
O Ordovician formations

Fig.2

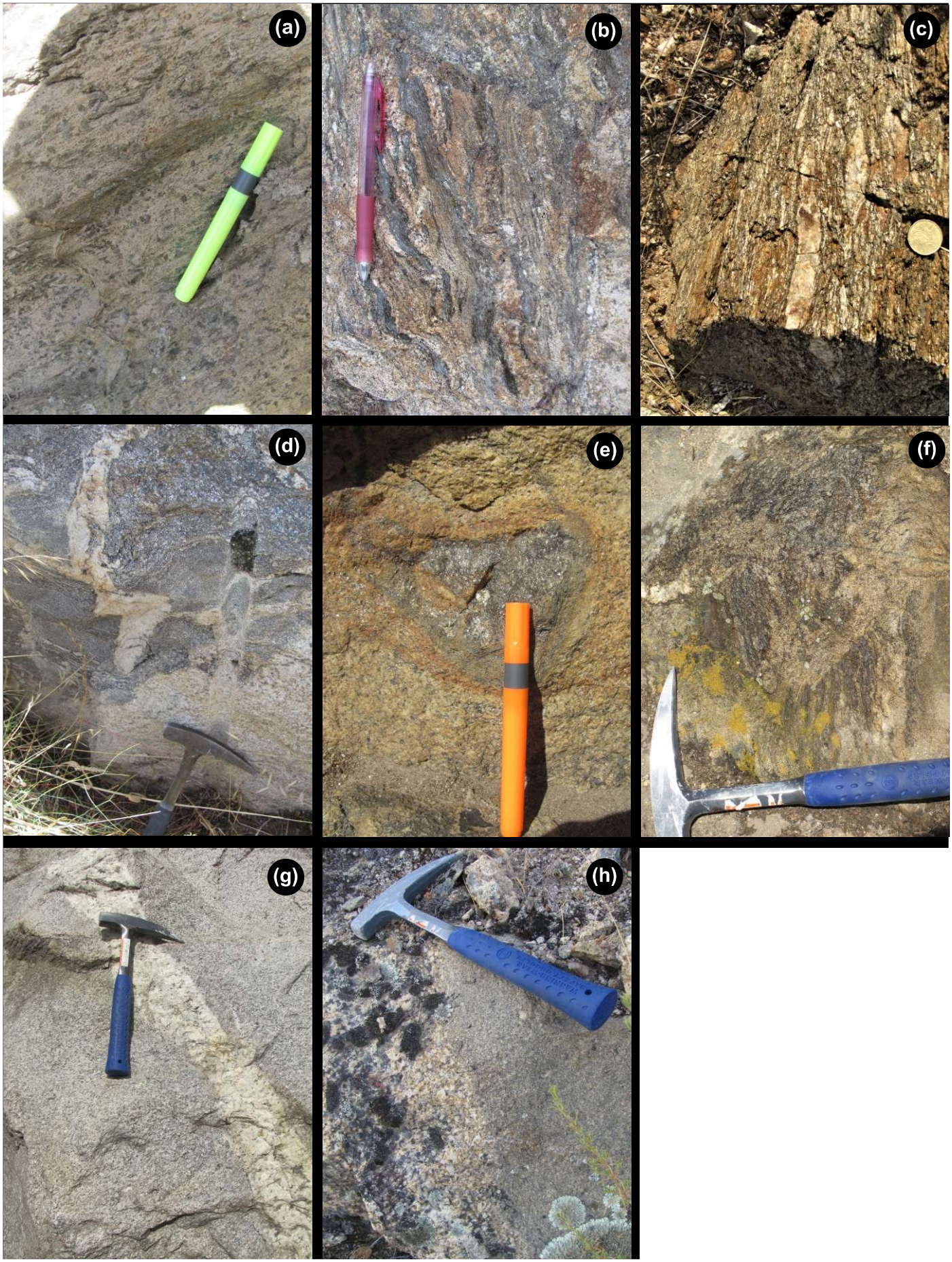

Fig.3

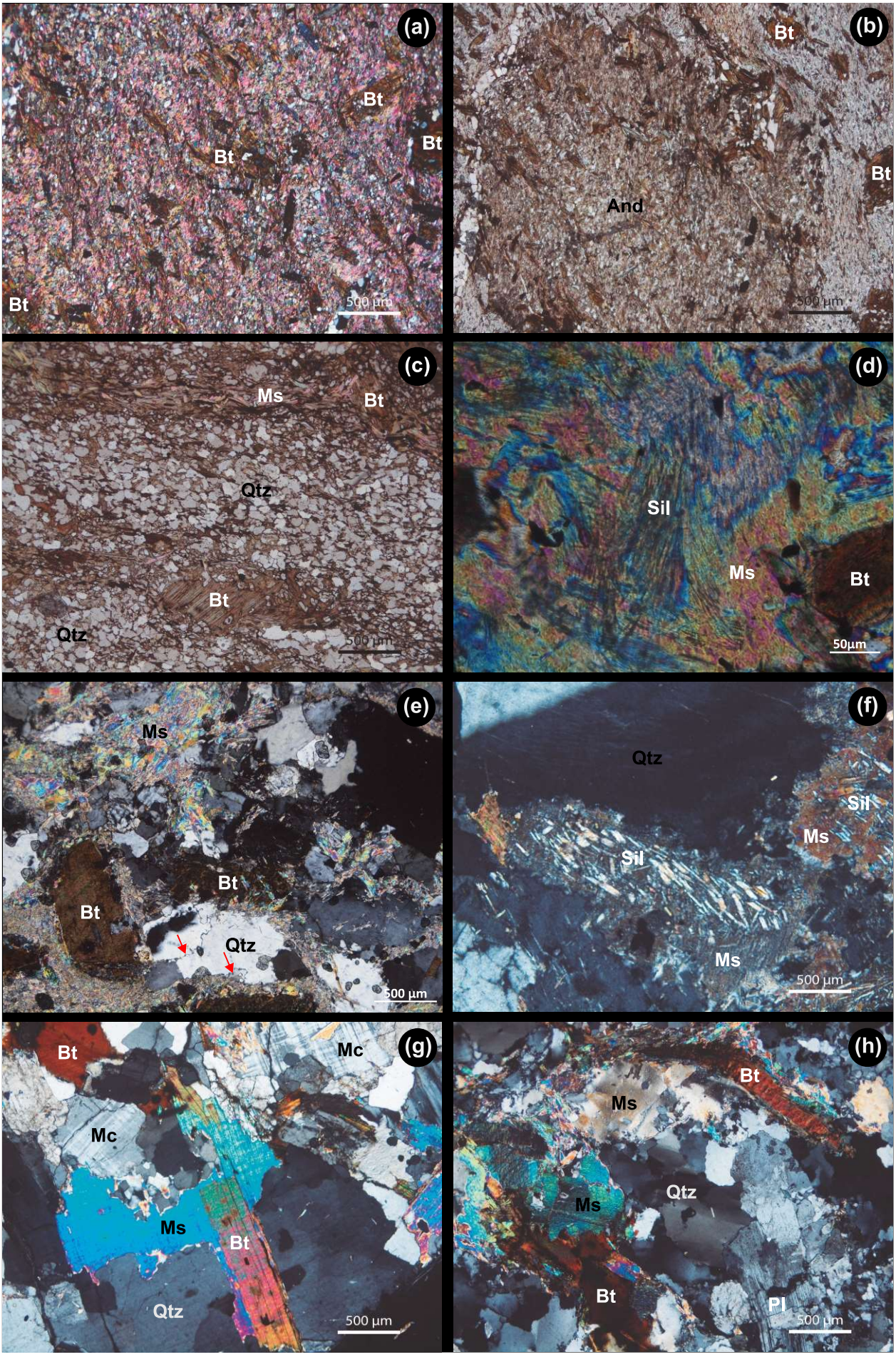
(a)
Bt
Bt
Bt
Bt
500 µm
(b)
Bt
Bt
And
500 µm
(c)
Ms
Bt
Qtz
Bt
Qtz
500 µm
(d)
Sil
Ms
Bt
50µm
(e)
Ms
Bt
Bt
Qtz
500 µm
(f)
Qtz
Sil
Ms
Sil
Ms
500 µm
(g)
Bt
Mc
Mc
Ms
Bt
Qtz
500 µm
(h)
Bt
Ms
Ms
Qtz
Bt
Pl
500 µm

Fig.4

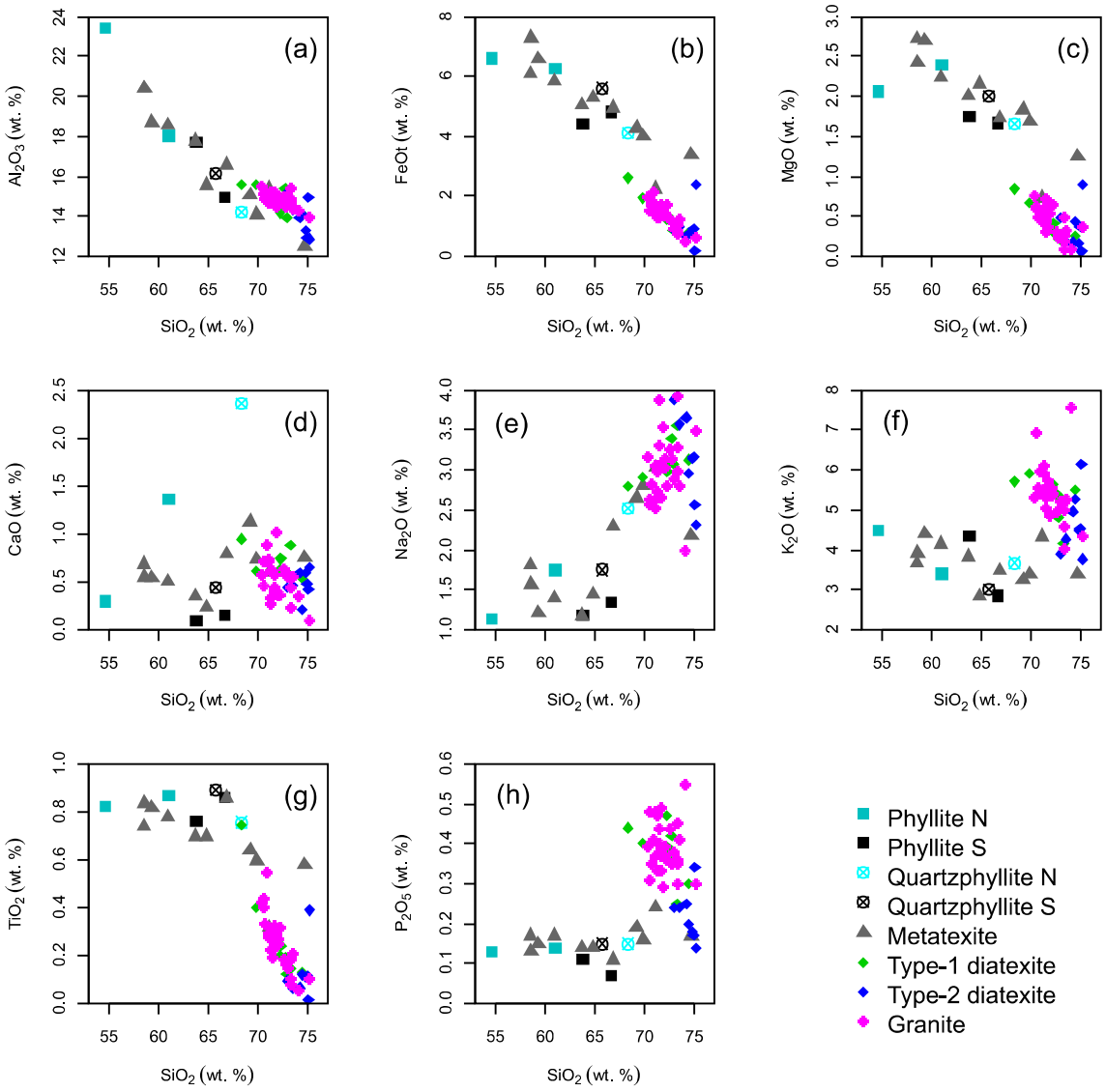
(a)
(b)
(c)
(d)
(e)
(f)
(g)
(h)
Al2O3 (wt. %)
FeOt (wt. %)
MgO (wt. %)
CaO (wt. %)
Na2O (wt. %)
K2O (wt. %)
TiO2 (wt. %)
P2O5 (wt. %)
SiO2 (wt. %)
Phyllite N
Phyllite S
Quartzphyllite N
Quartzphyllite S
Metatexite
Type-1 diatexite
Type-2 diatexite
Granite

Fig.5

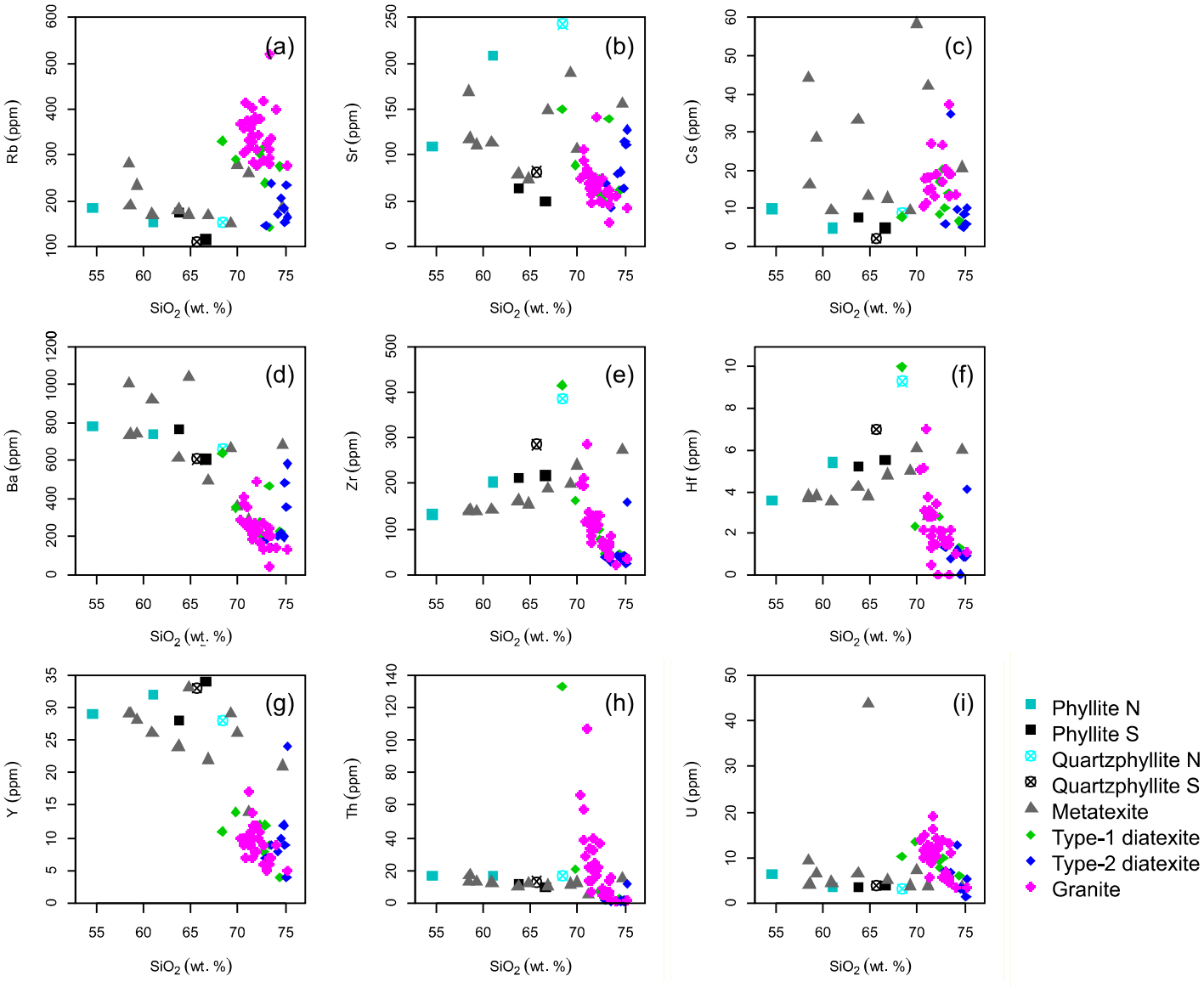
(a)
Rb (ppm)
100 200 300 400 500 600
(b)
Sr (ppm)
0 50 100 150 200 250
(c)
Cs (ppm)
0 10 20 30 40 50 60
(d)
Ba (ppm)
0 200 400 600 800 1000 1200
(e)
Zr (ppm)
0 100 200 300 400 500
(f)
Hf (ppm)
0 2 4 6 8 10
(g)
Y (ppm)
0 5 10 15 20 25 30 35
(h)
Th (ppm)
0 20 40 60 80 100 120 140
(i)
U (ppm)
0 10 20 30 40 50
55 60 65 70 75
SiO2 (wt. %)
Phyllite N
Phyllite S
Quartzphyllite N
Quartzphyllite S
Metatexite
Type-1 diatexite
Type-2 diatexite
Granite

Fig.6

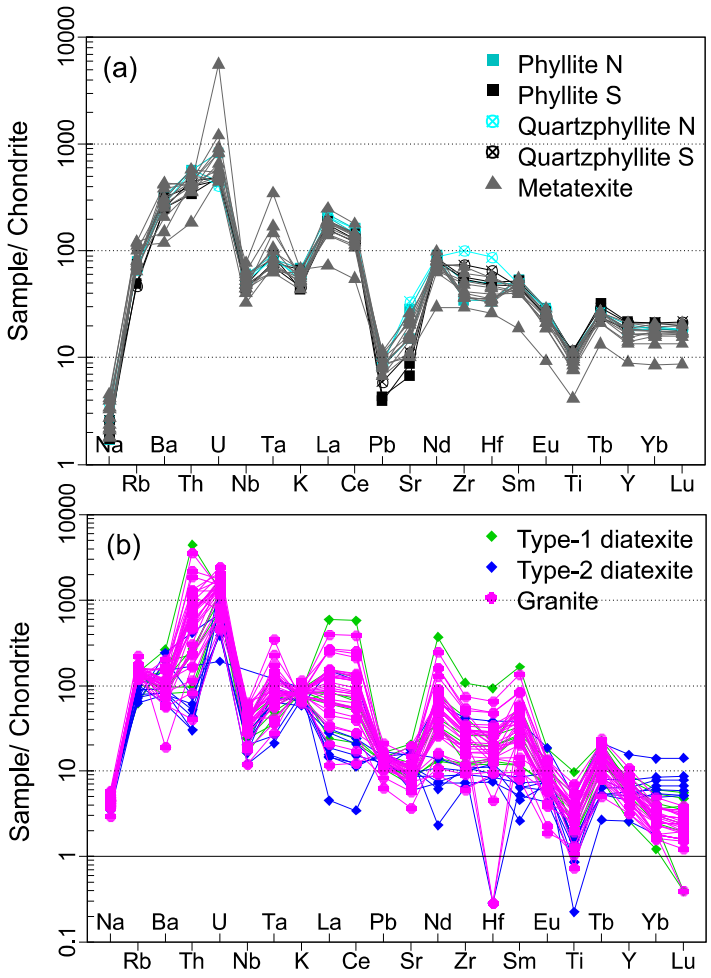
(a)
Phyllite N
Phyllite S
Quartzphyllite N
Quartzphyllite S
Metatexite
Sample/ Chondrite
10000
1000
100
10
1
Na Ba U Ta La Pb Nd Hf Eu Tb Yb
Rb Th Nb K Ce Sr Zr Sm Ti Y Lu
(b)
Type-1 diatexite
Type-2 diatexite
Granite
Sample/ Chondrite
10000
1000
100
10
1
0.1
Na Ba U Ta La Pb Nd Hf Eu Tb Yb
Rb Th Nb K Ce Sr Zr Sm Ti Y Lu

Fig.7

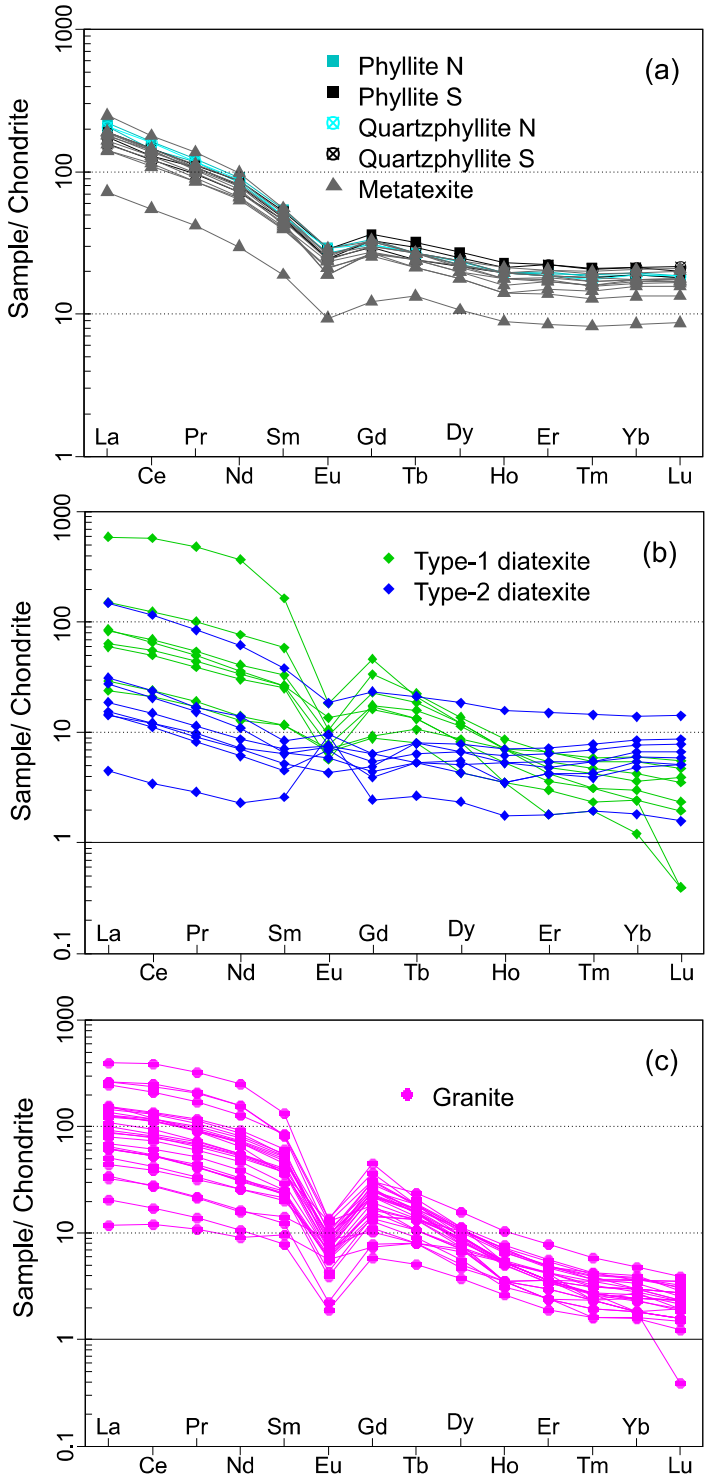
Sample/ Chondrite
1000
100
10
1
0.1
La
Ce
Pr
Nd
Sm
Eu
Gd
Tb
Dy
Ho
Er
Tm
Yb
Lu
(a)
Phyllite N
Phyllite S
Quartzphyllite N
Quartzphyllite S
Metatexite
(b)
Type-1 diatexite
Type-2 diatexite
(c)
Granite

Fig.8

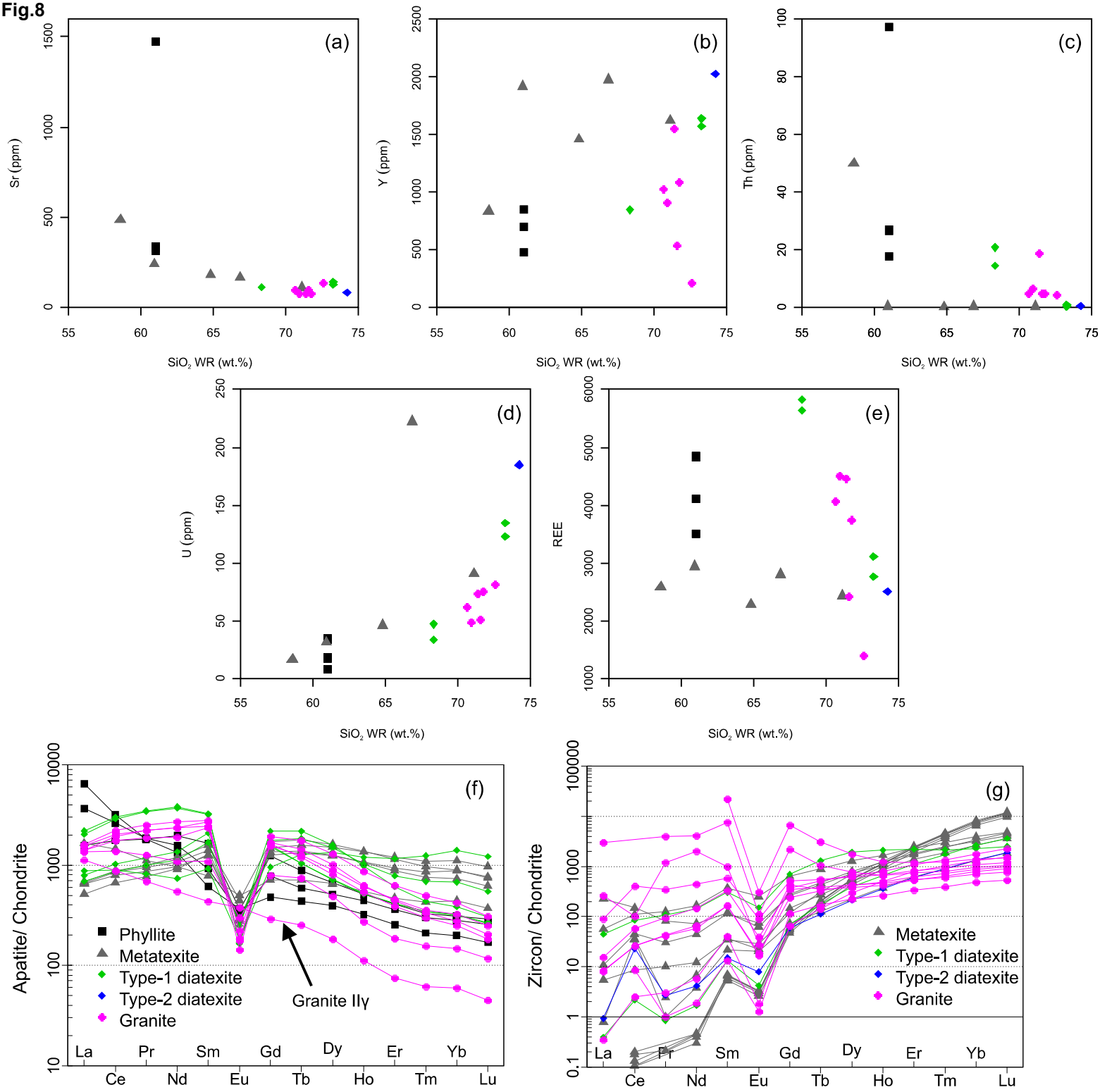
(a)
Sr (ppm)
SiO2 WR (wt.%)
(b)
Y (ppm)
SiO2 WR (wt.%)
(c)
Th (ppm)
SiO2 WR (wt.%)
(d)
U (ppm)
SiO2 WR (wt.%)
(e)
REE
SiO2 WR (wt.%)
(f)
Apatite/ Chondrite
Phyllite
Metatexite
Type-1 diatexite
Type-2 diatexite
Granite
Granite IIγ
La Ce Pr Nd Sm Eu Gd Tb Dy Ho Er Tm Yb Lu
(g)
Zircon/ Chondrite
Metatexite
Type-1 diatexite
Type-2 diatexite
Granite
La Ce Pr Nd Sm Eu Gd Tb Dy Ho Er Tm Yb Lu

Fig.9

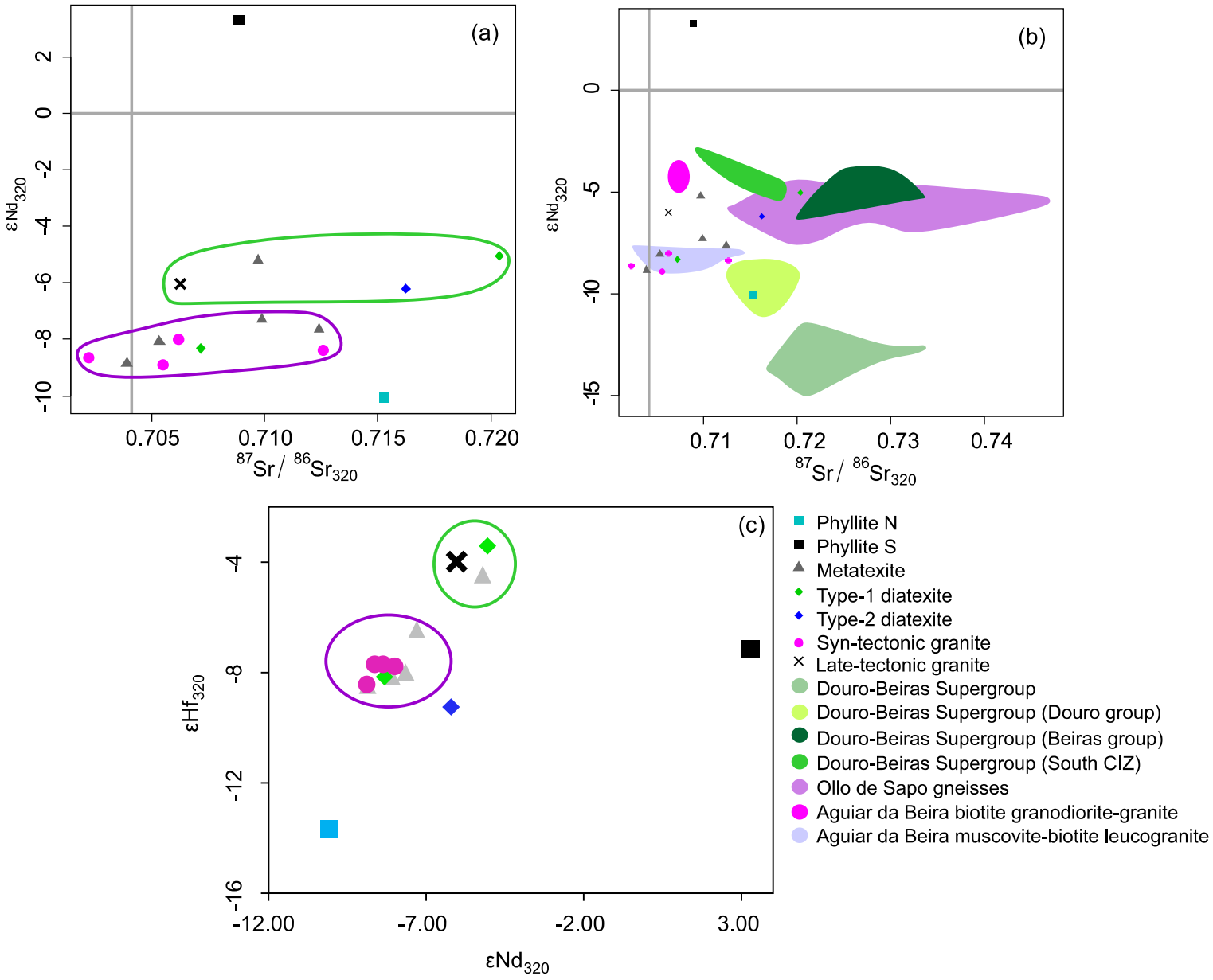
(a)
(b)
(c)
εNd320
87Sr/ 86Sr320
εHf320
Phyllite N
Phyllite S
Metatexite
Type-1 diatexite
Type-2 diatexite
Syn-tectonic granite
Late-tectonic granite
Douro-Beiras Supergroup
Douro-Beiras Supergroup (Douro group)
Douro-Beiras Supergroup (Beiras group)
Douro-Beiras Supergroup (South CIZ)
Ollo de Sapo gneisses
Aguiar da Beira biotite granodiorite-granite
Aguiar da Beira muscovite-biotite leucogranite

Fig.10

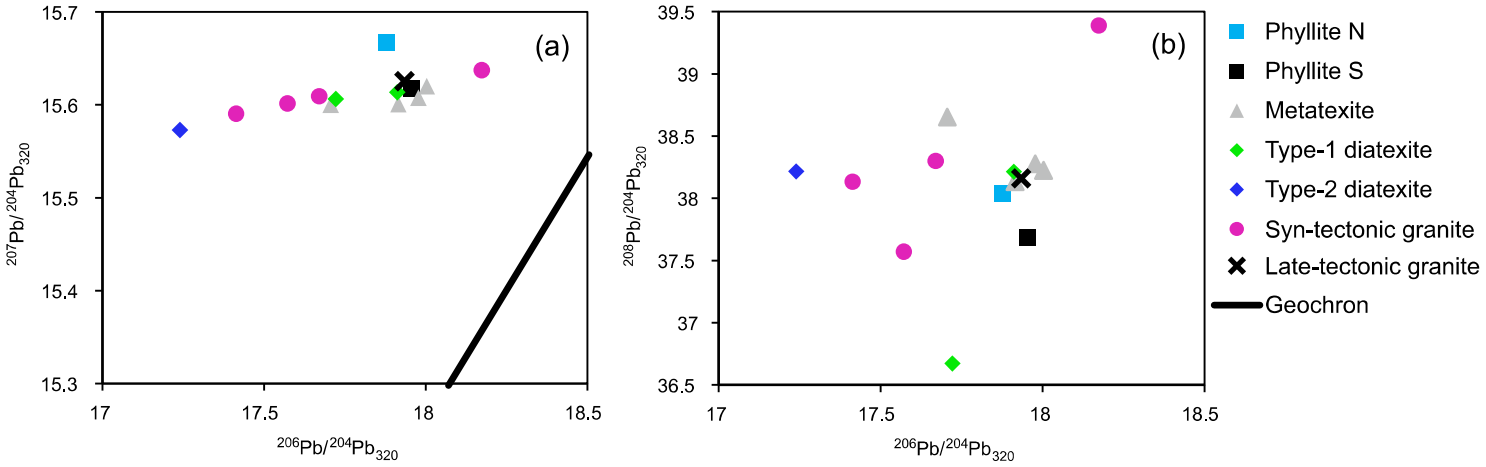
(a)
(b)
15.7
15.6
15.5
15.4
15.3
17
17.5
18
18.5
$^{207}Pb/^{204}Pb_{320}$
39.5
39
38.5
38
37.5
37
36.5
$^{208}Pb/^{204}Pb_{320}$
$^{206}Pb/^{204}Pb_{320}$
Phyllite N
Phyllite S
Metatexite
Type-1 diatexite
Type-2 diatexite
Syn-tectonic granite
Late-tectonic granite
Geochron

Fig.11

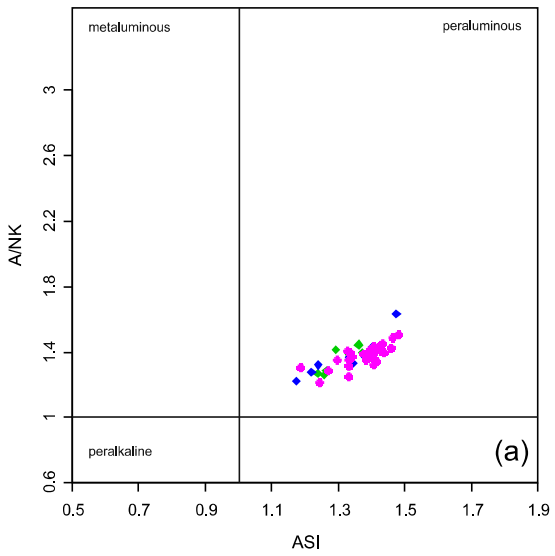

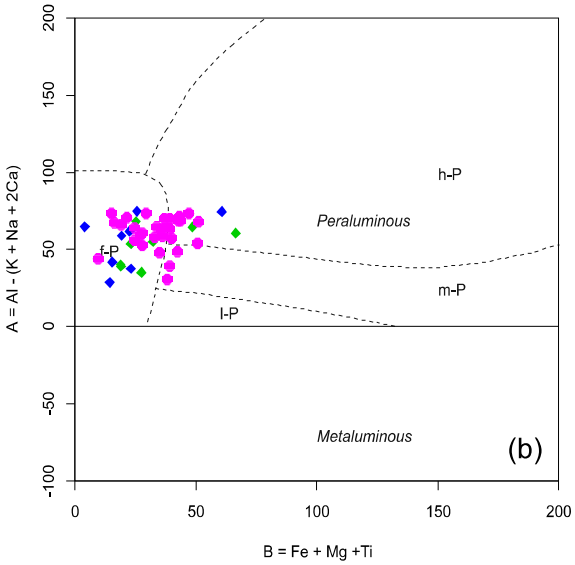

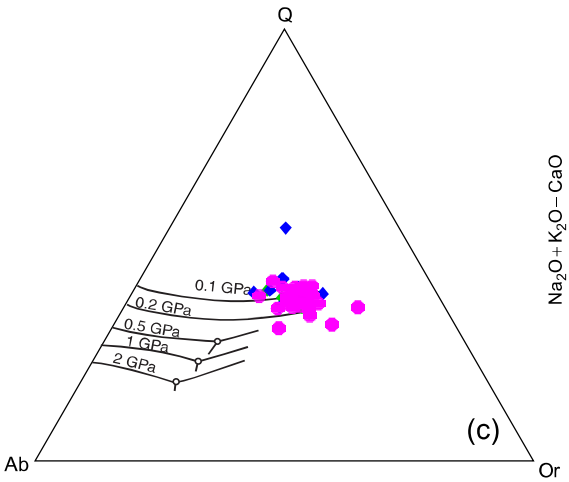

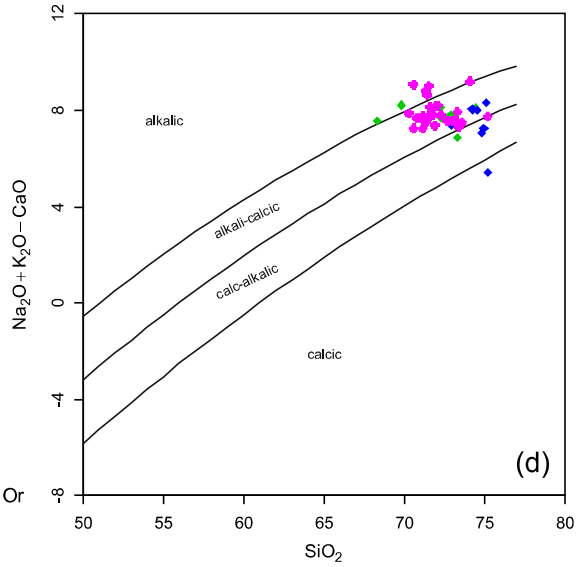

- Phyllite N
- Phyllite S
- Quartzphyllite N
- Quartzphyllite S
- Metatexite
- Type-1 diatexite
- Type-2 diatexite
- Granite

Fig.12

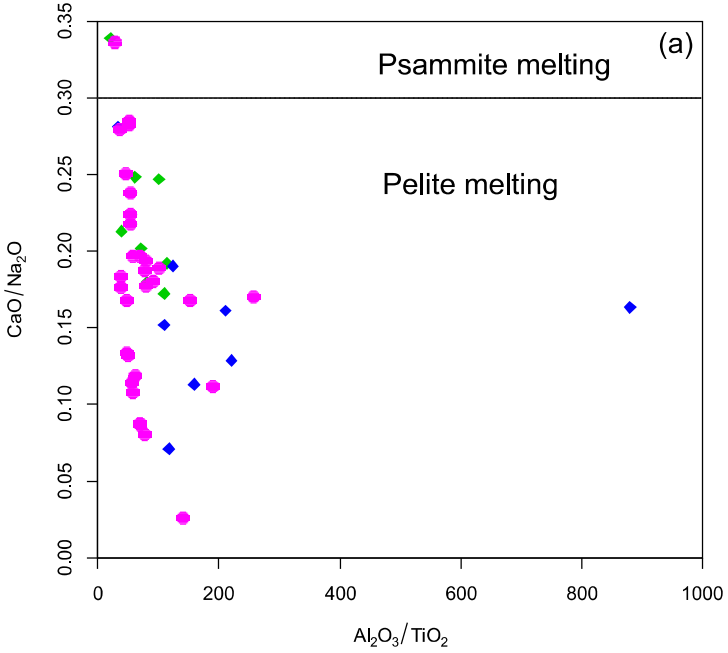
(a)
Psammite melting
Pelite melting
CaO/Na2O
Al2O3/TiO2
0.00
0.05
0.10
0.15
0.20
0.25
0.30
0.35
0
200
400
600
800
1000

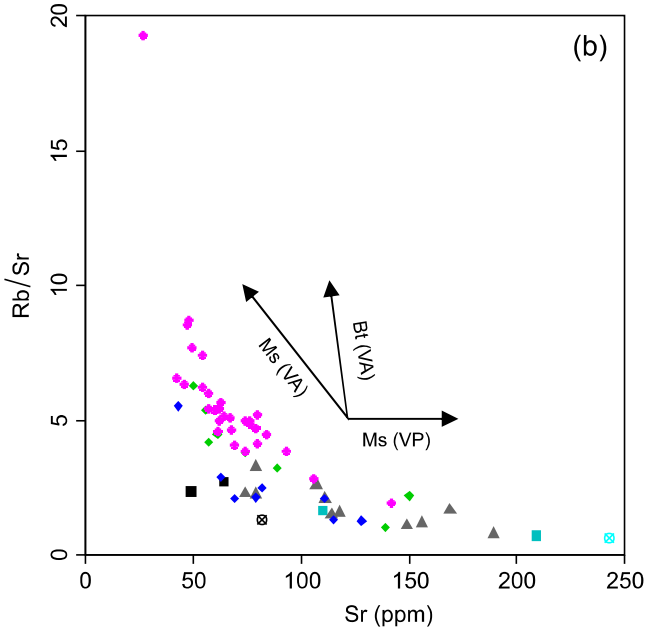
(b)
Rb/Sr
Sr (ppm)
Ms (VA)
Bt (VA)
Ms (VP)
0
5
10
15
20
0
50
100
150
200
250

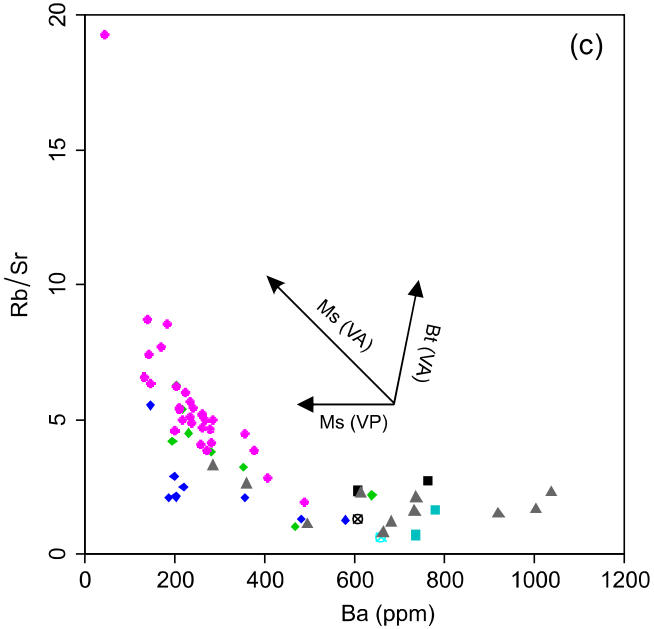
(c)
Rb/Sr
Ba (ppm)
Ms (VA)
Bt (VA)
Ms (VP)
0
5
10
15
20
0
200
400
600
800
1000
1200

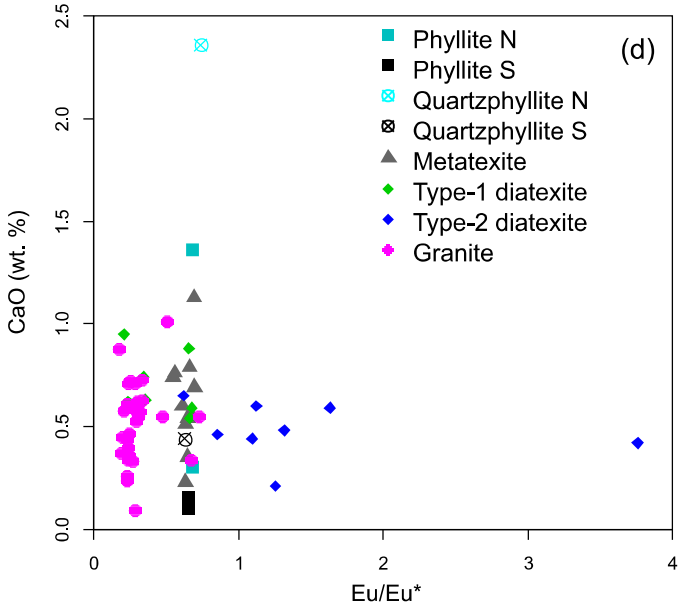
(d)
Phyllite N
Phyllite S
Quartzphyllite N
Quartzphyllite S
Metatexite
Type-1 diatexite
Type-2 diatexite
Granite
CaO (wt. %)
Eu/Eu*
0.0
0.5
1.0
1.5
2.0
2.5
0
1
2
3
4

Fig.13

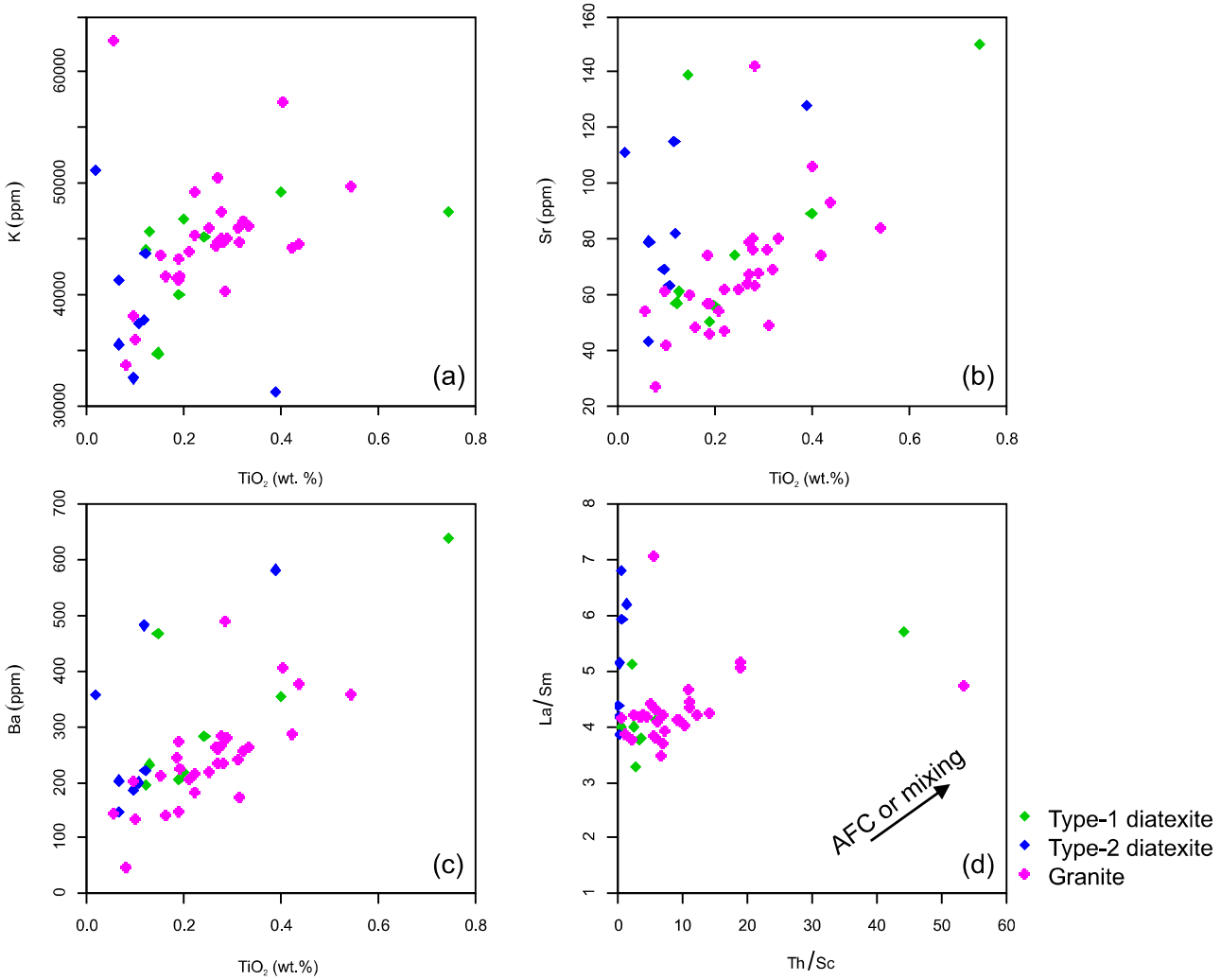
K (ppm)
30000
40000
50000
60000
0.0
0.2
0.4
0.6
0.8
TiO2 (wt. %)
(a)
Sr (ppm)
20
40
60
80
100
120
140
160
TiO2 (wt.%)
(b)
Ba (ppm)
0
100
200
300
400
500
600
700
TiO2 (wt.%)
(c)
La/Sm
1
2
3
4
5
6
7
8
0
10
20
30
40
50
60
Th/Sc
AFC or mixing
(d)
Type-1 diatexite
Type-2 diatexite
Granite

Fig.14

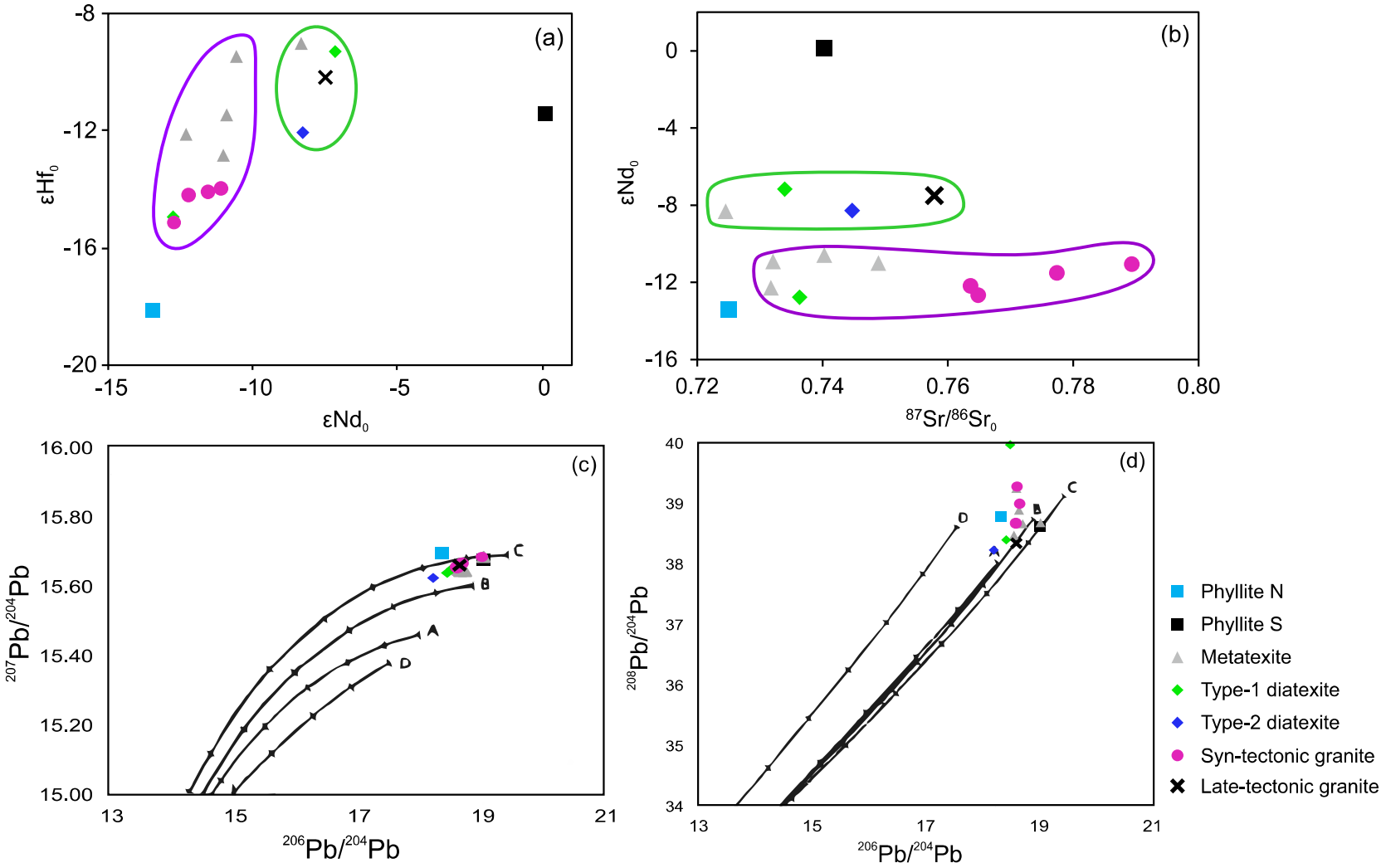
(a)
εHf0
εNd0
-8
-12
-16
-20
-15
-10
-5
0
(b)
εNd0
87Sr/86Sr0
0
-4
-8
-12
-16
0.72
0.74
0.76
0.78
0.80
(c)
207Pb/204Pb
206Pb/204Pb
16.00
15.80
15.60
15.40
15.20
15.00
13
15
17
19
21
A
B
C
D
(d)
208Pb/204Pb
206Pb/204Pb
40
39
38
37
36
35
34
13
15
17
19
21
A
B
C
D
Phyllite N
Phyllite S
Metatexite
Type-1 diatexite
Type-2 diatexite
Syn-tectonic granite
Late-tectonic granite

Fig.15

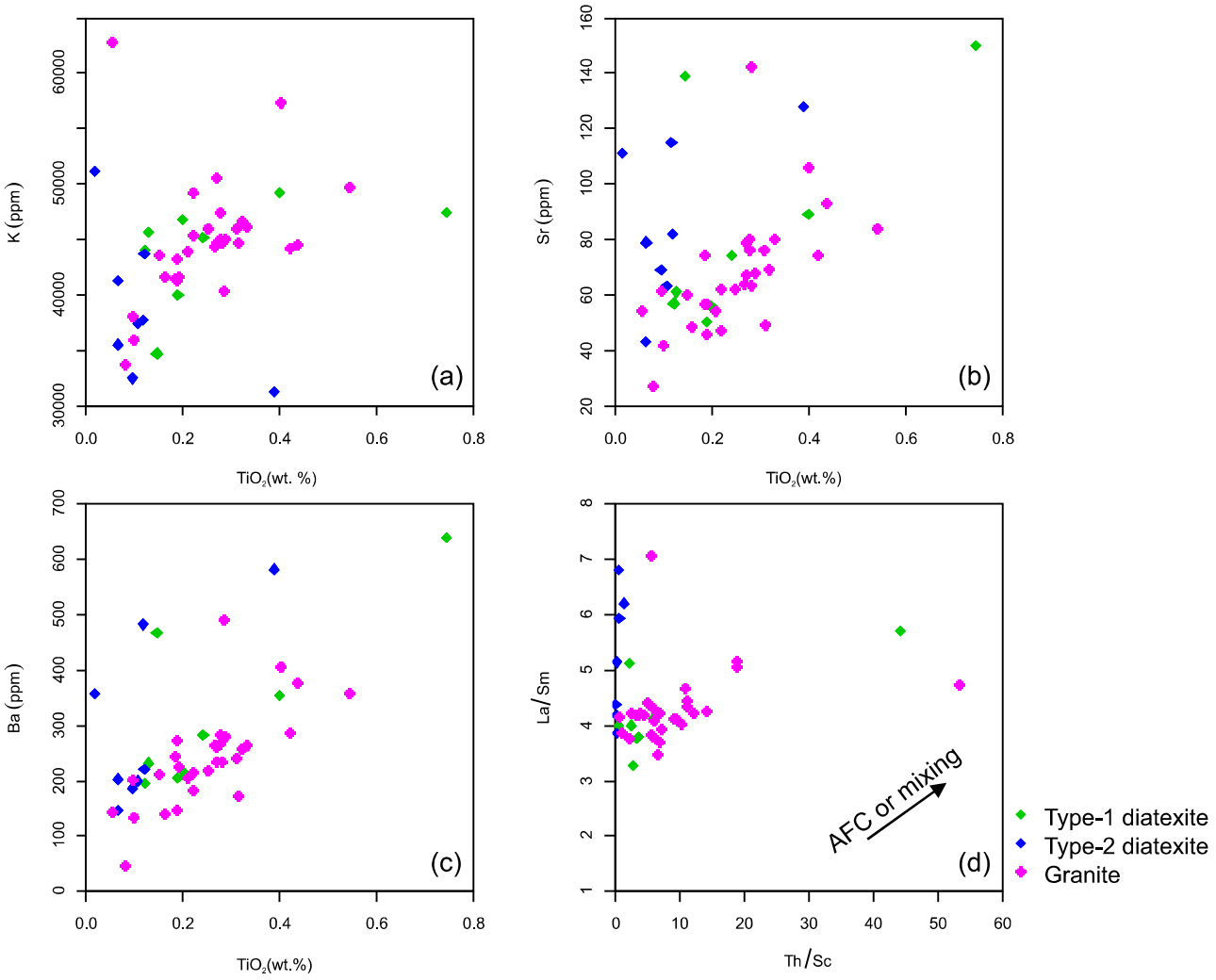
K (ppm)
30000
40000
50000
60000
0.0
0.2
0.4
0.6
0.8
TiO2(wt. %)
(a)
Sr (ppm)
20
40
60
80
100
120
140
160
TiO2(wt.%)
(b)
Ba (ppm)
0
100
200
300
400
500
600
700
TiO2(wt.%)
(c)
La/Sm
1
2
3
4
5
6
7
8
0
10
20
30
40
50
60
Th/Sc
AFC or mixing
(d)
Type-1 diatexite
Type-2 diatexite
Granite